Ulrich Radeschnig, BSc

Approaching Fundamental Resolution Limits during Focused Electron Beam Induced Gold Deposition on Bulk Substrates

MASTER'S THESIS

to achieve the university degree of

Diplom-Ingenieur

Master's degree programme: Technical Physics

submitted to

Graz University of Technology

Supervisor

Ass.Prof. Priv.-Doz. Dipl.-Ing. Dr. techn. Harald Plank

Institute of Electron Microscopy and Nanoanalysis

Graz, December 2017

Abstract

Focused electron beam induced deposition (**FEBID**) is a sophisticated additive, direct-write technology that enables the controlled fabrication of metallic structures with feature sizes in the sub-10 nm regime. This allows the realization of electromagnetic metamaterials (**MTM**), which can be used to manipulate spectral and spatial properties of electromagnetic fields forming the basis for plasmonic devices. Promising applications include near-field microscopy beyond the diffraction limit based on sub-wavelength field concentration, enhanced linear absorption, novel biochemical sensing, negative refraction and cloaking via a sub-unity refractive index, and tailored optoelectronic filtering. For visible and near-infrared wavelengths (**vis-NIR**), the lateral resolution of the metallic sub-structures typically needs to be on the scale of 10's of nanometers.

In this work, the manufacturability of such nanostructures via FEBID for optical MTM is studied in detail, using arrays of bi-ring structures that for the intended design parameters should exhibit multiple resonances in the vis-NIR range. As the precise fabrication is not only important but decisive, effective patterning schemes and scan strategies were elaborated to approach FEBIDs fundamental resolution capabilities. The main fabrication obstacle was primarily based on the successive depletion of adsorbed precursor molecules during material deposition, which adversely affected the required preciseness and led to deviating and inhomogeneously distributed geometries. However, even with this persistent limitation, plasmonic MTM could be successfully fabricated.

To compensate the scarcity of precursor molecules, further emphasis was put on the extraction of parameter-morphology relationships by using a different feature design. In more detail, distinct electron beam movement settings such as the pulse duration or patterning cycles sequences were systematically studied for two different precursor materials (Me_2-Au(acac) and $MeCpPt^{IV}Me_3$). By that, it was possible to separate material dependent effects from fundamental processes, which revealed a still improper working regime. To compensate the latter, an electron beam idle time was introduced, which strongly increased the precursor molecule coverage. This successfully shifted the FEBID working regime from being molecule transport limited into reaction rate limited conditions, which finally procured the development of fully homogeneously distributed structures. In numbers, the final structures revealed full width half maximum values of less than 13 nm at heights of 8 nm, which had set a benchmark in this specific research area.

Kurzfassung

Die Materialabscheidung durch fokussierte Elektronenstrahlen (Focused Electron Beam Induced Deposition, **FEBID**) ist eine hochentwickelte, additive Direkt-Schreibtechnologie, welche eine kontrollierte Herstellung von metallischen Strukturen im Sub-10-nm-Bereich ermöglicht. Damit lassen sich elektromagnetische Metamaterialien (**MTM**) realisieren, welche für die Manipulation von spektralen und räumlichen Eigenschaften verwendet werden können und damit die Basis plasmonischer Bauelemente darstellen. Vielversprechende Anwendungen umfassen die Nahfeldmikroskopie jenseits der Beugungsgrenze über Subwellenlängen-Felddichten, verbesserte lineare Absorptionen, neuartige biochemische Sensoren, negative Brechung und Verhüllung über subunitäre Brechungsindizes sowie maßgeschneiderte opto-elektronische Filter. Für sichtbare und nahinfrarote Wellenlängen (**vis-NIR**) muss die laterale Auflösung der metallischen Substrukturen typischerweise im unteren zweistelligen Nanometerbereich liegen.

In dieser Arbeit wird die FEBID-Tauglichkeit hinsichtlich der Fabrikation derartiger MTM-Nanostrukturen untersucht, wobei Gold Bi-Ring Arrays als Testgeometrie verwendet wurden, welche mehrere Resonanzen im vis-NIR-Bereich aufweisen sollten. Da eine präzise Fertigung nicht nur wichtig, sondern entscheidend ist, wurden effektive Strukturierungsschemata und Scanstrategien entwickelt, um das fundamentale Auflösungslimit der FEBID voll auszuschöpfen. Das zentrale Hindernis bei der Herstellung war vor allem durch den sukzessiven Abbau von adsorbierten Ausgangsmolekülen während der Materialabscheidung gegeben, das die geforderte Genauigkeit erheblich beeinträchtigte und damit zu abweichenden und inhomogen verteilten Geometrien führte. Allerdings konnten plasmonische MTM selbst mit dieser persistenten Einschränkung erfolgreich hergestellt werden.

Um die lokal abfallende Dichte der Ausgangsmoleküle zu kompensieren, wurde der inhaltliche Fokus auf die Parameter-Morphologie-Abhängigkeit gelegt, wofür ein geändertes, idealisiertes Strukturdesign verwendet wurde. Dazu wurden für zwei unterschiedliche Vorläufermaterialien (Me_2-Au(acac) und $MeCpPt^{IV}Me_3$) jeweils verschiedene Einstellungen zur Elektronenstrahlbewegung, wie z.B. die Pulsdauer oder die Abfolge der Strukturierungszyklen, systematisch untersucht. Dadurch war es möglich, materialabhängige Effekte von fundamentalen Prozessen zu trennen, wobei sich ein noch immer unzulängliches Arbeitsregime offenbarte. Um diesen Umstand zu kompensieren, wurde eine Elektronenstrahl-Leerlaufzeit eingeführt, was den Bedeckungsgrad der Ausgangsmoleküle stark erhöhte. Dies führte zu einer erfolgreichen Verschiebung des FEBID-Arbeitsregimes von molekül- hin zu elektronenlimitierten Bedingungen, welches die Fabrikation von homogen verteilten Strukturen ermöglichte. Derartig hergestellte Strukturen zeigten Halbwertsbreiten von weniger als 13 nm bei Höhen von 8 nm, welche in diesem Forschungsgebiet den gegenwärtigen Benchmark darstellen.

Acknowledgements

I would like to thank all persons that contributed to this thesis by supporting me during my work.

Initially, a special thank goes to Ao.Prof. DI Dr. Ferdinand Hofer, head of our institute, for providing the opportunity to write this thesis.

My greatest gratitude goes to my supervisor Ass.Prof. Harald Plank for inspiring me. His ability to constantly excite his students, his talent to simplify complex tasks and to handle knotty situations are remarkable.

I want to express further thanks to my working group colleagues at the FELMI-ZFE, particularly to DI Robert Winker for the instruction on handling the technical equipment and DI Jürgen Sattelkow for the support on the bi-ring fabrication.

At last, I want to express my deepest recognition to my family for invariably backing me and the things I do - and to my parents, for the incessant and unconditional love they provide.

Table of Contents

List of Abbreviations

AFM	…	*atomic force microscope*	LLE	…	*low-loss electrons*
BSE	…	*back scattered electrons*	MTL	…	*molecule transport limited*
DBM	…	*dual beam microscope*	MTM	…	*metamaterials*
DE	…	*diffusion-enhanced regime*	vis-NIR	…	*visible and near-infrared*
DEA	…	*dissociative electron attachment*	PLR	…	*pressure limiting aperture*
DI	…	*dissociation ionization*	PoP	…	*point pitch*
DT	…	*dwell time*	PSD	…	*positioning sensing detector*
EDX	…	*energy dispersive x-ray spectroscopy*	RRL	…	*reaction rate limited*
ELR	…	*electron limited regime*	RT	…	*refresh time*
ESEM	…	*environmental scanning electron microscope*	SE	…	*secondary electrons*
ETD	…	*Everhardt Thornley detector*	SEM	…	*scanning electron microscopy*
FEBID	…	*focused electron beam induced deposition*	S-TET	…	*specific total exposure time*
FIB	…	*focused ion beam*	TEM	…	*transmission electron microscopy*
FIBID	…	*focused ion beam induced deposition*	TET	…	*total exposure time*
FWHM	…	*full width at half maximum*	TLD	…	*through the lens detector*
GIS	…	*gas injection system*	TRT	…	*total refresh time*
IL	…	*interlacing*	UHR	…	*ultra-high resolution*
ITO	…	*indium tin oxide*	VdW	…	*Van der Waals*

1 Introduction

There is a practical limit for transistors and devices resting upon electron transport to work viable for frequencies higher than 300 GHz[1], wherefore directly manipulating spatial and spectral properties of electromagnetic fields for frequencies such as of visible and near-infrared wavelengths (**vis-NIR**) is by these means not viable. However, structures able to collectively generate charge carrier waves enable a conversion of vis-NIR frequencies from subwavelength volumes into free space and vice versa (i.e. plasmonic antennas)[2], and thereby give further access to optoelectronics[3] such as optical negative-index metamaterials[4], light emitters, energy harvesting, and photonic chips[5]. These plasmonic electromagnetic metamaterials (**MTM**) typically require specially designed geometries and dimensions of down to several nanometers, whose realization is hardly feasible.

Compared to the conventional method of electron beam lithography, the application of direct-writing via focused electron beam induced deposition (**FEBID**) offers certain distinct advantages, i.e. the ability to fabricate complex geometries and true 3D architectures in the two-digit nanometer scale for modification of existing devices or combination of different metals. The use of 3D structures not only allows more freedom to tailor electromagnetic MTM properties (e.g. via the effective inductance / capacitance) but also to potentially customize specific receptors (e.g. chemical and biological species). This thesis will focus on the evaluation of potential performances of specific designed MTM, compounded by a 12 × 12 array of Au bi-ring structures with inner and outer diameters of 65 nm and 175 nm, respectively, and a base line widths of 25 nm at heights > 10 nm. For the intended frequency range (vis-NIR), Au is (beside Ag and their alloys) the best material for plasmonic applications[6].

In 2016, Ulrich Haselmann, a former master student in the work group around Prof. Plank at the Institute of Electron Microscopy (Technical University in Graz), already had proven the feasibility of fabricating solitary bi-rings[7] with these dimensions via FEBID by using Me_2-Au(acac) as precursor material. The individual bi-rings fulfilled the required conditions to be potentially applicable as MTM. The development was nontrivial, as FEBID actually has its drawback in the structure matrix impurity, revealing carbon contaminations of up to 90 at.%[8], which basically thwarts the usage as plasmonic device since the high carbon content does not appropriately allow plasma waves propagation. To settle this disadvantage, in 2014, Geier et al., who also had been a former master student in the work group around Prof. Plank, successfully had developed a subsequent purification method by using an electron beam assisted approach within an H_2O atmosphere[9]. Despite the purification process rendered pure metallic structures, the method was explicitly applied on materials that were fabricated using the $MeCpPt^{IV}Me_3$ (platinum) precursor, and the effect on as-deposited Au structures had not been studied. Furthermore, the purification is accompanied by a strong volume loss (due to carbon extraction), causing the structures to lose roughly two thirds of their height. This in turn forces the as-deposited structure do be designed nearly three times higher than the intended MTM dimension. However, both the purification of the Au structures and the height loss after the purification process could be managed by Haselmann et al.

This work proceeds the idea of creating MTMs by addressing on the fabrication of an array consisting of 144 (12 × 12) Au bi-rings, which together should exhibit measurable resonances for frequencies in the vis-NIR range. For this purpose, several parameter optimizations will be done and the fundamental resolution limit of FEBID will be approached by applying Au and Pt based precursor types.

2 Instrumentation

2.1 Dual Beam Microscope

2.1.1 Components

A dual beam microscope (**DBM**) is a microscope system for 3D characterization, sample preparation and nano-prototyping that unifies a scanning electron microscope (**SEM**) and a focused ion beam (**FIB**) microscope within one divice[10]. This combination allows imaging (SEM) and material sputtering (FIB) simultaneously, which is highly practical for many specialized applications.

The DBM is mainly used for preparing specimen lamellas for transmission electron microscope (**TEM**) analyses. To enable TEM investigations, these specimens require to exhibit extremely low thicknesses, which is sufficiently provided via FIB cutting. After carving, a lamella is subsequently mounted onto a TEM grid. For the processing of lifting and sticking a sample onto a TEM grid, a micromanipulator and several gas injection systems (**GIS**) are installed within the DBM. The GIS delivers specialized precursor gas into the vacuum chamber, which is principally used for fusing the sample onto the grid. Other applications involve device modification, circuit editing[11], failure analysis, energy dispersive x-ray spectroscopy (**EDX**) and electrical measurements. The availability of GIS and SEM / FIB enables specialized surface structuralizing by material deposition (additive) or material etching (subtractive), depending on the applied precursor type.

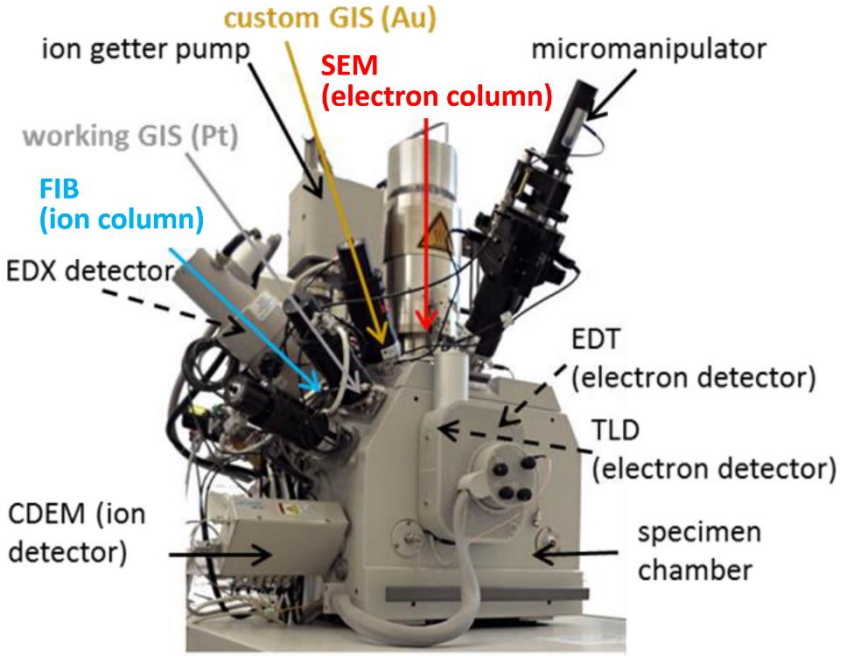

Figure 1: DBM (FEI NOVA 200) with several components. FIB (blue arrow) and SEM (red arrow) columns are tilted by 52° to each other. The specimen chamber requires high vacuum provided by roughing pumps, a turbo-molecular pump and, within the columns, ion getter pumps. The experiments in this thesis required the SEM, the Au custom GIS (golden arrow) and the Pt working GIS (gray arrow). For imaging, ETD and TLD were used.[12]

An overview of the main components of the DBM utilized at this institute is depicted in Figure 1. The DMB type used is a *NOVA 200* from *FEI*, in which the SEM and FIB columns are tilted by 52° to each other. For operating, the sample surface (being mounted on a stage) has to be adjusted on the intersection point of electron and ion beam. This setting is indicated as "eucentric height", which is located roughly 5 mm beneath the bottom end of the SEM column (i.e. the pole piece of the last lens)[13]. The experiments in thesis did not require the usage of the FIB column, wherefore an adjustment in the eucentric height was not mandatory and the sample-to-column distance principally could be decreased, which would raise the resolution performance, but the presence and position of GIS and micromanipulator is a technical restriction that allows merely little change.[14] This thesis is based on the capability of material deposition via SEM with the GIS systems (more details found in chapter 2.2).

2.1.2 Vacuum System

For proper operation, the DBM chamber requires high vacuum conditions for preventing the electrons to scatter at gas atoms. This is resized by a multistage pump system.[13] Roughing pumps evacuate the vacuum chamber in a first stage (low vacuum) before a turbo-molecular subsequently kicks in to attain a high vacuum level. As both SEM and FIB sources require ultra-high vacuum, their columns have additional ion getter pumps integrated (see Figure 1). While typically operating in the upper 10^{-6} mbar range, the prevailing operating pressure when having the GIS valves open is in the 10^{-5} mbar range.

2.1.3 SEM - Electron Column

The electrons in this DBM type are generated by a Schottky emitter, which principally is a combination of the concepts of thermic emitter and field emission gun. The wolfram tip (typically for field emission guns) of the emitter is coated with ZrO, which reduces the work function to 2.7 eV[15]. The generated electrons then pass through a lens and aperture system towards the sample, as visible in Figure 2. Condenser lenses (C1 and C2) demagnetize the beam and aligns it being parallel with respect to the optical axis (in the red area in Figure 2). The electrons then get deaccelerated to the appointed voltage (for the *NOVA 200*: 1 - 30 keV). One of several permutable apertures (with different diameters) is subsequently implemented to vary the beam current. Electron steering and the corrections of lens aberrations (i.e. chromatic and spherical aberrations, axial astigmatism and diffraction error) is performed via duplex (objective) lenses (in the blue area in Figure 2). Before the beam impinges on the sample, it passes through the final objective lens, and additionally, if imaging in the ultra-high resolution (**UHR**) mode, an UHR lens.[13]

The reason for using multiple condenser lenses is that the theoretical resolution limit, given by the Rayleigh criterion, is mainly depending on the opening angle of the electron beam, which basically increases with the number of beam crossovers (lenses). The Rayleigh criterion is described by equation 1. The smallest distance δ of two separate points to get individually resolved is depending on the De Broglie wavelength λ (i.e. 0.07 Å for electrons with 30 keV), the index of refraction η (i.e. zero for vacuum) and the semi divergence angle β of the impinging beam (i.e. 2 - 5 mrad).

$$\delta = \frac{0.61\,\lambda}{\eta \sin(\beta)} \tag{1}$$

However, the actual resolution limit is not determined by the Rayleigh criterion but rather by the lens aberrations and the volume of electrons and sample interaction. If the SEM column in the *NOVA 200* is well adjusted, the laterally Gaussian distributed electron beam impinges with a spot size of approximately 1 nm.

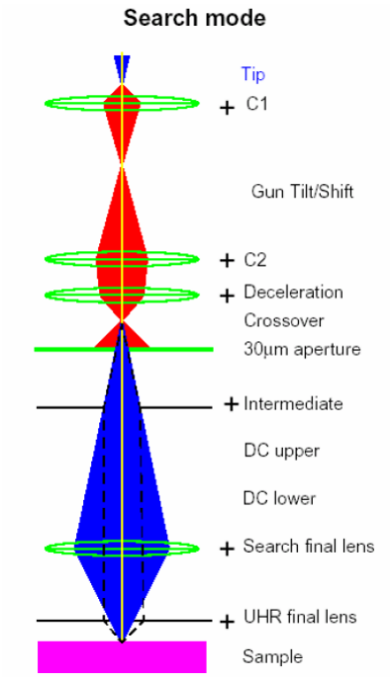

Figure 2: Scheme of a SEM column. The electron beam passes several condenser lenses (green ellipses in the red area) and objective lenses (green ellipses in the blue area) before impinging on the sample. The aperture is situated between those lenses types (green line) and defines the beam current.[16]

2.1.4 Interaction of Electrons with Matter

Electrons that impinge on a (solid) sample interacts with its atoms elastically and inelastically. Due to the energy / velocity of the electrons, they penetrate into the bulk material and spread laterally as a result of multiple scattering processes. The increasing interaction volume spreads the information area which leads to a decline in imaging accuracy. Even though the interaction process is a statistical process that makes the depth of penetration not sharply restricted, it is still possible to closely estimate the penetration depth *R*

$$R \propto \frac{E^{5/3}\,A}{Z^{0.89}\,\rho} \tag{2}$$

with the atomic weight *A*, the electron energy *E*, the atomic number *Z* and the bulk material density ρ. As apparent from formula (2), the penetration depth is strongly determined by the acceleration voltage. Figure 3 shows a Monte Carlo simulation of the trajectories of electrons penetrating a silicon (Si) substrate with 5 keV (a) and 30 keV (b).

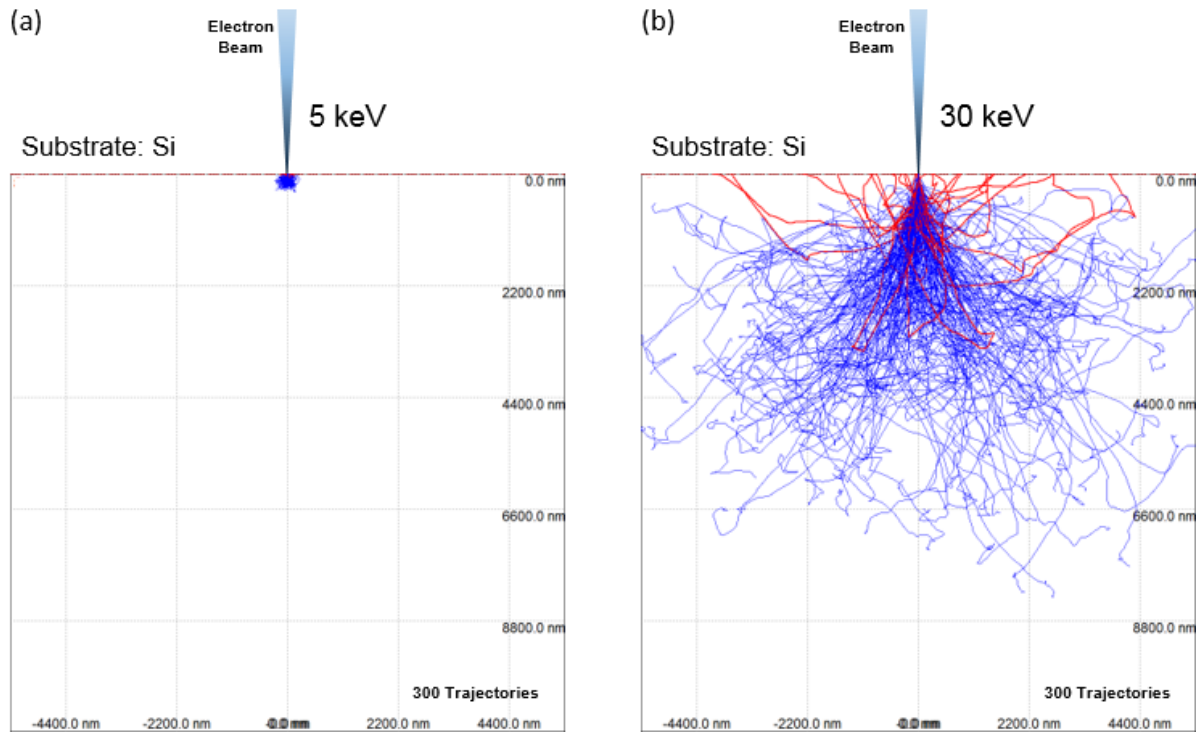

Figure 3: Monte Carlo simulation[17,18] of electrons penetrating a bulk sample (Si) with 5 keV (a) and 30 keV (b). The interacting volume strongly increases with higher energies. The blue trajectories represent electrons that grind to a halt within the substrate, the red trajectories those able to leave the substrate (BSE, see text).

The penetration depth of the 30 keV electrons vastly surpasses that of the 5 keV electrons. The choice of electron energy typically depends on the area of interest: If the emphasis is on the investigation of bulk material, the electrons are required to have high energies (30 keV). Precise surface inspections (imaging) on the other hand demand lower electron energies (1 - 5 keV).

There are several possible ways an impinging primary electron (**PE**) can interact with material and generate derivative particles and electromagnetic signals (see Figure 4(a)). The fraction of electrons that maintain enough energy to leave the material are referred to as backscattered electrons (**BSE**), which are identifiable as red trajectories in Figure 3(b). BSE have energies that range between 50 eV (per definition) and the initial energy of the PE (see Figure 4(b)).[13,19] BSE that nearly remain all of their initial energy are referred to as low-loss electrons (**LLE**). Inelastic scattering is primarily caused by electrons that interact with the atomic shells of the sample atoms. The electrons are hereby slowed down by multiple small angles scattering interactions. By hitting an upper shell, they may instigate the ejection of secondary electrons (**SE**) which are defined to have energies below 50 eV but have a significant yield as seen in the re-emission diagram in Figure 4(b). Due to their low energy the SE do have a travelling range of only a few nm within the substrate and subsequently can exit the sample merely near the surface (< 5 nm)[13,19]. SE in a sample are either generated by PE (referred to as $\mathbf{SE_1}$) or by BSE (referred to as $\mathbf{SE_2}$). A propagating high energy electron can also cause an inner shell electron to be ejected from an atom. The inner shell vacancy is then replaced by an outer electron from a higher orbital, which in turn results in the emission of either an auger electron (**AE**) (mainly appearing for

elements with low mass numbers) or characteristic X-ray radiation (mainly appearing for elements with high mass numbers). The interaction with the screened Coulomb field of the nuclei consecutively decelerates propagating electrons which constantly generates continuous bremsstrahlung. Additionally, electrons are able to engender quasiparticles such as plasmons, electron-hole pairs and phonons within the substrate. The electron-hole pairs occurring in semiconductors create electric current (induced current) or, if recombined, photons in the infrared, visible or ultraviolet wavelength range (cathodoluminescence). The frequency of occurrence and energy distribution of the electron types generated by the electron beam are depicted in Figure 4(b).

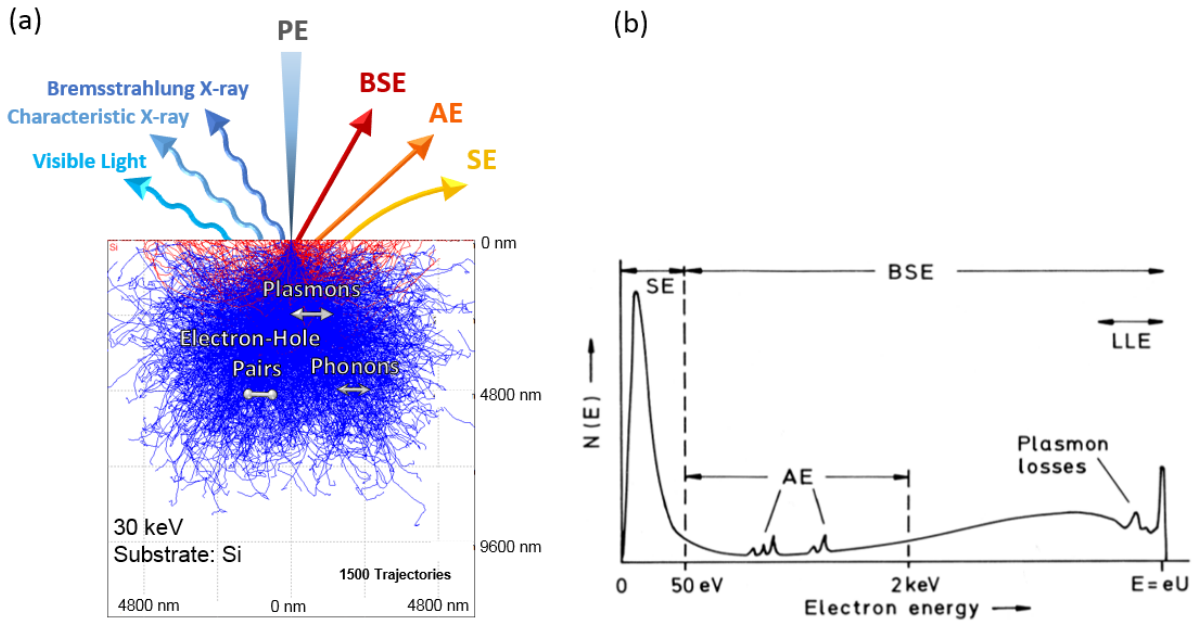

Figure 4: The impinging primary electrons (PE) create derivative electrons of varying energies, electromagnetic waves and quasiparticles within a solid. Electrons that reenter the vacuum (red trajectories) are referred to as backscattered electrons (BSE). PE and BSE both may generate secondary electrons (SE), which are able to exit the substrate for depths of merely a few nm due to their low energy of less than 50 eV. (b)[19] Frequency of occurrence and energy of varying electron types. BSE do have energies higher than 50 eV, wherefore they are able to leave the substrate from depths up to several µm.

2.1.5 Electron Detectors

There are two separately working types of electron detectors integrated in the used DBM system, which is the Everhart-Thornley detector (**ETD**) and the through-the-lens detector (**TLD**). The setup of the ETD is sketched in Figure 5. To distinguish between the SE and BSE, the ETD implies a collector that could be biased positively or negatively, depending on whether BSE or SE are targeted for detection. After leaving the substrate and reentering the vacuum, the trajectories of the low energy electrons (SE) are strongly influenced by electromagnetic fields, whereas the high energy electrons (BSE) barely change their trajectories. If the collector is biased positively, the SE are attracted by the electric field and bundled onto the scintillator, which subsequently reemits light signals. This signal is transferred by a light pipe into a photomultiplier, where it gets amplified for further processing. In turn, a positively

biased collector repels the SE from the detector, meaning that only the BSE are able to approach it. As the scintillator works for both electron types, the information from BSE gets proceeded similarly. The ETD is installed in a tilted angle relative to the beam axis, giving the resulting image a 3D character. This is explained by the changing obstacle for electrons to approach the ETD depending on whether they reenter the vacuum on a sample area that is faced towards or faced away from the detector. Therefore, the signal yield increases for surface areas that are faced towards the detector (brighter areas in the final image), and decreases for surface areas that are faced away (darker areas in the final image).[13]

The TDL is located rotationally symmetrically around the electron beam axis inside the electron column. This implies that the electrons from the sample have to move back towards the objective lens. To enable the electron motion to the scintillator, the detector has to have a high and positive bias (+10 kV[13]) applied. SE (SE_1 or SE_2) are capable to reach the detector, BSE on the other hand cannot, as their trajectories remain uninfluenced.[13] The TDL detector is used for imaging in the UHR mode.

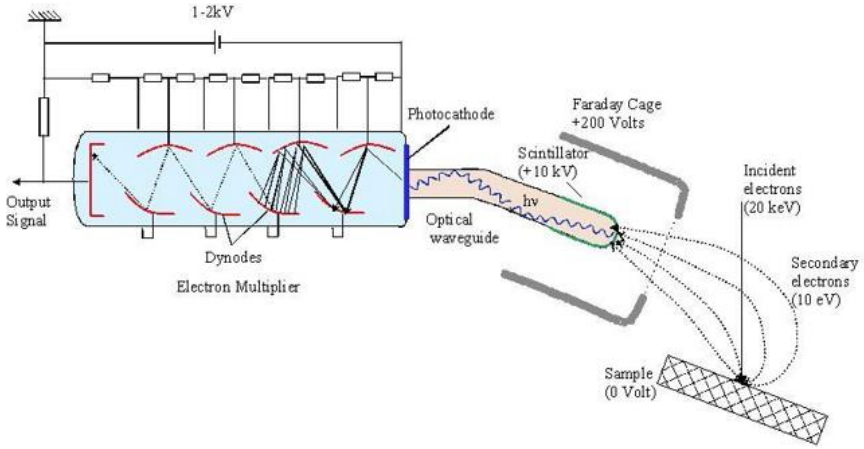

Figure 5: Schematic diagram of an Everhart-Thornley detector (ETD). The SE from the sample get bundled by a positively biased collector onto a scintillator, which then generates light signals. The signal is amplified in an electron multiplier for further processing (output signal). BSE are detected only if their trajectories point directly onto the scintillator.[20]

2.2 Focused Electron Beam Induced Deposition

2.2.1 Basic Concept

Focused electron beam induced deposition (FEBID) is an additive, direct-write fabrication technique that allows additive 3D nano-manufactoring[21–23], typically realized within a SEM or FIB. The vacuum chamber thereby is equipped with a gas injection system (**GIS**), which provides a specific precursor gas that gets injected onto a surface on which it adsorbs. The electron beam dissociates the precursor molecules when impinging on the substrate surface. The molecules separate into a volatile part that gets pumped out of the system and a non-volatile part that remains on the surface forming a deposit.

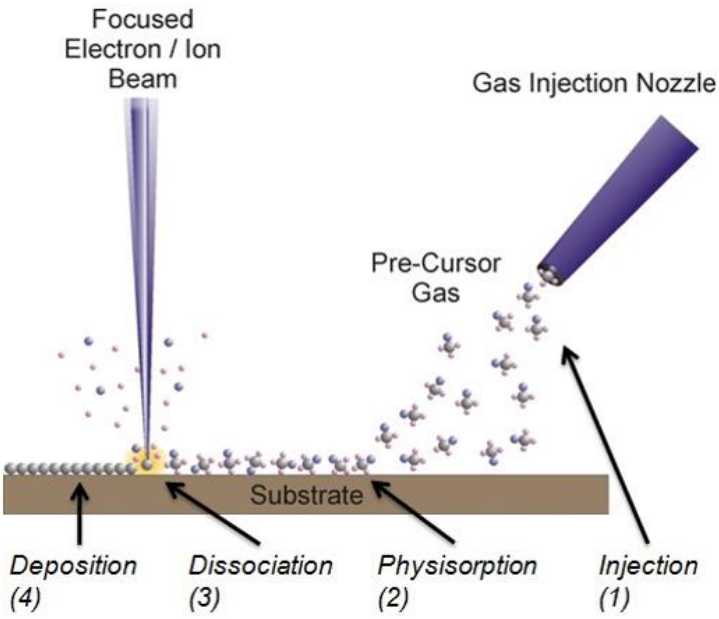

Figure 6: Scheme of the working principle of FEBID / FIBID. Precursor molecules adsorb onto a substrate and gets dissociated by an electron / ion beam. The molecule separate into a volatile and a non-volatile part, whereas the non-volatile part forms the deposit.[24]

Figure 6 visualizes a simplified scheme of the FEBID working principle. The GIS nozzle is positioned close to the surface to ensure a high precursor density in the intended deposition area. Molecules physiosorb onto the substrate, randomly diffuse and subsequently desorb after a certain residence time[25]. If the technique is used in combination with a focused ion beam, it is termed focused ion beam induced deposition (**FIBID**) which has, despite similar fundamental processes, different depositing characteristics regarding deposit growth rate and others properties.[21] However, FIBID has the massive drawbacks of unwanted material implantation (mostly Ga), partly significant temperature rises with less resolution due to the different deposition channels. This is the main reason why ultra-high-resolution fabrication is mostly done via electrons. FEBID deposits reveal a wide range of functionalities depending of the used precursor type, ranging from being magnetic, insulating or (semi-) conductive[23,26,27]. Established application fields include lithography-mask repair[28,29], probes for nano-optics[30,31] or strain sensors[32,27], or specifically tuned magnetic devices[33–36]. In recent years, the work group around Prof. Plank increasingly focuses on the FEBID based modification of scanning probe microscopy tips to enable new measurements modes, which exploit their full potential together with FEBIDs true 3D nano-printing capabilities.

2.2.2 Dissociation Mechanism

The probability that impinging electrons dissociate adsorbed precursor molecules depends heavily on the dissociation cross section, which primarily correlates with the electron energy. The dissociation cross section has its highest level for energies of a few eV[37], which falls into the range of SE. There are two relevant dissociation processes to be mentioned, which is the dissociative electron attachment

(**DEA**) and the dissociation ionization (**DI**). The DEA appears in the low electron energy range (1 - 5 eV) and therefore dominates the mechanism of molecule splitting. The DI requires energies higher than 10 eV and has a minor part in the deposition dynamics due to the small amount of high energy electrons[37] (see energy distribution in Figure 4(b)). The effect of the PE to the dissociation process is miniscule[21,23,37]. As SE do have a small range of propagation (few nm), the logical conclusion would be that the deposition accuracy is similar to the electron beam diameter. In fact, as SE are not solely generated by PE (SE_1) but also by BSE (SE_2) the lateral spread of SE is significantly higher (c.f. red trajectories in Figure 3(b)), which subsequently worsens the depositing accuracy.

2.2.3 Precursor and Gas Injection System

There is a range of precursor types with different characteristics available[26], making several applications for varying purposes attainable. They are typically metal-organic molecules compounded by hydrocarbons or other volatile units (ligands) surrounding a representative center atom. Examples of center atoms are Si, Fe, W, Pt, or Au[26]. Impurities are caused if the separation of the center atom from the ligands is not completely fulfilled (see Figure 8).

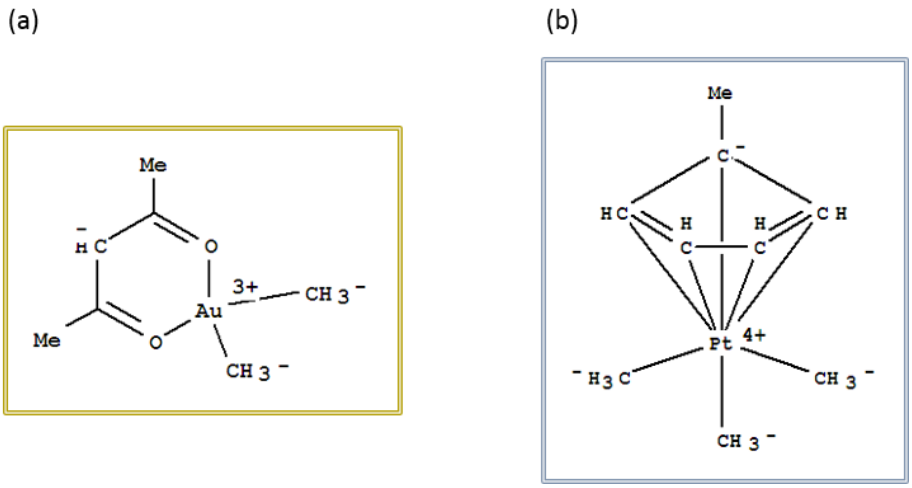

Figure 7: The precursor types used during this work: (a) Me_2-Au(acac) is deployed for the deposition of Au.[38] (b) MeCpPt^{IV}Me$_3$ is deployed for the deposition of Pt.[38] Both molecule types are compounded by hydrocarbons that surround the representative center atom.

To be applicable the precursor has to fulfill a variety of requirements, which include the ability for physisorption and the capability for decomposing when impinged by electrons, as well as other nontechnical properties such as economical and toxicological legitimacies[21]. In this work the precursor types Me_2-Au(acac) (full denotation: dimethylgold^{III} acetylacetonate) and MeCpPt^{IV}Me$_3$ (full denotation: trimethyl(methylcyclopentadienyl)-platinum(IV)) were used (see Figure 7), which are frequently just termed “Au precursor” and “Pt precursor”, respectively. The purity of the deposition is rather meagre with being approximately 8 at.% for Au and 15 at.% for Pt.[8] The majority of bulk material is carbon (see Figure 9).

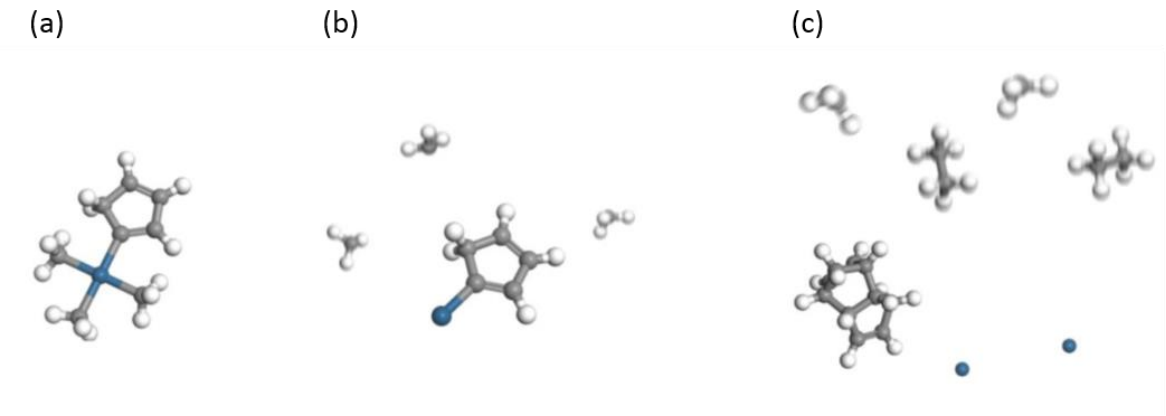

Figure 8: A precursor molecule ($MeCpPt^{IV}Me_3$)) before (a) and after dissociation ((b) and (c)). The blue atoms represent the intended atom (Pt) to adhere on the substrate after molecule cracking, the gray and white atoms represent the carbon and hydrogen atoms, respectively. The dissociation by the electron beam does not automatically mean the precursor molecule is cracked the anticipated way (c) in which the Pt atoms (blue) are completely separated from the polymerized organic compounds (gray and white). In most cases the detachment is partial incomplete (b), which raises carbon impurities within the deposit.[24]

The Au and Pt precursors were injected by two GIS separately. The system providing Au was referred to as custom GIS and the other one providing Pt was referred to as working GIS. Both precursor types required an accurately set temperature for working reliably. For this reason, the working GIS was heated to 45 °C and the custom GIS to 30 °C, both for at least 30 minutes before and during deposition. For details on the GIS alignment see chapter 4.1.1 and chapter 4.2.2.

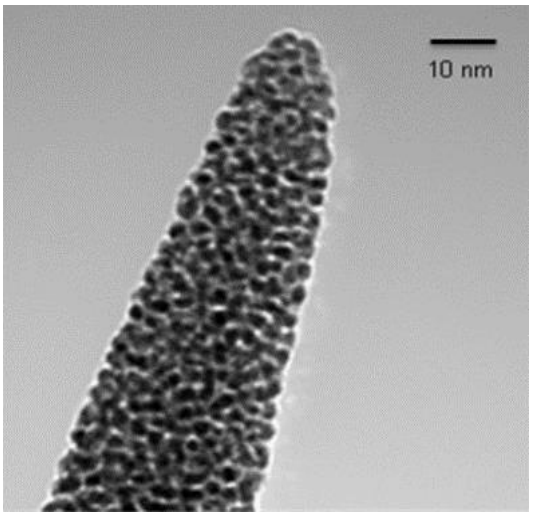

Figure 9: TEM image of a structure fabricated via FEBID by applying the Pt precursor. Visible are the metallic nanoclusters (dark areas) within a carbon matrix (bright area). The granular morphology has a Pt fraction of merely 15 at.%.[39]

2.2.4 Working Regime

The dissociation process and deposition behavior heavily depend on the ratio of available precursor molecules to impinging electrons, affecting growth rates[40], functionality[41] and chemical composition[21,40]. There are two main regimes and one intermediate regime to classify the ratio during deposition[21,42–44]:

1. The reaction rate limited regime (**RRL**) also called electron limited regime (**ELR**): This working regime is prevailing if the amount of adsorbed precursors on the surface is surpassing the amount of electrons for potential dissociation. In this case the quantity of electrons is limiting the growth rate. As most of the electrons are absorbed in large portions by the molecules before entering the substrate, the deposits emerge relatively small in their lateral expansion (thin deposits). The laterally Gaussian distributed electron density leads to deposits that are rendered laterally Gaussian distributed likewise. The RRL working regime provides the best depositing resolution with the most accurate tunability.
2. The mass transport limited regime (**MTL**) also called molecule limited regime (**MLR**): This working regime is characterized by a superior number of impinging electrons compared to adsorbed precursor molecules. The growth rate is limited by the amount of available precursor molecules and is thereby smaller than in the RRL working regime. The cross-section profile of single points / lines reveal a flat-top shape (see right-hand side in Figure 10), as the central area is constantly limited by direct molecule replenishment from the gas phase, while the outer areas are replenished by surface diffusion from surrounding areas (explaining the non-vertical side slopes).
3. The diffusion enhanced regime (**DER**): These conditions emerge in the transition from pure RRL towards MTL. Effectively, the morphology is determined by surface diffusion from surrounding areas and varies from broader Gaussian profiles towards non-Gaussian, flat top shapes (see morphologies in the white regions of Figure 10). Most FEBID processes work in these regime conditions,[21] which also explain the many different reported shapes and achievable line widths.

In essence, the working regime is the most central element in FEBID, and almost any drawback can be traced back to the local electron - molecule ratio. It not only decides about shapes and lateral dimensions but also has strong implications on the chemistry and thus on the functionality[26,40,45]. By that, attention has to be paid on the estimation of the working regime before any geometry with a given functionality can be aimed. This is in particular the focus of this thesis, as it will be shown in detail how the working regime can influence the final outcome.

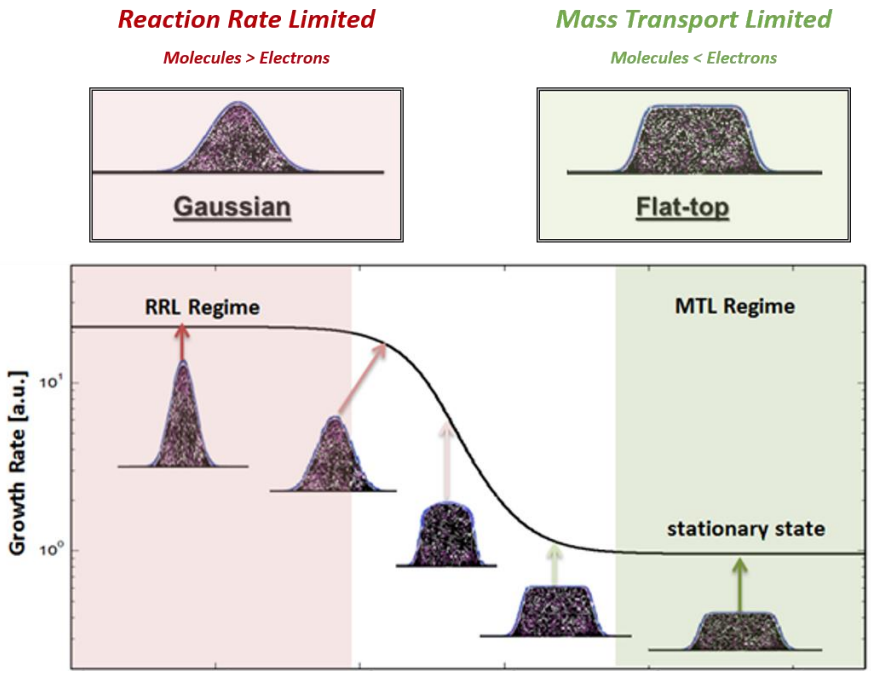

Figure 10: The working regime has a strong impact on the fabrication dynamics such as depositing rate and deposit shape. If there are more adsorbed molecules available on the surface than electrons impinging, the deposition rate is high and the deposit will emerge laterally Gaussian distributed. If there are less molecules than electrons available, the fabrication rate is lower and the deposit will be flat-top distributed.[24]

2.2.5 Adsorption Rate Model

The density of precursor molecules adsorbed onto a surface is depending on several processes. The adsorption rate model takes four individual effects into account that change the number of precursor molecules $\partial n/\partial t$ located on a certain surface area. Those mechanisms are referred to as adsorption, diffusion, desorption and dissociation[8,21,46,47]:

$$\frac{\partial n(r,t)}{\partial t} = \underbrace{sJ\left(1-\frac{n(r,t)}{n_0}\right)}_{Adsorption} + \underbrace{D\left(\frac{\partial^2 n(r,t)}{\partial r^2}+\frac{1}{r}\frac{\partial n(r,t)}{\partial r}\right)}_{Diffusion} - \underbrace{\frac{n(r,t)}{\tau}}_{Desorption} - \underbrace{\sigma\, f(r)\, n(r,t)}_{Dissociation} \qquad (3)$$

$n(r,t)$	…	*number of precursor molecules on the surface (at distance r and time t)*
s	…	*molecule sticking probability*
J	…	*molecule flux*
n_0	…	*number of molecules for a complete monolayer*
τ	…	*average molecule residence time*
σ	…	*dissociation net cross-section*
$f(r)$	…	*electron beam distribution*
D	…	*surface diffusion coefficient*

The adsorption is described by the sticking probability s, the intensity of the molecule gas flux J and the momentary molecule coverage n/n_0, where n_0 describes the highest possible number of molecules being adsorbed (there is only one monolayer allowed). Diffusion emerges if there is a lateral precursor

density gradient on the surface (due to the irradiation with electrons causing molecule depletion[21,40]) and is driven by the compensation force from diverging molecule concentrations. This effect intensifies for an increasing diffusion coefficient *D* and concentration gradient (term inside the bracket of the diffusion term in equation (3)). The desorption is inversely proportional to the residence time τ of an adsorbed molecule on a surface (spontaneous thermal desorption), and the mechanism of dissociation is depending on the net cross-section σ and the electron (beam) distribution *f(r)*, where *r* describes the lateral distance from the irradiation / electron beam center (see Figure 11). Logically, both dissociation and desorption rate increase for higher numbers of molecules *n*.

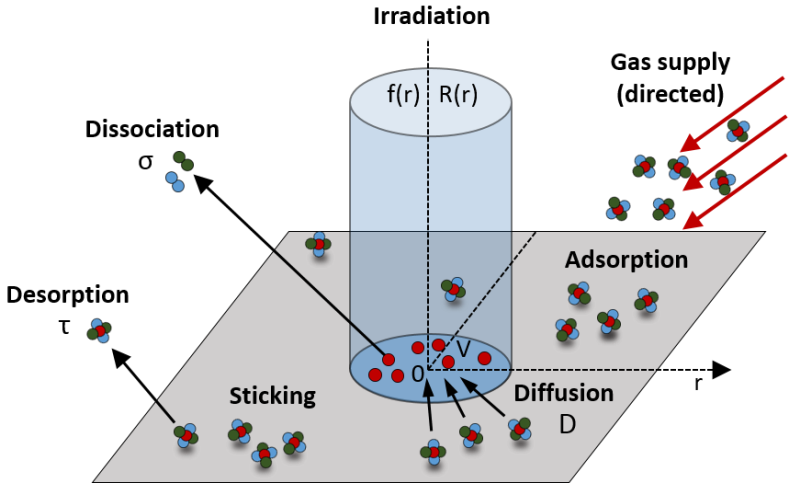

Figure 11: According to the adsorption rate model there are four mechanisms that contribute to the change of precursor molecules located on a specific surface area: 1) adsorption, 2) diffusion, 3) desorption, and 4) dissociation. Redrawn from[21].

2.2.6 Patterning Strategies

For material structuring (deposition) and examining (imaging) the electron beam scans a surface in a defined pattern, depending on the particular usage. Figure 12 depicts a raster pattern strategy that is commonly applied when doing imaging. By appropriating a raster strategy, the electron beam moves over the exposed / imaged area (blue box) in a line by line procedure (red dotted arrows). As the beam has to accomplish a horizontal movement (from the left to the right) for each line separately, the horizontal axis is denoted as fast scan axis and the vertical one as slow scan axis (red solid arrows). For special morphologies, other strategies may be used, e.g. a serpentine, a spiral-inward or spiral-outward strategy[48]. Furthermore, to prevent any morphological barriers induced by already grown structures, the pattern strategy has to be adapted in such a way that the slow scan axis is directed towards the gas flux. Already deposited structures otherwise could possibly hinder precursor molecules to replenish (adsorb and / or diffuse) to an area that is intended to be structuralized[48].

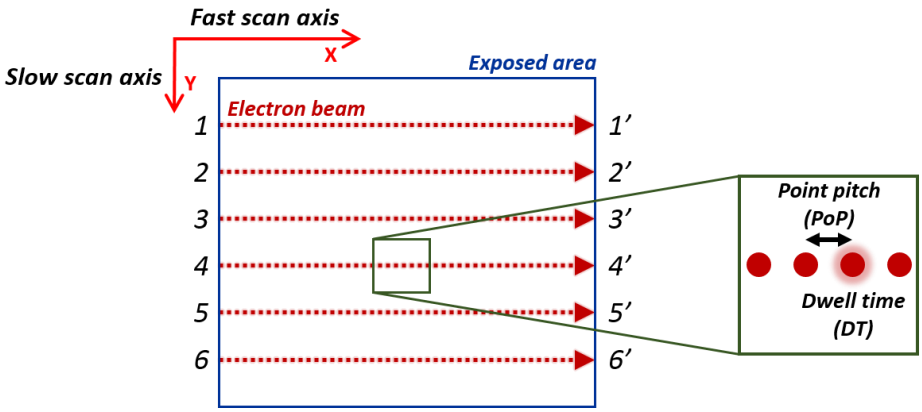

Figure 12: Scheme of a line by line scan strategy. The electron beam scans from the left to the right (main scan axis) for each horizontal line, which classifies the beam directions into a fast scan axis and a slow scan axis.

To obtain a highly precise nanostructure fabrication not only the proper choice of pattern strategy is crucial, but also further patterning parameters such as the point pitch (**PoP**), the dwell time (**DT**) and the number passes exceedingly are. The PoP is the distance between two sequentially irradiated points, the DT is the time the beam remains on each point, and the pass number describes the count of loops a beam scans over a given pattern (see right hand scheme in Figure 12). The appropriate adjustment of scan strategy, PoP, DT and number of passes is crucially decisive for deposition near the fundamental resolution limit. For approaching this limit, deposition within an RRL working regime is not optional but essential, and by having the parameters inadequately adjusted consequently thwarts the establishing of it.

As this thesis deals with single lines (i.e. bi-rings in chapter 4.1 and "L" shaped lines in chapter 4.2), the electron dose per area (see 2.3.2) conveniently will be hereinafter represented by the specific total exposure time (**S-TET**), which is the total exposure time (**TET**) divided by the PoP. The TET is the product of DT and the number of passes *n*:

$$TET = DT \cdot n \tag{4}$$

$$S\text{-}TET = \frac{TET}{PoP} \tag{5}$$

A significant drawback of the used technique is that the stage on which a sample is mounted on is not absolutely motionless (in terms of nanometers), which may cause structural broadening when the fabrication is conducted with a large number of passes. For this reason a multiple pass pattern strategy often has been eschewed when doing high-fidelity deposition at nanoscale[41,49]. As in this work a multiple pass pattern strategy was required, a waiting time of > 30 min between selecting the deposition area (by actively moving the stage) and starting the deposition process was implemented on all experiments. The additional time was deemed necessary to minimize the influences of a drifting stage.

2.3 Purification

The realization of plasmonic MTMs via FEBID requires a very accurate and precise fabrication. The dimensions of the structures intended to be fabricated in this work (chapter 4.1) were considered being near or beyond the current resolution limit. What makes this task even more challenging is the carbon contamination within the deposit, which inevitably has to be removed subsequently after deposition, as the plasmonic MTM response relies heavily on achieving a sufficiently metallic optical conductivity. For conventional as-deposited FEBID structures, the resulting metallic nanoclusters in a residual organic matrix will generally have a degraded optical conductivity[50] in particular, due to increased scattering at grain boundaries. Studies of the impact of the nano-granular morphology with FEBID on optical-MTM performance are apparently lacking up to now. To overcome this limitation, Geier et-al[51] demonstrated a post-fabrication purification approach which provides pore- and crack-free high-fidelity shapes with a pure metal character as needed for plasmonic applications. The purification is done via the approach by Geier et al. by using the *FEI Quanta 200 ESEM*.

2.3.1 Environmental Scanning Electron Microscope

An environmental scanning electron microscope (**ESEM**) is basically a SEM that allows working with higher chamber pressures.[13,52,53] The conventional SEM requires a high vacuum level (see chapter 2.1.2), which heavily limits the range of usable samples, as they need to be dry and clean. An additional constraint for the applicability in a SEM is the required conduciveness of a probe. This is explained by the charging effect that emerges when electrons impinge on a sample which is not conductive. In this case, a sample would be continuously charged negatively until the electrons get repelled from the surface before reaching it, making any reasonable processing impossible. However, an ESEM allows the usage of non-conductive samples, as the chamber atmosphere causes the charges on a (non-conducting) sample to be compensated by ions generated by the permanent collisions of electrons and atmosphere molecules.[13,53]

The vacuum system of an ESEM is multi-staged, as visualized in Figure 13. The pressure is increasing from the gun chamber (which requires ultra-high vacuum) to the sample (low vacuum up to atmospheric pressure) via several vacuum chambers that work separately but are connected by orifices. The last (at least two) orifices are termed pressure limiting apertures (**PLA**) and are highly essential elements in the functional principle, as only their implementation enable a high pressure gradient.[13,53] The *Quanta 200 ESEM* uses a five-stage vacuum system.

The ESEM chamber can be filled with several gas types - a common one is H_2O. The application of a water vapor atmosphere allows in-situ investigations on a range of sample types, specifically biological probes that need to remain wet, or insulating probes.[13,53]

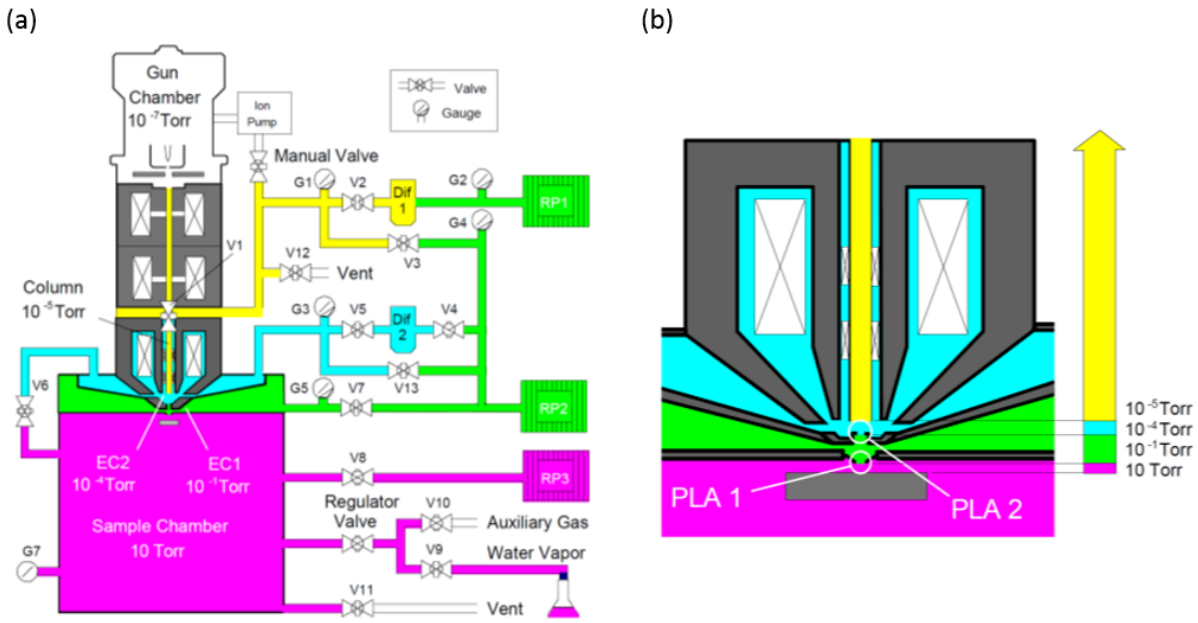

Figure 13: (a) Sketch of the multistep pumping process of an environmental scanning electron microscope (ESEM). The pressure increases from the gun chamber to the sample chamber by individual pumping systems. (b) Close-up of the pressure limiting apertures (PLA) that separate the individual pressure regions. (Note the caption: 1 Torr is roughly 1.33 mbar or 133.3 Pa).[53]

2.3.2 Purification Process

In 2014, Geier et al. successfully demonstrated an electron beam assisted approach for purifying Pt-C deposits by using a H_2O vapor atmosphere at room temperature[9,51]. This procedure takes the ability of the electron beam to separate H_2O molecules into H and O atoms, which subsequently bond to the carbon atoms within the bulk matrix, forming volatile CO, CO_2 and CH_X molecules that get pumped away[9]. Geier et al. demonstrated the feasibility to remove the carbon fraction from deposits by purifying solid pads with typical lateral dimensions of 2 × 2 µm. The pads were deposited with the $MeCpPt^{IV}Me_3$ precursor on Si substrate. TEM investigations of the pad cross sections, visible in Figure 14, revealed that the as-deposited (unpurified) structure layers having Pt grains of size of 2 - 3 nm embedded into a carbon matrix (a). As recognizable in (b), the purification is a bottom-up process starting on the lowermost layers. It could be shown that the low energy SE are mainly responsible for the purification processing owing to their large cross section. Fully purified structures revealed being pore, crack and carbon free with Pt grain sizes of 6 - 9 nm (c). The volume of the deposit decreased by roughly 69 vol.%. The mass loss proceeded primarily in height (vertically) while the lateral extensions remained relatively constant.[9]

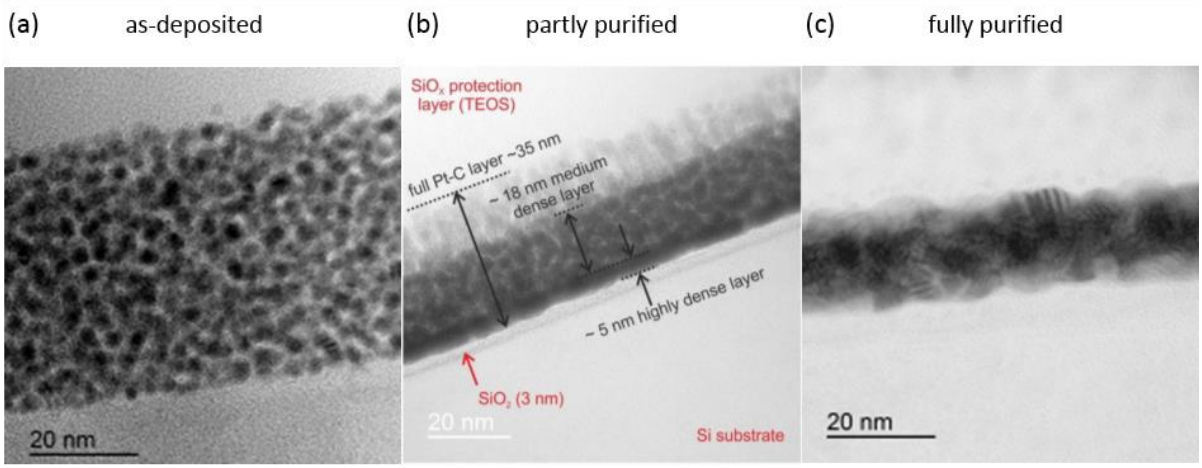

Figure 14: TEM image of the cross sections of solid pads with lateral size of 2 x 2 µm, deposited on Si by using the Pt precursor. (a) The unpurified deposit shows Pt grains embedded in a carbon matrix. (b) The purification is a bottom-up process that starts decarbonizing at the lowest layer. (c) A fully purified deposit is free of pores, cracks and carbon. The volume loss of roughly 69 vol.% affects the structure height almost solely (vertical shrink).[9]

The electron dose (charge per area) deployed for purification is given by equation (6) and must be adapted to the respective deposit size / thickness separately. The parameter setting in the *Quanta 200 ESEM* works partly differentially to the *NOVA 200* regarding DT (adjusted via scan speed), PoP (adjusted via magnification and number of pixels in the scan frame) and beam current (adjusted via electron beam spot size)[7]. For reasons of simplicity, the electron dose is frequently expressed as beam current times purification time divided by purification area[7,9]:

$$D = \frac{Q}{A} = \frac{I \cdot t}{A} \tag{6}$$

D … *electron dose*
Q … *charge*
A … *area of the scan frame*
I … *current of the electron beam*
t … *purification time*

2.4 Atomic Force Microscopy

An atomic force microscope (AFM) is a scanning probe microscopy technique that enables morphology investigation down to the sub-nm range[54]. The operating principle of an AFM is based on rastering a surface with a fine tip in a line by line pattern, similar to the scan strategy displayed in Figure 12. In its simplest form, the system records the height profile for each line, from which a 2D image is generated. A visualization of the setup is found in Figure 15: A tip with a radius of several nanometers is connected to a cantilever, which itself is mounted onto a scan head. The scan head is movable in x-, y- or z-direction to allow scanning in several directions (x, y) and adjusting to the required cantilever-surface distance (z). A laser is pointed to the topside free end of the cantilever and is reflected onto a positioning sensing detector (**PSD**) for data acquisition. If the cantilever bends due to height variations,

the reflected laser gets displaced from the PSD causing a signal shift, which then gets transferred to a computer to generate a height profile.[55] In this thesis all AFM measurements were performed with a *Bruker Dimension Fastscan*.

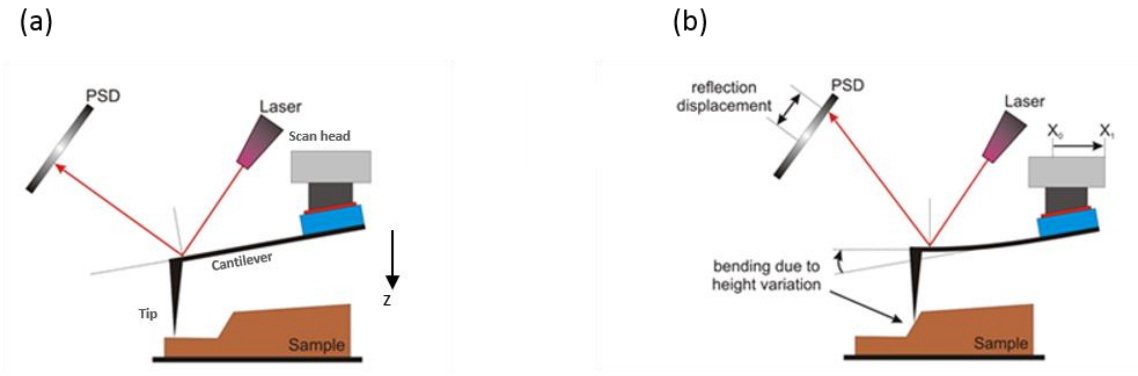

Figure 15: Principle setup of an atomic force microscope (AFM). (a) The essential components are scan head, cantilever, tip, laser and position sensing detector (PSD). (b) A change of sample height is detected via cantilever deflection, causing the reflected laser to induce a signal shift on the PSD. By scanning several lines, a 2D height profile can be computed.[55]

While coarse motion is done mechanically, fine positioning is realized via actuators that are implemented within the scan head, capable to shift the cantilever with precision in the picometer range. Those actuators are piezoelectric crystals attached to electrodes. Applied voltage causes the crystals to expand or contract (depending on whether the voltage is positive or negative), as shown in Figure 16(a). Altering the lateral cantilever position (x and y) is realized by a piezo tube scanner with two pairs (for x and y-direction) of electrodes (Figure 16(b)). Each pair has its electrodes positioned oppositely. The tube scanner bends if an electrode set is provided with opposite voltages (as one side then is elongated and the other one shortened).[55]

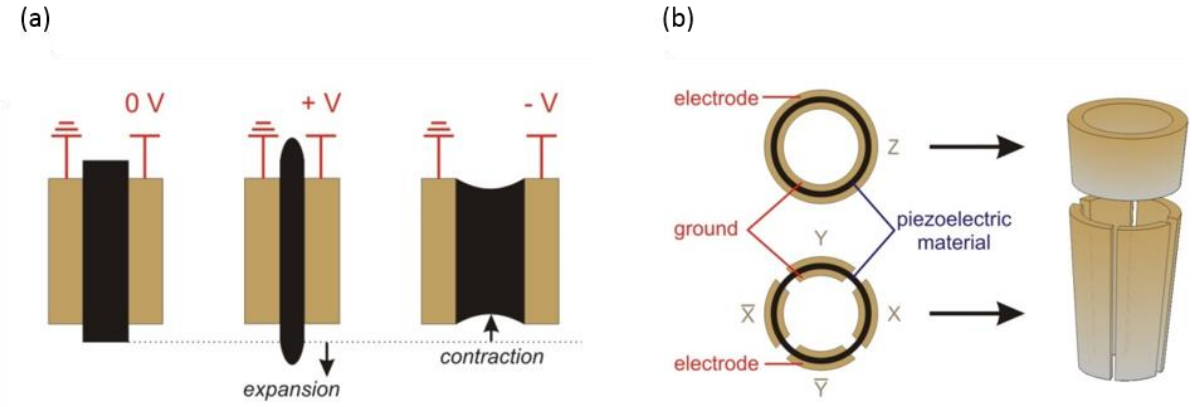

Figure 16: (a) Concept of the piezoelectric actuator for z-positioning: An applied voltage leads to expansion / contraction of the crystal that precisely changes the position of the cantilever. (b) Piezo tube scanner for changing x- and y- position. Electrodes are attached to piezoelectric crystals on the two opposite sides (for x- and y-direction respectively). The tube bends if opposite voltages are applied.[55]

There are two prevailing forces between tip and surface when the cantilever is approaching the sample: Van der Waals (**VdW**) force and Pauli repulsive fore. While the Van der Waals force is dominating at distances of 10 to 5 nm, the Pauli repulsion strongly kicks in for distances below 2 nm. The Pauli repulsion stems from the Pauli exclusion principle, which prohibits two electrons being simultaneously in the same quantum state. The VdW potential and the potential from the Pauli repulsion together form the Lennard-Jones potential[55]:

$$V_{LJ} = V_{VdW} + V_{rep} = -a \cdot r^{-6} + b \cdot r^{-12} \tag{7}$$

V_{LJ} … *Lennard-Jones potential*
V_{rep} … *Van der Waals potential*
V_{VdW} … *potential from Pauli repulsion*
a, b … *constants*
r … *tip-surface distance*

As evident in equation (7), VDW and Pauli repulsion compete each other, leading to a potential minimum (an equilibrium between attractive and repulsive force) at a certain tip-surface distance. The situation is also visible in Figure 17, showing the respective potentials / forces in dependency of the tip-surface distance: When the tip approaches the sample, it gets attracted by the far-reaching VdW force at first (green area), bending the cantilever towards the surface. At a specific distance (depending on the cantilever geometry) the force surpasses the threshold force of the cantilever (green dashed line), causing the cantilever to snap into physical contact with the sample ("jump to contact"). At contact, the force (black curve) is zero as the Lennard-Jones potential (blue curve) is being minimized there.

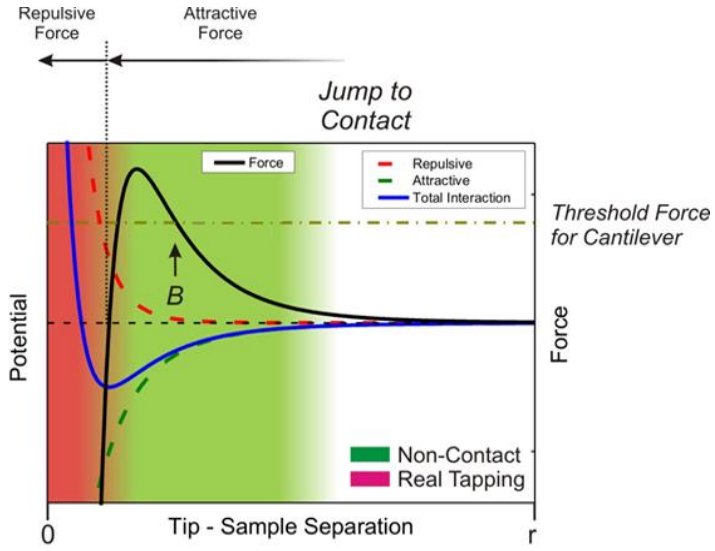

Figure 17: Potential and force in dependence on tip-sample distance. The Lennard-jones potential (blue curve) is a convolution of the Van der Waals (VdW) potential (green dashed curve) and the potential from Pauli repulsion (red dashed line). By approaching the cantilever towards the sample it gets attracted by the far-reaching VdW force (black curve in green area). At a certain distance (B) the cantilever threshold force is surpassed by the VdW attraction force causing the cantilever tip to snap physically onto the surface ("jump to contact"). The force stemming from the Pauli repulsion then strongly kicks in and disallows the tip to penetrate into the (solid) sample. For highly precise measurements in tapping mode, reaching into the repulsive regime (red area) is considered necessary.[55]

There are several opportunities existing for the morphology detection, which include the contact mode, non-contact mode and intermittent-contact (tapping) mode. These mode types differ from one another in terms of how the cantilever is sensing the surface. In contact mode, the tip constantly contacts the sample. Height differences are perceived either as cantilever deflection (constant height mode), whereby the scanner is fixed in the z-position, or as position in z-direction of the scanner (constant force mode), where by the deflection of the cantilever is fixed. The contact mode allows high scan speed and resolution, but has its disadvantage in the risk of surface destruction, delamination or material removal (see Figure 18). Moreover, a fluid film on the surface ("wetting layer") commonly distorts measurement results (though to a small extend). In non-contact mode the cantilever oscillates closely above the surface without touching it. This technique is utilized for more specific applications such as determining electrical / magnetic charge distributions. The mode that is exclusively used in this thesis is the tapping mode, which is a combination of constant and non-constant mode: The cantilever oscillates (permanently externally driven) above the surface at such a low distance that there is an energy exchange from the cantilever to the sample proceeding. In addition to the height data derived from the z-position of the scanner (similar to the constant force mode), there are phase data obtainable that possibly give information of various material properties. Phase data are deduced from the phase shift caused by the tip-sample interaction. The cantilever oscillation is manipulated either by attraction (attractive regime, in which the phase shift is negative) or by repulsion (repulsive regime, in which the phase shift is positive). For performing highly a precise morphology determination, which had been required in this thesis, it is inevitable that AFM measurements are conducted within the repulsive regime. The reason for this is the nearly throughout existing wetting layer on the sample surfaces, which only then is of no virtually consequences if the tapping mode is performed within the repulsive regime. In the attractive regime though, the cantilever has lower vibration energy and the tip is therefore influenced by the liquid layer in a much greater degree. Despite the reduced tip-sample interaction in tapping mode compared to contact mode, surface damage is still possible, especially by working in the repulsive regime.[55]

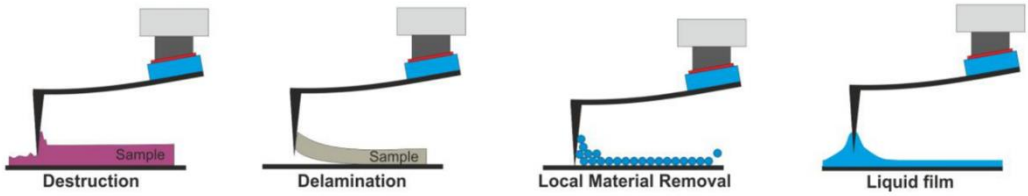

Figure 18: Destruction, delamination or material removal are possible sample damages caused by direct tip-sample interaction when doing AFM measurements. The wetting layer is almost invariably present, which is why in this thesis the tapping mode was required to be performed within the repulsive regime.[55]

Another hindrance is the accurate determination of sample morphologies is the lateral broadening due to tip superposition. Since a tip naturally has a finite extent, the measured lateral dimension of an examined structure is a convolution of the actual morphology and the tip geometry, as visible in Figure 19. Hence, AFM tips should be preferably as small as possible (compare (a) and (b)). AFM tips typically have to be replaced relatively often due to tip impurities (resulting from dirty samples or destructured, delaminated or removed material). A filthy tip is recognizable by a one-sided broadening and generally has to be replaced. All AFM measurements in this thesis were performed by using the tip model *RTESPA-300* by *Bruker*.

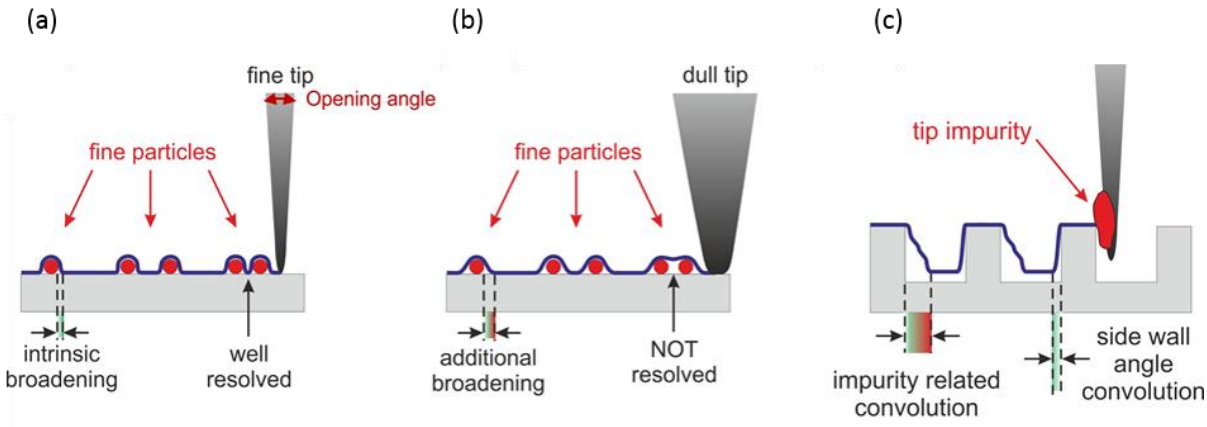

Figure 19: Tip convolution leads to structural broadening. For highly precise lateral measurements, a tip is required to be as fine as possible ((a) vs. (b)). (c) Tip impurity is a frequently occurring effect and is easily discernible by a unilateral broadening. For obtaining precise results, a filthy tip has to be replaced.[55]

2.5 Determination of Plasmonic Activity

Plasmons are collective oscillations of the electron gas within a metal, technically feasible in metal nanoparticles. The fundamental principle is that an electric field forces the electrons within a metallic object to get displaced in one direction, creating charge separation. If the electric field stops impinging upon the charge carriers, they try to enter equilibrium again and subsequently start to oscillate, analogue to a mass mounted onto a spring. The electrons themselves are creating electromagnetic fields by oscillating. The coupling of oscillating particles inside and electromagnetic fields outside the particles is referred to as plasmonic resonance (or surface plasmons). For particles at nanoscale, the coupling between light and surface plasmons are relatively strong.[56]

In its first experimental section, this thesis focuses on the precise fabrication of metallic nanostructures that are intended to exhibit plasmonic resonances in a very distinct frequency range (see chapter 3 and 4.1). The determination of their functionality was subsequently conducted by the work group around Prof. Roskos at the Goethe University Frankfurt (Germany). There, the transmission spectra were measured in a microscope-spectrometer of in-house design based on a conventional optical microscope, using a high-power continuous-wave xenon lamp source, fiber-coupled via a monochromator to the microscope that is equipped with an additional objective (100×) from below to focus the light through the sample, with an avalanche photodiode detector in the output port of the microscope. A representative transmission spectrum (relative to a mask on the same substrate without nanostructures) for Au samples is shown later in Figure 34 (chapter 4.1). The presence of a MTM resonance with a comparable transmission minimum in this spectral range is also predicted on the basis of electromagnetic simulations (*CST Microwave Studio*).

3 Related Previous Work

As a starting point, this section gives a brief overview on several previous findings this master thesis is built on. The focus of this study has been on the precise fabrication of challengingly small dimensioned structures in the two-digit nanometer scale, whose basic feasibility had already been proven by U. Haselmann in his master thesis[7]. The relevant results found by Haselmann et al. are curtly summarized (chapter 3.1).

3.1 Plasmonic Gold Nanostructures

In 2016 U. Haselmann et al. had successfully produced solid, plasmonic and carbon free nanoscale Au discs using the Me_2-Au(acac) precursor via FEBID[7] via post-growth purification in H_2O atmospheres together with a scanning electron beam. Further emphasis was put on a bi-ring shaped structural geometry that is expected to provide unique plasmonic characteristic. According simulations conducted by the work group around Prof. Roskos at the Goethe University in Frankfurt predicted multiple plasmonic resonances in the THz range for pure Au bi-ring deposits, as discussed in more detail in chapter 4.1 and Figure 26. The sketch of the aimed structure is depicted in Figure 20. These bi-rings were set to have inner and outer diameters of 165 nm and 65 nm, respectively, a line width of 25 nm and a ring height of 5-15 nm, combined with a rectangular cross section. The deposits are required to be produced within a 5 x 5 µm² Au aperture window (enabling the subsequent measuring of the plasmonic activity) on a glass / ITO layer stack (enabling electron withdrawal). More details will be given in chapter 4.1 and Figure 25.

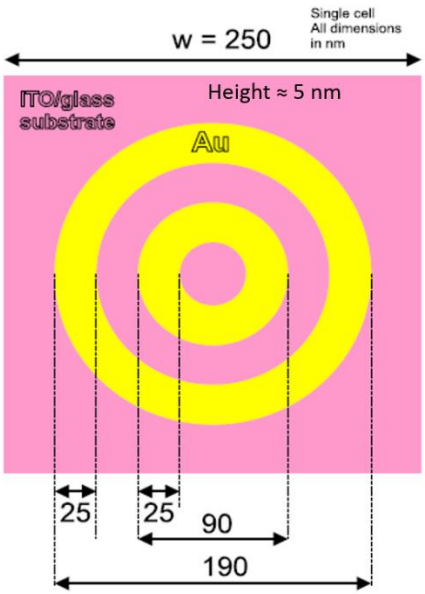

Figure 20: Sketch of an Au bi-ring for plasmonic response simulations conducted by the workgroup of Prof. Roskos at Goethe University Frankfurt (Germany). With intended inner and outer line diameters of 65 nm and 165 nm, respectively, a line with of 25 nm and a line height of 5-25 nm, the dimensions are near the resolution limits of FEBID. In particular, the assumed rectangular cross section is very challenging for FEBID on that scale. The Au bi-ring is supposed to be deposited within a 5 x 5 µm² cavity and on an ITO / glass layer stack (see 4.1 and Figure 25).[7]

Haselmann et al.[7] explored on the fabrication aspects and pursued the feasibility of structures considered being close the fundamental resolution limits of FEBID technique. Based on preceding findings[49,41] framework configurations already were known, which included a beam voltage of 30 keV, a beam current of 21 pA and, as discussed in 2.2.3, and a carefully adjusted GIS[48]. The structures were fabricated on an ITO / glass layer stack substrate and exclusively deposited via single pass strategy to avoid unwanted broadening by stage drifts influences. Figure 21(a) shows two different main sets using point pitches (PoP) of 1 nm and 10 nm to study typical border values. Both sets reveal downscaling sweeps from 510 and 205 nm to 340 and 140 nm to 170 and 70 nm (outer and inner ring, respectively). In each set, the specific total exposure time (**S-TET**) was varied from 3.0 over 4.5 to 6 nm / s to study the thickness scaling and its implications on the achievable widths. Furthermore, as essential in FEBID, the patterning strategy was varied by means of the ring sequence (outer - inner and inner - outer). Figure 21(b) shows a close-up of the 10 nm PoP downscaling array with the most favorable inner - outer patterning strategy.

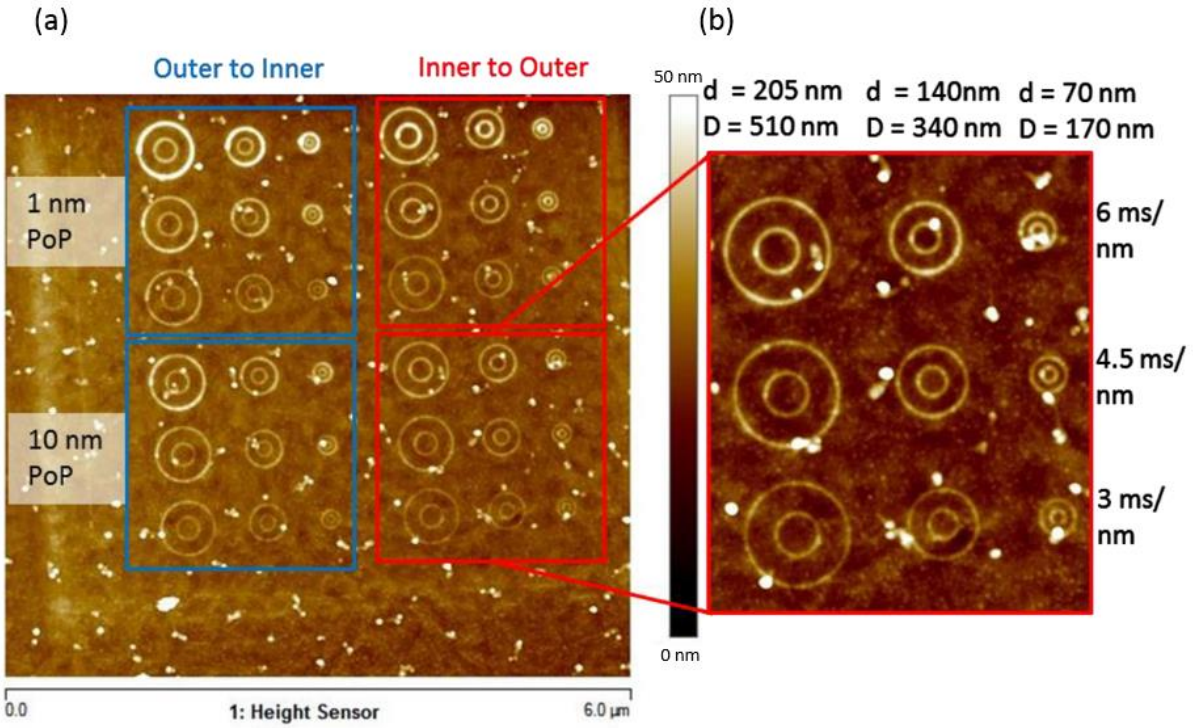

Figure 21: (a) AFM height image of various sized as-deposited Au bi-rings on an ITO layer fabricated at various S-TET, PoP and pattern strategies. All bi-rings were deposited using a single pass pattern strategy. The upper sub-array was done at 1 nm PoP, which resulted in a faster but also less controllable depositing mechanism compared to the lower sub-array made at PoP of 10 nm. The sub arrays marked by the blue squares refer to an outer to inner pattern sequencing, i.e. the outer ring is fabricated prior to the inner ring. The inner to outer pattern sequencing indicated by the red squares is superior due to a better precursor replenishment. (b) Magnified image of a sub-array made with 10 nm PoP, Inner to outer pattern strategy and varying S-TET (Note: Letter "d" represents the inner ring diameter and letter "D" the outer ring diameter). The usage of shorter S-TET also led to lower structures.[7]

In summary, no critical impacts were found on the deposits that had led the downscaling be unfeasible. The height tunability was, as expected, given by the S-TET (a longer S-TET generally leads to higher deposits[23]), while the height accuracy was not significantly affected by a change of the S-TET. An inconsistency between inner and outer ring arose when an outer to inner pattern strategy was applied, as the inner rings consistently remained distinctly lower than the first made outer rings. This fact has been attributed to a worse initial precursor gas situation for the inner to outer pattern strategy. Also, the inner rings were broader than the outer rings, which indicated a better precursor gas situation for rings that were produced at first. Therefore, an inner to outer pattern strategy was maintained providing a more accurate operability. Deposits made using 10 nm PoP emerged as being more controllable due to their linear growth behavior compared to deposits made using 1 nm PoP. To achieve deposit heights of 15 - 45 nm, which was equivalent to 5-15 nm due to the subsequent volume loss as a result of the purification step (chapter 2.3), a PoP of 4 nm had been chosen. This was considered being an appropriate compromise between the fast growth performance of 1 nm PoP and the accuracy of 10 nm PoP. The most important change, however, was the change from single- to multi-pass patterning since the aimed bi-ring height was not possible to achieve, unless the S-TET had been increased higher than 6 ms / nm. At such high S-TETs the deposits start to lift off from the surface (transition area to true 3D fabrication). Increasing the specific exposure time was not an option that could lead to a satisfying result, hence switching to a multiple pass pattern strategy was enforced.

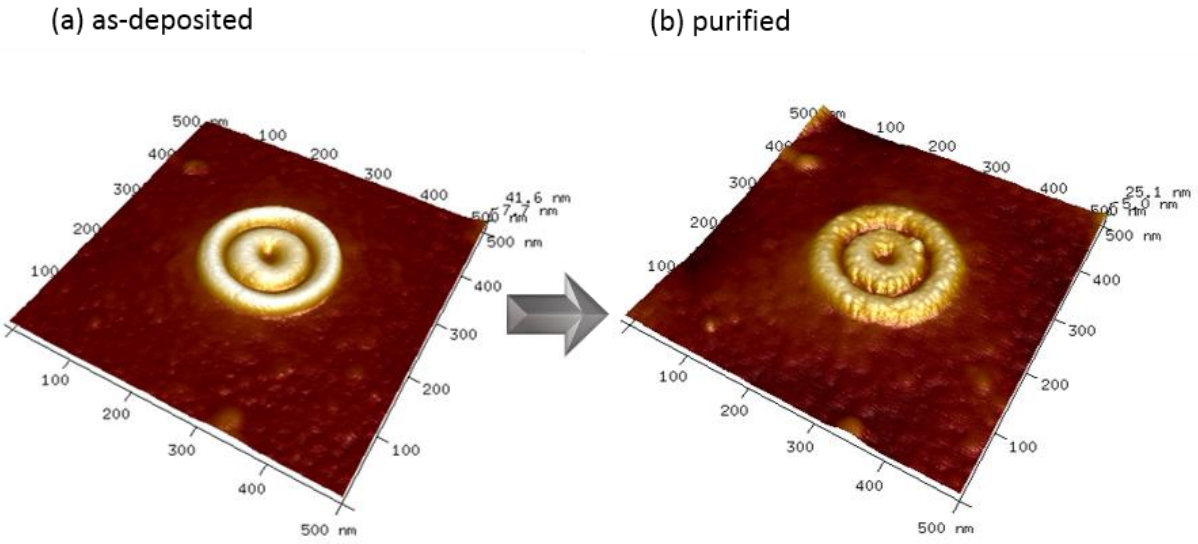

Figure 22: AFM height image of an Au bi-ring within a cavity before and after purification. (a) The bi-ring was deposited with an S-TET of 32 ms / nm using 4 passes (inner ring) and an S-TET of 56 ms / nm using 7 passes (outer ring). This parameters choice revealed the ring lines being too bulky. (b) After purification, the bi-ring featured a height loss of nearly two-thirds and, most importantly, kept its shape. For imaging, a plain fitting of the surface was done to compensate the disrupted ITO substrate.[7]

Further deposits were made within a cavity / Au window of 300 nm depth (see scheme in Figure 25(a)). This exposed another important facets the growth behavior concerning, as the cavity significantly provides an improved gas replenishment situation that leads the growth rate being increased by a factor of 3 - 4. Also a height difference between inner rings and outer rings was found, leading the

outer rings being developed more dominant. Therefore, a dynamic parameter adaption was implemented by depositing the inner rings with less passes (equivalent to a shorter S-TET) than the outer rings to gain a more accurate homogeneity in height.

The as-deposited structures had inner rings fabricated with 4, 5 and 6 passes and outer rings fabricated with 7, 8 and 9 passes, with each pass corresponding to an S-TET of 2 ms / nm. The line height varied from 32 - 42 nm for both inner and outer lines. Comparison of inner and outer ring line widths revealed a serious disadvantage when using separate number of passes: While the outer lines yielded line widths (FWHM) varying from 30 to 34 nm, the inner lines had them 39 to 48 nm.

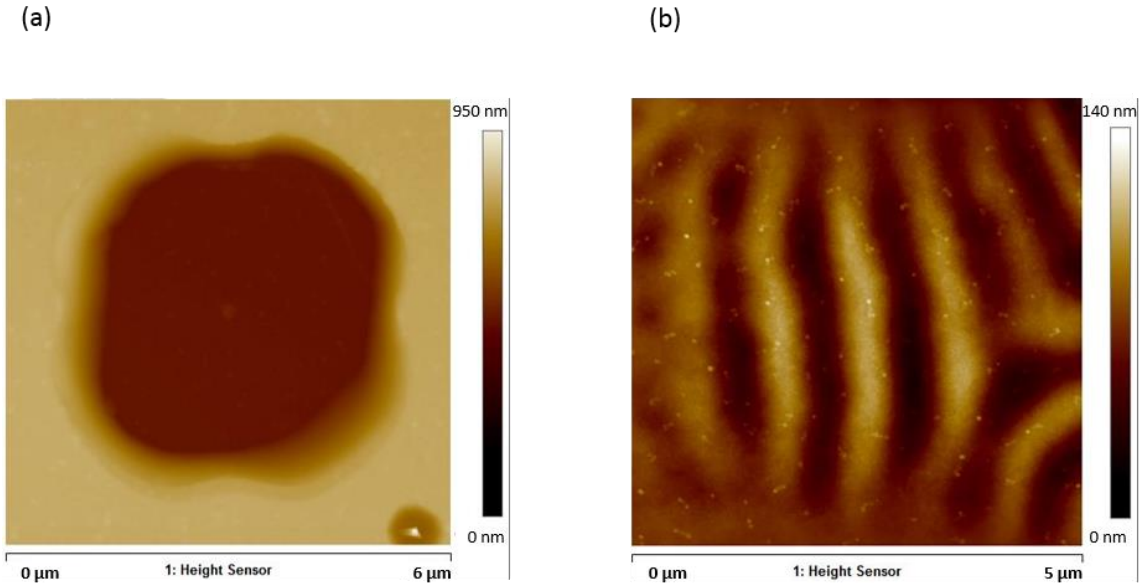

Figure 23: (a) AFM height image of a cavity with size of 5 x 5 µm² and depth of 300 nm. The deposition inside the cavity led to higher structures due to a better gas replenishment situation. (b) ITO substrate arching after purification using 5 keV, 5 nA, 1 µs DT, 10 nm PoP, 10 Pa H_2O pressure and 60 C / cm².[7]

Subsequently, a purification step was conducted at 5 keV, 5 nA, 1 µs DT, 10 nm PoP, 10 Pa H_2O pressure and an electron dose of 60 C / cm² as introduced by Geier et al.[51]. This procedure has the advantage to entirely remove the carbon without disrupting the surface morphology by pinholes and / or cracks. The only change is a height loss of 57 - 65 rel.% after purification in agreement with the initially incorporated carbon amount. Figure 22(a) shows an as-deposited bi-ring within a cavity, fabricated with 4 and 7 passes (inner and outer ring, respectively). The inner ring revealed a line height of 32 nm at a FWHM of 37 nm, while the outer ring revealed a line height of 36 nm at a FWHM of 31 nm. After purification (see Figure 22(b)), the inner and outer rings revealed FWHM of 35 nm and 40 nm, respectively, and a height of 15 nm for both inner and outer rings (Z scales are adapted to recognize the details of interest). Most importantly, the rings kept their shape and did not crack during purification as mentioned above. This has been considered a major requirement for further research as initially described in this chapter.

The purification step also revealed a drawback of the ITO substrate that has not been fixed yet: It was observed that after the purification process the ITO surface massively arched. This resulted in a wavy surface structure with height differences between maxima and minima up to 70 nm that potentially could disrupt the performance of plasmonic devices seriously (see Figure 23(b).

In summary, previous work provided a clear picture about the fabrication parameters, the patterning strategy and confirmed the compatibility with the H_2O based, electron beam assisted purification process to provide compact, non-disrupted nanostructures composed of pure gold for plasmonic applications. Based on these protocols, the further purpose was to arrange the bi-rings in an array to reveal collective plasmonic activities in a well-defined wavelength range (THz frequency) which is the main subject of this master thesis.

4 Experiments and Results

The targeted aim of this thesis was to proof the feasibility of specific, circular shaped electromagnetic Au metamaterials (**MTM**) via FEBID and to achieve further knowledge on the depositing behavior when using the Me_2-Au(acac) precursor, along with new insights on the principal patterning resolution limits attainable. All deposits were created within the dual beam microscope (**DBM**) compounded by a scanning electron microscope (**SEM**) and a focused ion beam (**FIB**). Selected deposits were purified using an environmental electron microscope (**ESEM**) and analyzed via DBM and atomic force microscopy (**AFM**).

By having the general feasibility of single Au bi-rings be proven by U. Haselmann (previous chapter), the next step was to fabricate an array of homogeneously distributed and fully purified Au bi-rings, which thereby satisfy the required geometries.

First of all, an array sequence optimization was done (chapter 4.1.2), as it turned out depositing several Au bi-rings subsequently next to each other led to precursor depletion. That emerged as central aspect in realizing plasmonic devices at nanoscale and mainly set up the basic subject of this master thesis. An on-ring fine tuning was accomplished (chapter 4.1.3) to counteract the prevalent spatially varying volume growth rates of the bi-rings by performing a dwell-time adaption. Nevertheless, bi-rings fabricated within the required cavity of 300 nm depth, exposed a new challenge due to an inhomogeneous gas distribution, which resulted in deposit height variations (chapter 4.1.3). As-deposited structures (Au / C matrix) generally contain about 8 at.% Au[8], therefore the fabrication of reliably working MTM required an increase of the Au content, which made a purification step necessary. During purification similar problems arose as seen in the study before (chapter 3.1), causing a massive wrinkling of the ITO layer. Three unpurified and one purified bi-ring array was sent to the group of Prof. Roskos from Goethe University in Frankfurt to study their plasmonic response behavior. Although having several performing limitations left unfixed, e.g. the deposit height variation, the ITO arching and too broad bi-ring line widths along with non-rectangular cross sections, the structures indeed revealed plasmonic behavior in the wavelength range of 550 to 800 nm (chapter 4.1.5). Also the non-purified structures unveiled plasmonic response, even if less distinct than the purified one. All bi-ring fabrication and purification processes were done jointly with DI J. Sattelkow. An overview of topics, objectives and the work-flow of this master thesis are depicted in Figure 24.

Although successful, it is here important to understand that the fabrication was incrementally tailored for the final application. For a more general applicability, however, this approach is not favorable as the adaption is time consuming. Hence, it was necessary to understand what influences the achievable structure dimensions to get a more general picture of the situation. Thus, it was decided to make a step back and gain deeper knowledge on the deposition performance (chapter 4.2). Simpler structures, referred to “L-shaped structures”, were fabricated on which the growth dynamics of the Au precursor could be ***1)*** compared to the well-known Pt precursor and ***2)*** understood in a more universal way. Based on the broad in-house knowledge using the Pt precursor, first experiments were done, which focused on the defined control of structure heights and achievable homogeneity (chapter 4.2.2). In a second step, the experiments were expanded to the intended Au precursor using the same strategy. The depositing dynamics of the Au precursor was then compared to those of Pt (chapter 4.2.3) to separate material dependent influences. Additionally, experiments were conducted to check if there is a correlation between synchronizing the pattern sequencing to the power line frequency (50 Hz) and

obtaining enhanced deposit geometries (chapter 4.2.4). The final part of this master thesis then focused on approaching the highly desired electron limited regime in which smallest feature sizes and most homogeneous thicknesses can be achieved. In chapter 4.2.5 It is successfully demonstrated how these regime conditions can be established and also set a new benchmark of line widths in the sub 13 nm regime at heights > 8 nm. By that, the work provides the fundamental framework for further tasks in the field of additive, direct-write fabrication of high-resolution structures for plasmonic THz applications.

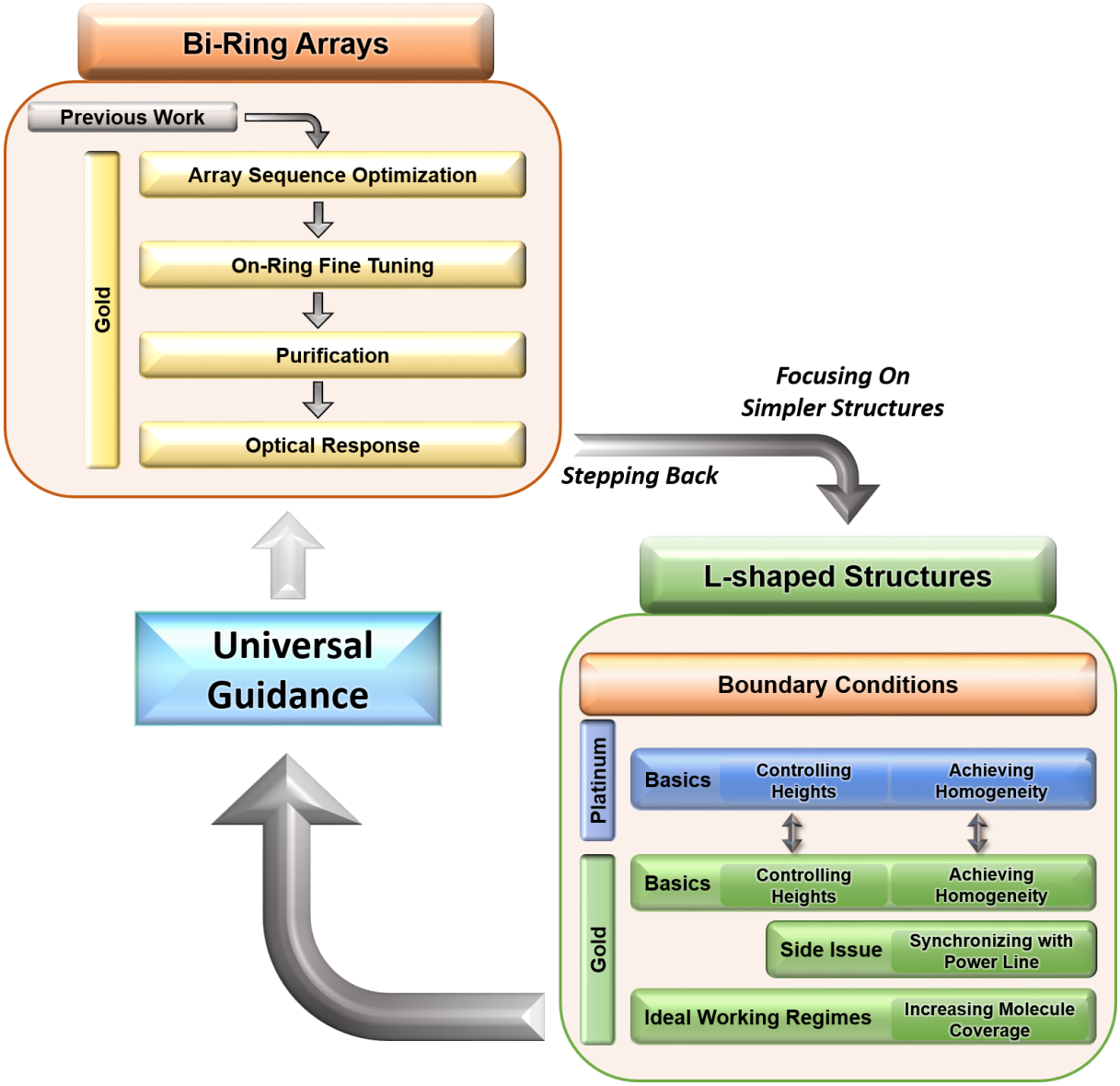

Figure 24: Overview of the two main subjects of this thesis: Based on previous work, the first aim was to create a system of plasmonic Au bi-rings (top left). In order to gain further knowledge required to obtain nanostructures at high precision, this thesis focused on simpler structures in its second stage (bottom right).

4.1 Plasmonic Au Bi-rings

Compared to other MTM cell patterns (e.g. split-rings[57]), the transmission resonances of bi-ring structures do have a particularly low sensitivity to the angle of incidence, which is advantageous for measurements with tightly focused beams. The bi-ring structures were initially realized via FEBID using the Au precursor and prepared on a commercial glass substrate coated with an ITO layer (15 - 25 Ω sq.) for electric contact as required during charged particle based FEBID processing. In this chapter, the optimization of process parameters and scan strategies to achieve pure Au bi-rings with heights ≥ 5 nm, inner and outer diameters of 65 nm and 175 nm, respectively, and line widths of 25 nm, all arranged in a 12 × 12 array, will be discussed. The final bi-ring array was deposited within a square mask with size of 5 × 5 µm^2 to block interfering light when doing measurements for determining the plasmonic activity. Figure 25(a) shows a scheme about the required setup together with a representative real FEBID array in Figure 25(b) by an AFM height image.

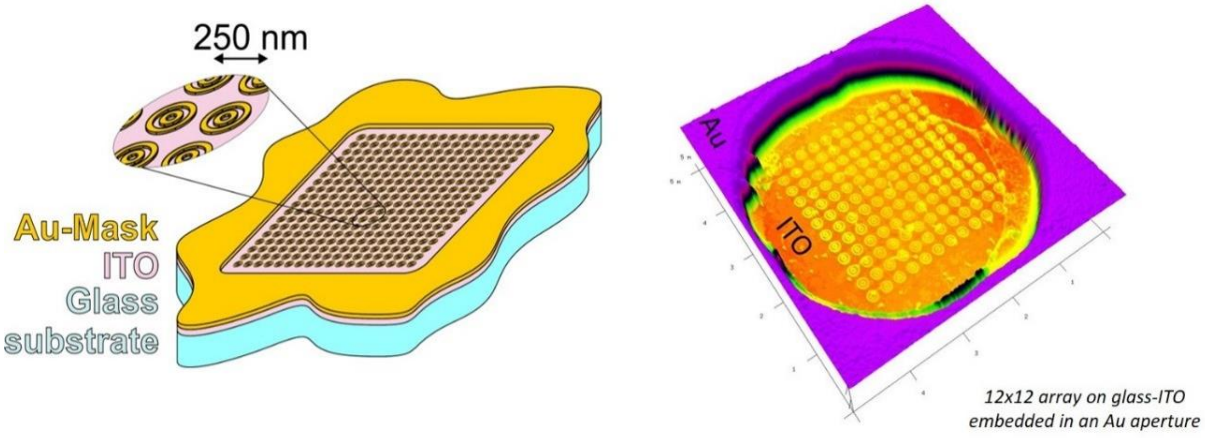

Figure 25: Left: Schematic bi-ring array on an ITO / glass layer, embedded in a 5 x 5 µm² Au window. Right: AFM 3D height image of a real as-deposited Au bi-ring array.

Several simulations had been executed by the work-group of Prof. Roskos, which claim that a 12 × 12 array of bi-rings at the given dimensions is expected to have resonances in the visible and near-infrared wavelength range. The diagrams in Figure 26 show the computed absorption curves for arrays with heights of 20 nm (a) and 5, 10, 20 and 25 nm (b) for different spectral ranges. In particular, the simulations shown in Figure 26(b) reveal that dynamic absorption peak and intensity shifts in dependency of bi-ring heights making clear their strong implications. These data also point out the required accuracy during FEBID fabrication as even small deviations might broaden the peaks and reduce the absorption intensities. As producing purified bi-rings with heights > 10 nm combined with line widths < 25 nm initially seemed not being realizable, an array height of 5 to 10 nm instead had be considered being feasible. The first subtopic concerns the question of how an array could be homogeneously fabricated, which strategies should be applied for and what are the crucial factors to avoid.

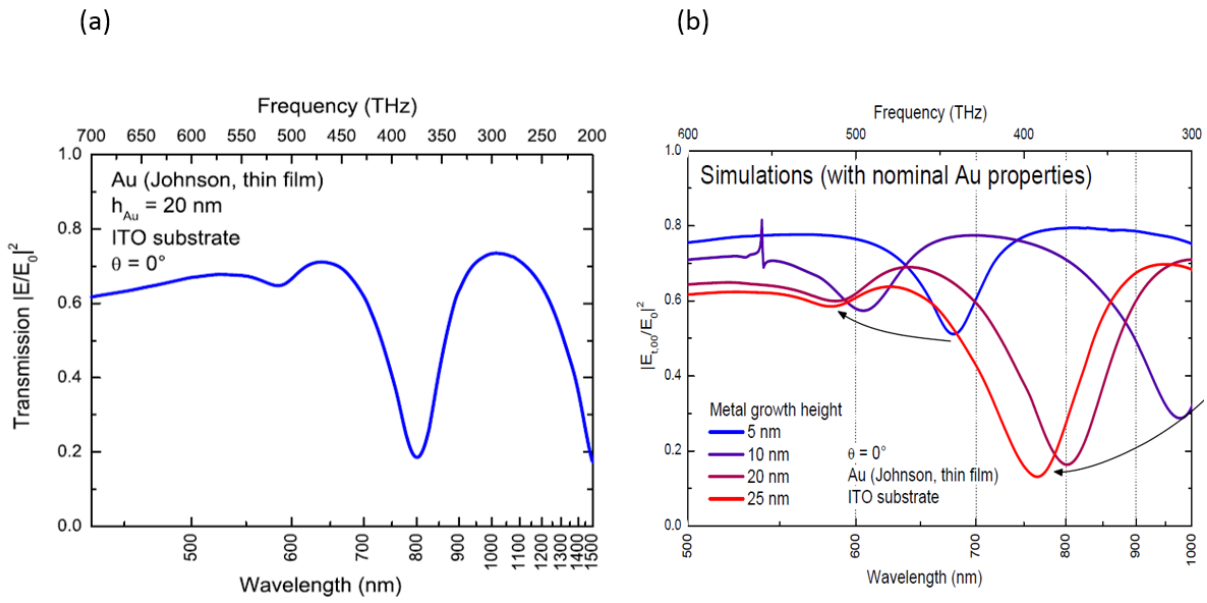

Figure 26: (a) Theoretical absorption curve of an ideal (rectangular cross-section) bi-ring array at a height of 20 nm when irradiated by a continuous-wave Xe-light source. Absorption peaks can be seen for 600 nm and 800 nm. (Note: The decreasing intensity > 1000 nm is attributed to the Xe-light source.) (b) Absorption curves for several bi-ring heights. A position shift and an intensity difference for varying heights can be observed. Simulations were done by the group of Prof. Roskos at Goethe University Frankfurt.

4.1.1 Alignment of the Gas Injection System

The alignment of the GIS (see also chapter 2.2.3) belongs to the most crucial settings one has to take care of. A local balance between potentially dissociating electrons and the precursor molecules is the central factor during FEBID as discussed in chapter 2.2.4. The position of the GIS affects the deposition behavior considerably, as the local precursor flux and its lateral distribution is mainly responsible for the gas molecule replenishment situation. Described in detail by Fridli et al.[58,59] and Toth et al.[60], the local precursor coverage is principally depending on a large number of parameters like nozzle-to-surface distance, nozzle-to-surface tilt angle and nozzle diameter. During all experiments in this chapter (4.1), the GIS (Me_2-Au(acac)) alignment was kept unchanged to provide highest comparability. The precursor nozzle, having inner and outer diameter of 500 µm and 830 µm, respectively, was positioned 430 µm above the surface, measured in vertical direction from lower nozzle edge to surface. The tilt of the GIS with respect to the sample surface involved 52°. A beam scan rotation was opted to 32° to ensure that the slow scanning axis of the electron beam coincided with the main axis of the GIS as discussed in chapter 2.2.6 and elaborated in detail by Winkler et al.[48].The center of the impinging electron beam did not coincide with the main axis of the GIS due to technical restrictions. The shifted position was chosen under consideration of other GIS systems used the same DBM. The lateral distance between the GIS main axis and the electron beam center was scaled to be 180 µm in the X-direction (fast scanning axis) and 30 µm in the Y-direction (slow scanning axis). An overview of the setup can be found in Figure 27.

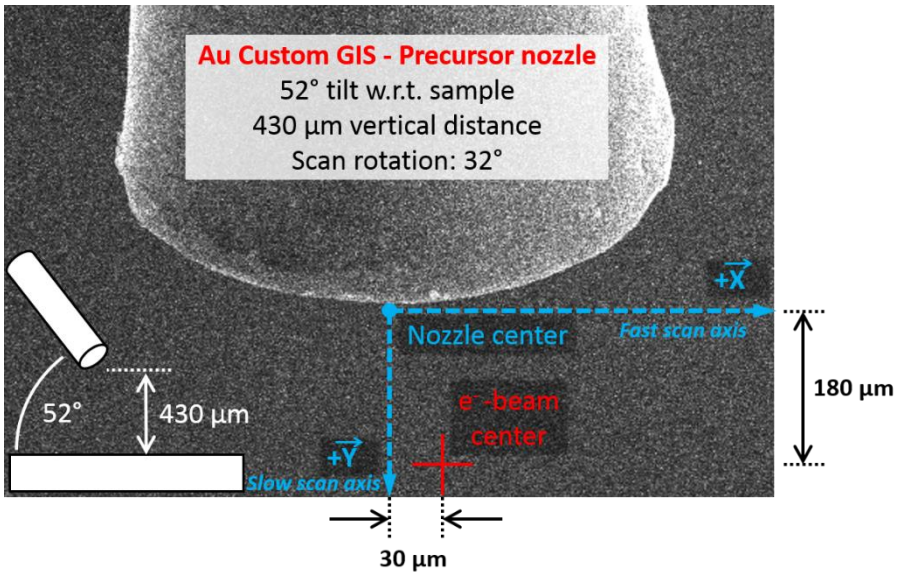

Figure 27: Labelled SEM image of the Au Custom GIS alignment (full image) with a schematic side-view illustration of the setup (bottom left). The GIS main axis did not fully coincide with the electron beam center.

4.1.2 Array Sequencing

With the promising outcome on the downscaling of a single bi-ring (chapter 3.1), the reliable process parameters were inherited. The necessity to work with the highest available electron beam voltage, i.e. 30 kV, and the lowest electron current possible, i.e. 21 pA, for gaining the most precise results had already been spotted by Winkler et al[25,61,62], Schmied et al[41] and Arnold et al[49]. The bi-rings were deposited at 4 nm PoP, 1 ms DT and 20 passes, referring to 5 ms / nm S-TET, combined with an inner to outer clockwise pattern strategy (each beginning at 3 o'clock position, c.f. Figure 30(b)).

The first array, situated inside the cavity, was fabricated by applying a classical interlacing approach[63,64,44], which is graphically illustrated in Figure 28(b). The idea behind is to improve the gas replenishment situation as subsequent patterning is performed far away from previous structures to prevent working in a partly depleted area. In principle, a regular pattern of largely spaced positions is used in the first step and then shifted by a small step to finally achieve closely packed structures. In this case, the 12×12 array was separated into nine individual 4×4 subarrays. These subarrays were generated by implementing an interlaced strategy, going line by line from left to right (fast electron beam scan axis) and from top to bottom (slow electron beam scan axis). The bi-rings within each array were deposited consecutively following the identical patterning procedure, likewise from left to right and from top to bottom.

Figure 28(a) shows the full array attained by applying this standard procedure by a SEM top view image. As evident, an inhomogeneity concerning the spatial height and thickness distribution of the individual bi-rings became apparent. AFM measurements showed the bi-ring heights varying from 10 nm to 15 nm, depending on the depositing order. This opened up a major challenge on realizing structures of tens of nanometers, as with even the best known process parameter and patterning strategies at that time, it seems that ELR conditions (see also chapter 2.2.4) cannot be established. The reason for the arising height / thickness variation is attributed to two effects: ***1)*** proximal depletion and

2) morphological shadowing. The former occurs when the amount of electrons is considerably depleting the local density of precursor molecules. This decrease of local coverage density trivially reduces the growth rate on the one hand, and non-trivially leads to a broadening of deposited structures on the other hand. In more detail, molecule supply from outside is still high while central line areas get increasingly depleted. In other words, when depletion is increasing the beam tails (large radius) dissociates more molecules than the beam center (small scale) which leads to the mentioned line broadening[41]. This explains the broad ring line widths in Figure 28(a) which obviously requires an improved precursor replenishment as discussed later. The second effect involved in the here observed height variation is initiated by the growing deposits, which represents an additional morphological barrier, further complicating precursor diffusion across those structures. Having a close look on the SEM image in Figure 28(a) together with the sequencing in (b) it becomes obvious that the horizontal lines starting with pattern #1, #4 and #7 are first entirely closed before the row below gets started (e.g. 37, …). That means after finishing the first three horizontal lines, there are 3 barriers which hinders the surface diffusion from upper areas, reducing effective replenishment from 3 instead of 4 surrounding directions. The situation gets even worse as the first run used a top down sequence of finished lines (away from the gas flux vector). These circumstances explain the reduced bi-ring height for subsequent rows on the hand and also the increasing line widths on the other hand based on the above described proximal depletion.

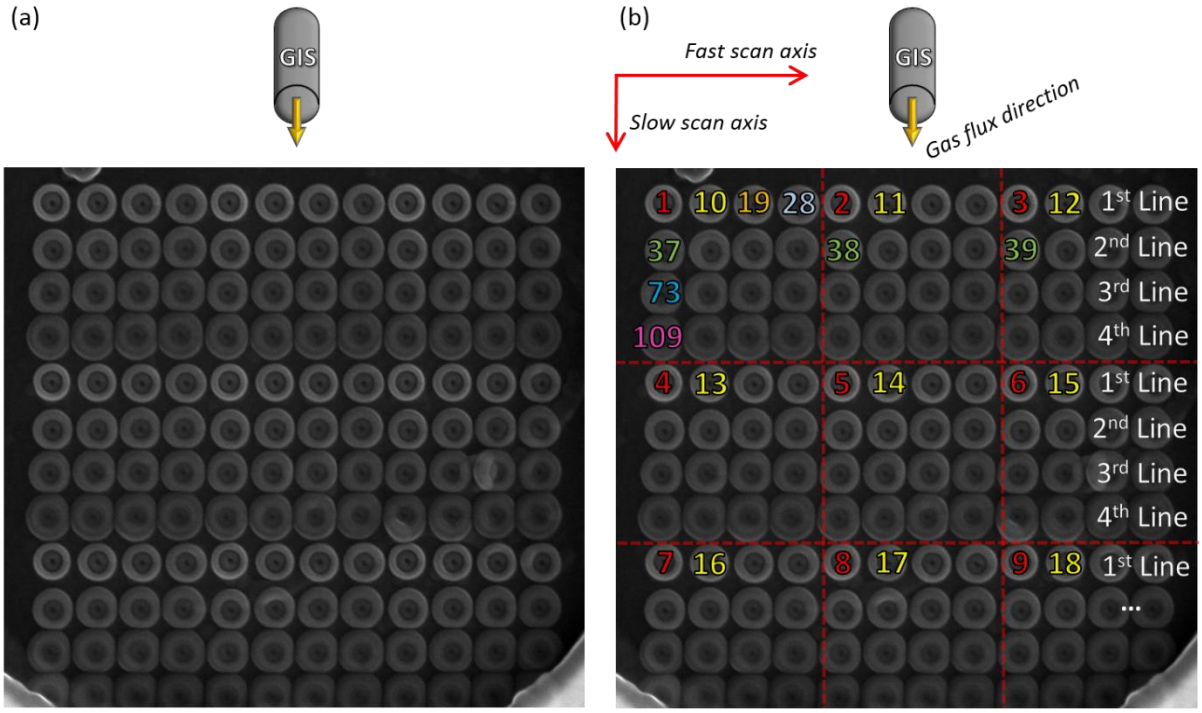

Figure 28: (a) SEM image of a 12 x 12 bi-ring array done by a classical interlacing approach following a line by line array sequencing. This resulted in varying bi-ring heights. (b) Same array with labeling of the applied sequencing. Note: The bright sites in the lower corners are parts of the cavity mask edge. Having two corner bi-rings set on the Au mask happened inadvertently but had no impact on the depositing behavior.

Hence, to obtain homogeneously distributed bi-rings, the classical patterning and even straight-forward interlacing does not work. Therefore, the array sequencing was systematically adapted to prevent a downturn in gas replenishment (see Figure 29). Two decisive details were changed: **1)** The patterning towards the GIS and **2)** a large and non-regular spacing between sequential numbered bi-rings were implemented to prevent the formation of closed bi-ring rows. Aligning the patterning direction towards the GIS avoided undesirable gas shadowing effects by preventing the formation of morphological barriers. The large spacing between consecutively fabricated structures minimized the proximal precursor depletion due to the adding of time for gas replenishment. Having a non-regular arranged pattering sequence bypassed the arrangement of closed barriers. This carefully implemented sequence optimization led to much more homogeneous ring structures at different positions when comparing Figure 28(a) and Figure 29(a). Complementary AFM measurements not only confirm this height homogeneity (averagely 11 nm) but also revealed homogeneous line widths at the base around 40 nm. By that, the lateral inhomogeneity concerning heights and line widths induced by evolving morphological barriers and the entailed proximal depletion, respectively, could successfully be removed. While the “macroscopic” inhomogeneities are removed, there is still a need to evaluate the bi-ring quality on small scale as discussed in the next chapter.

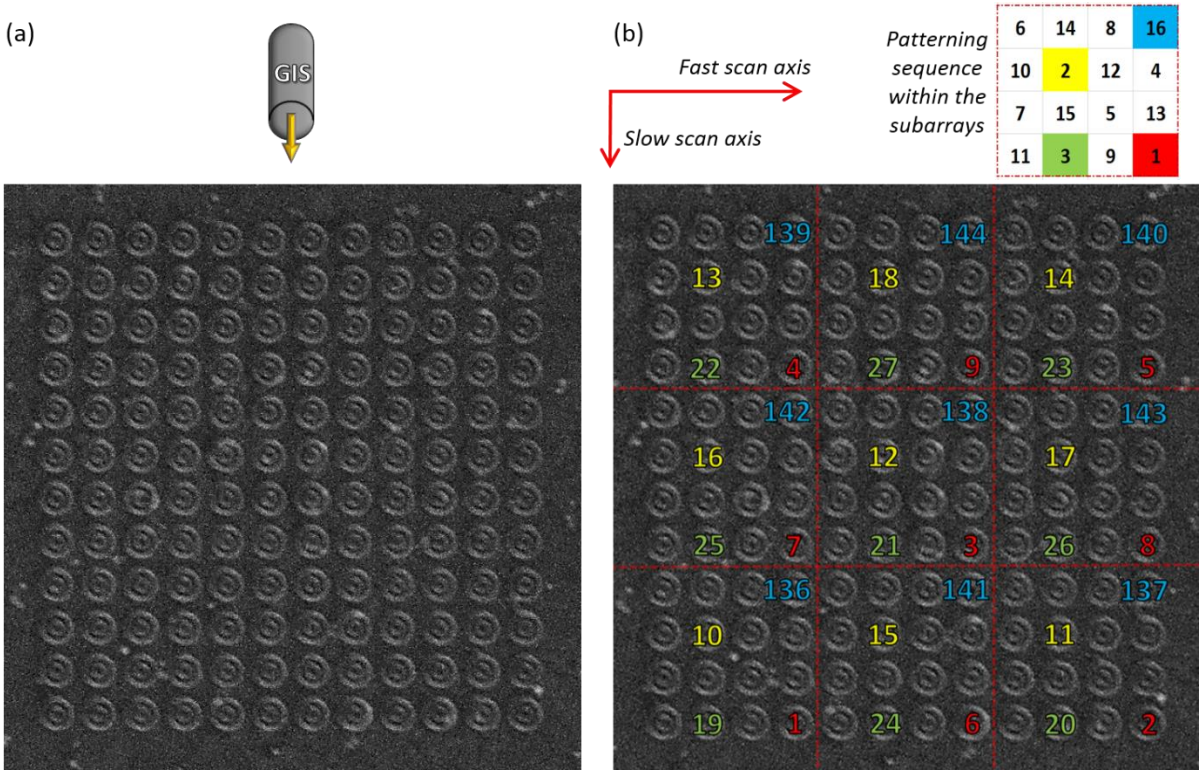

Figure 29: (a) SEM image of the 12 x 12 bi-ring array with an optimized array sequence which prevents the formation of morphological barriers which influences surface diffusion. (b) Same array with labeling of the applied sequencing.

4.1.3 On-Ring Fine-Tuning

While the array sequence optimization had been successfully conducted by finding an arrangement that provided a homogeneously distributed array, a closer look on individual bi-rings revealed spatially varying on-ring volume growth rates, which can be obviously seen on the AFM height image in Figure 30(a). Noticeable in Figure 30(a) is the characteristic first-shot effect on the inner ring at 3 o'clock position (bright spot) that appeared on nearly all bi-rings. The structures developed higher on the area where the electron beam impinged the surface at first, when the precursor molecule density is at its highest. Structure parts that were made afterwards suffer a lack of precursor molecules and could not grow to an equal level. This indicates again, that ELR conditions were not fully established. The option was chosen to empirically compensate the growth inconsistency by using an on-ring DT adaption, whose concept is indicated in Figure 30(b). As most of the bi-rings revealed a similar shape, the AFM height information as input parameter was used. Next, the DT was decreased for those patterning pixels which revealed higher growth rates. Even tough being quite imprecise, the performed adaption resulted in laterally homogeneous bi-ring altitudes and cross sections (for related, quantified data see chapter 4.1.4).

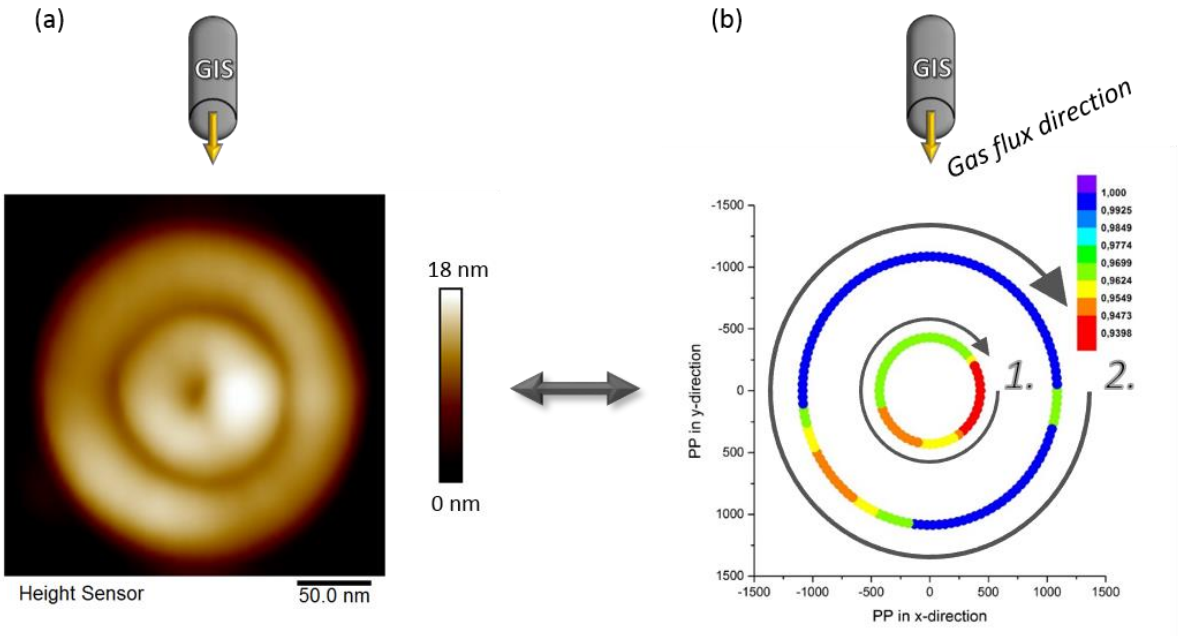

Figure 30: (a) AFM height image of a typical bi-ring within the array revealing the on-ring deposition was not homogeneous but reveal radius dependent height variations (brighter areas). (b) Schematic description of the on-ring patterning sequence and the DT adaption based on average AFM height data. In more detail, the DT was decreased for points that grew faster, which in particular pertained to the initially irradiated area (inner ring at 3 o'clock position). The different colors represent the various scaling factor following the legend.

Based on the both improvements, the on-ring fine tuning (DT adaption) and bi-ring sequence optimization (4.1.2), further arrays have been fabricated. They were again produced directly within the 300 nm deep 5 × 5 µm cavity composed of gold on the Ito substrate. Detailed analyses confirmed homogeneous on-ring line heights and acceptable line widths in the range of about 35 nm FWHM

across the entire array. However, as evident in Figure 31(a), AFM height images revealed a systematic height variation by means of a cross-shaped distribution (brighter areas) which indicates an inhomogeneous gas distribution inside the cavity. In numbers, heights between 8 nm and 13 nm were found as summarized in Figure 31(b) by a colored 3D surface plot which clearly shows the cross-shaped feature together with the gas flux direction. As such features on plane Si surfaces were not observed, this effect can be attributed to the cavity itself. In more detail, the here assumed edge reflection effects of adsorbing and desorbing molecules leading to a small but evident position dependent precursor gradients (corners and edges). At this point it was decided not to study the exact origins of this behavior but proceed with purification experiment to evaluate whether the structures generally exhibit a plasmonic response. The deeper reason for this decision was the awareness that a lot of trial-and-error adaption already has been done instead of gaining a deep knowledge of the underlying processes. At that point it became already evident that it will be necessary to stop with bi-ring fabrication, step back a little and study the fundamental principles of *controlled* high-resolution fabrication.

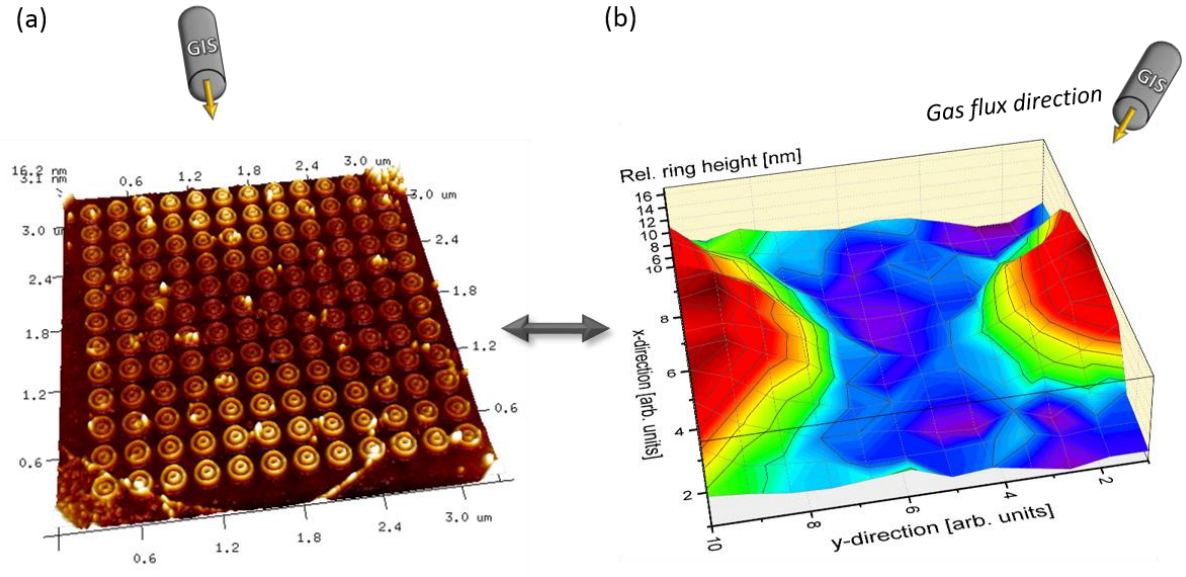

Figure 31: (a) An AFM height image of the array shows varying growth rate inside the cavity. The average bi-ring height was determined to be 11 nm with variations of 5 nm. (b) Identified bi-ring altitude in dependency of the position inside the cavity. The deposit height is assumed to give conclusions on the precursor gas distribution inside the cavity.

4.1.4 Array Purification

For the next move on the way towards creating plasmonic MTMs a purification process was conducted, necessary for generating pure gold structures. The purification of the array was performed using 5 keV, 5 nA, 4 nm PoP, 1 µs DT, 60 C / cm², 10 Pa H_2O on a purification field with size of 4×4 µm². This parameter setting is equivalent to that used in the previous work (see chapters 2.3 and 3.1), originally introduced by Geier et al. in this institution[51]. During the purification process the bi-rings kept their closed shape without breaking or any considerable lateral shrinking. The bi-ring height dropped by about 65 % giving 2 - 4 nm high Au MTMs with line widths of roughly 35 nm (FWHM) on average. Figure

32 shows 3D AFM height images before (a) and after full purification (b) of the same bi-ring array. As already mentioned in the chapter 3.1, the ITO undergoes massive buckling during purification (see Figure 32(b)), which was attributed to a delamination of the 150 nm thick ITO layer. In numbers height variations up to 125 nm after purification were found. As a side note, new ITO substrates to eliminate this problem for further studies are currently screened.

When investigating the morphology of individual purified bi-rings, their geometry did not feature a completely satisfying result. The bi-rings, as representatively shown in Figure 33, revealed a small on-ring height variation of 1 nm together with total heights of 3 - 4 nm for this specific ring. Here it is important to note, that based on the cross-shaped height distribution (see previous chapter) a total height range of 3 - 7 nm was covered for the full array which stays within the targeted minimum of 5 nm compared to the simulation calculating the plasmonic response. More strikingly, however, are the line widths of 35 nm (FWHM) / 50 nm (base line width), which indeed is clearly broader than the targeted width of 25 nm (base width). Also, the cross section is Gaussian shaped as expected rather than giving a rectangular ("sharp") profile. The measurement of the bi-ring profiles (indicated by the red dotted arrow in Figure 33) was done by averaging the cross section over an area of roughly 5 nm to avoid fluctuations. In summary, the results so far are twofold. From a FEBID point of view, the fabricated bi-rings are a very good result as still compact pure gold structures in the sub-50 / sub-5 nm regime (base widths and heights, respectively) were successfully produced. At the moment of this achievement, this result represented a worldwide benchmark in the respective community. From a plasmonic point of view though, the results are not ideal, as there is neither a rectangular cross section nor the narrow dimension initially targeted. Nevertheless, the plasmonic response was studied as described in the following chapter.

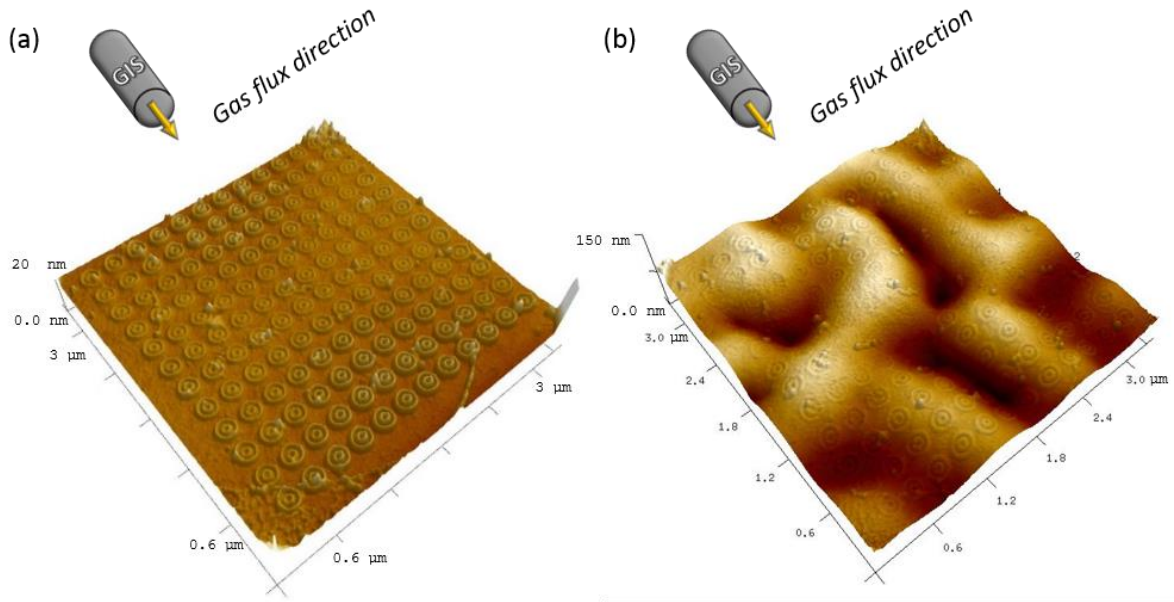

Figure 32: (a) AFM height image of the array before purification. (b) AFM height image of the array after purification. The wavy structure of the ITO layer due to the purification process is one of the major issues. The fully purified Au bi-rings are still recognizable.

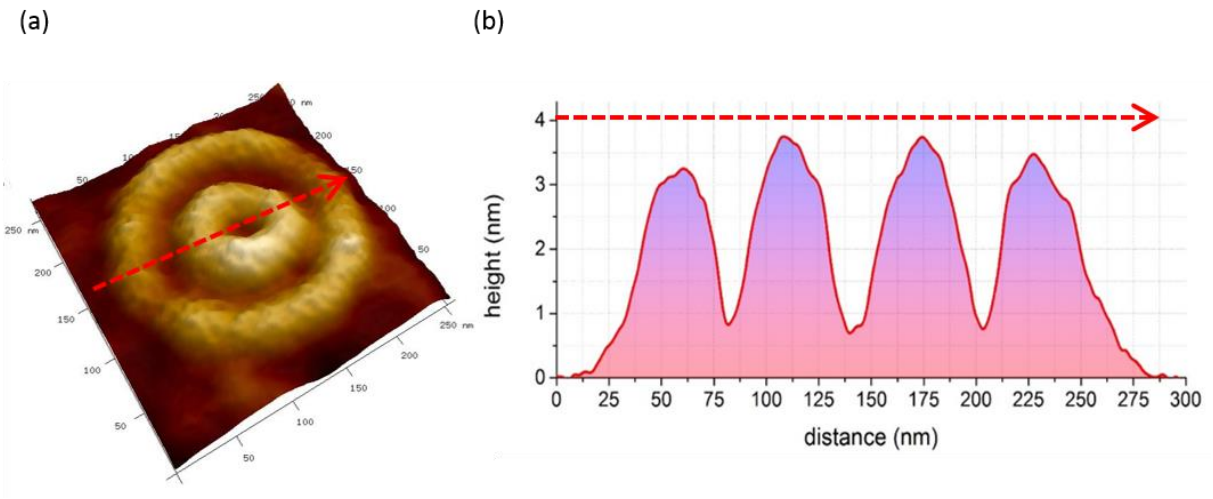

Figure 33: (a) AFM image of a purified bi-ring, found on the array in Figure 32(b). (b) The cross section of the bi-ring was unveiling the structures being too broad for the given height and having a non-rectangular profile, compared to the geometry used in the simulation.

4.1.5 Optical Response

To evaluate the optical response of the plasmonic bi-ring systems, different samples have been subjected to plasmonic measurements at the workgroup around Prof. Roskos at the Goethe University Frankfurt. Specifically, as-deposited and fully purified bi-ring arrays were provided to compare the different material qualities and its optical behavior. More details on the measurements can be found in chapter 2.5. The results are summarized in Figure 34 by comparing three unpurified arrays (A, B, C) together with spectra from fully purified bi-ring arrays shown in blue. The orange curve projects the initial simulation according to an array with alternating bi-ring heights of 5 nm and 10 nm following the experimentally derived height distribution of 3 - 7 nm for the full array (see previous chapter). Within the wavelength range going from 550 nm to 850 nm, a noticeable decrease in transmission for all arrays (B, C, D and E) can clearly be recognized. It was not expected for the as-prepared structures to generate any plasmonic response, as the high content of carbon (>90 at.%[8]) in the deposit matrix was assumed to completely hamper collective free electron oscillations. Compared to the as-deposited arrays, the purified one revealed an overall increased performance. All arrays displayed a significantly broader absorption curve (i.e. 550 - 850 nm) relatively to the simulation (610 nm and 680 nm), which most likely could be referred to the challenges in fabrication. Summarized, there were several reasons for the observed broadening of the absorption peaks in the transmission curve that originated from the depositing and purification of the bi-ring structures:

1. Inhomogeneous heights. As discussed in chapter 4.1.3, the cavity induces a lateral coverage gradient which entails a height variation. This ultimately means that there is not a distinct but a distribution of bi-ring heights leading to a superposition of discrete plasmonic response.
2. Too broad line widths. Instead of achieving line width of 25 nm, the bi-rings were found being distinctively broader, giving 35 nm (FWHM) / 50 nm (base line width). This indicates non-ideal working regime conditions initiated by either low precursor coverage and / or replenishment. The Me_2-Au(acac) precursor appeared in this regard as particularly inefficient compared to

other precursors, e.g. Pt ($MeCpPt^{IV}Me_3$), mainly because of the short residence times on the surfaces.

3. Non-rectangular cross sectional profile. All characterized FEBID structures revealed a Gaussian like profile. This is unfortunately an inherent limitation of FEBID as for the ELR or close-to-ELR conditions the deposit cross-section mimics the beam profile which is Gaussian like. Please note, an on-purpose shift towards molecule limited regime conditions is known to provide flat top profiles as targeted here. However, this goes along with massive line broadening where the aimed 25 nm are not possible. Therefore, this profile issue will remain even if the structures goes below 20 nm line base width.

Finally, it should be emphasized that the ITO buckling is not listed above, because all arrays, purified and non-purified, showed a similar broadening in their absorption curve while ITO buckling is only evident for the fully purified array. This allows the conclusion that this morphological disruption may have only little influence on the plasmonic response of the MTM.

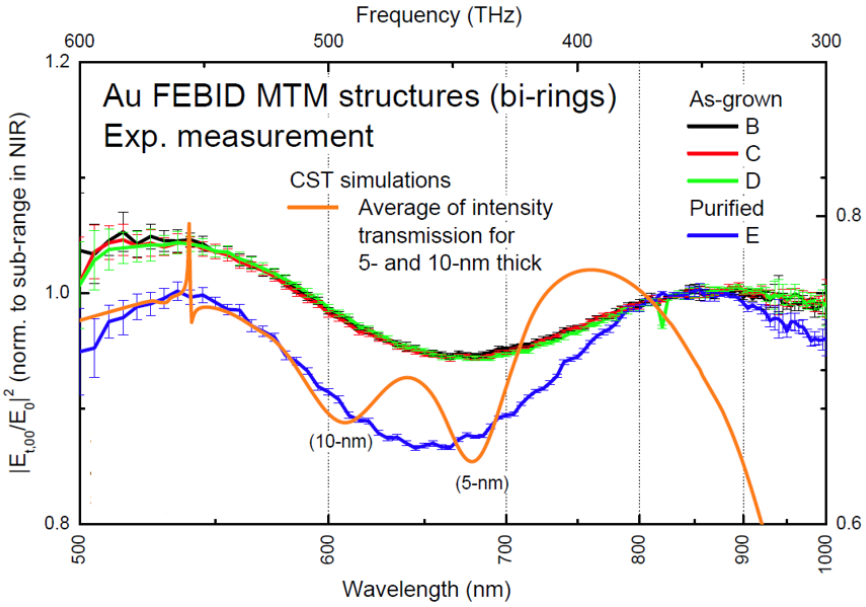

Figure 34: Transmission curve of three unpurified (B, C and D) and one purified (E) bi-ring array in comparison to the initial simulation (orange curve). Not only the purified, but also the unpurified structures exhibit plasmonic resonances, whereby the purified ones do more distinctively. The arrays display broader absorption spectra (550 - 850 nm) than the simulation suggests. The measurements were done by Prof. Roskos at the Goethe University Frankfurt.

In summary, it can conclusively be stated that the proof of principle had been delivered that FEBID can be used for the on-demand, additive, direct-write fabrication of plasmonic nanostructures for application in the THz range. This becomes evident by the orange curve in Figure 34, showing a response in well agreement with real measurements around 655 nm.

However, all deviations from ideal spectra evident in this figure seem to originate in the initial FEBID fabrication concerning ***1)*** too broad line widths and ***2)*** a Gaussian like cross-sectional profile. While the

latter is unavoidable in FEBID, the former aspect can be improved by a deep understanding of influencing and limiting effects during nano-synthesis. The crucial point in this context is the working regime, which has to be in real ELR conditions for a predictable fabrication close to the intrinsic limitation of FEBID given by the electron beam profile and backscattered electrons as revealed by Arnold et al.[49]. Therefore, further efforts in producing plasmonic nanostructures were stopped at this point and it was decided to step back and study the fundamental FEBID processes in the high-resolution regime. The goal was to build up a systematic knowledge for predictable fabrication close to the ultimate resolution limit. Consequently, the following chapters are addressing fundamental growth dynamics with the aim to establish real electron limited conditions.

4.2 L-shaped Structures

For obtaining improved capabilities on precisely fabricated nanostructures, the desire was henceforth to understand the depositing behavior, to optimize the fabrication parameters and to enhance the precursor gas situation. The overall main task was to elaborate a protocol that enables the deposition within the RRL regime, which has been assumed to be the requirement for obtaining the thinnest possible deposit profiles[48] (see also chapter 2.2.4). A specific pattern design was chosen, on which the line profiles could be reliably measured and from that the prevalent regime be classified. For this purpose, a design of seven nested "L"-shaped lines was opted as shown in Figure 35. Each "L" consisted of a horizontally and a vertically aligned branch, with branch lengths from 600 nm (longest "L") to 80 nm (shortest "L"). This specific geometry choice has also been used in experiments conducted by Van Oven et al.[65] in 2011, issuing on resolution improvements of FEBID as well (using $MeCpPt^{IV}Me_3$ as precursor). Van Oven at al. were able to produce lines with widths in the sub-10 nm range by depositing on Si wafers that were only 200 µm thick. Although an impressive resolution was achieved, a critical look on this work was needed, as the authors exclusively showed SEM images and did not provide quantitative height data. Therefore, it has been unclear whether the specified line widths stemmed from a morphology or were based by internal Pt agglomeration which gave the SEM contrast. To answer this question, this work used mainly AFM and complement the data by SEM when needed. Regarding the design, the multiple "L" pattern has its advantage in the simple discriminability between the dominating working regimens by basically comparing the line profiles. Having one horizontal and one vertical line provided redundancy in fabrication and measuring on the one hand, and on the other is ensured that the AFM measurements were more reliable. At this point it is important to mention that AFM working principles could lead to slightly anisotropic results caused by tip-convolution. In more detail, the cross-sectional profiles are prone to be antisymmetric and / or reveal broader structures than they actually are due to imperfect tip shapes and finite side slopes, respectively (see chapter 2.4). Keeping these risks in mind, three line types were in focus during the nano-characterization, according to Figure 35: **1)** The protruding line section of the centered "L", hereinafter referred to as "**single line**". The precursor gas on this line type is replenishing laterally from two sides and directly from top down (see black arrows). **2)** The "L" on the very bottom, hereinafter referred to as "**outer line**". On this line type, the precursor gas is replenishing laterally, mainly from one side (blue arrows), resulting in lower replenishment rates compared to the single line. **3)** The two lines situated between the single line and the outer line, hereinafter referred to as "**inner lines**". These lines were expected to have the lowest gas replenishment rate, as the precursor molecules refill from top down in undisturbed ways (red arrows), with minor lateral contributions where the molecules have to diffuse

across other lines before. The estimation of the working regime was based on the distinction of the line type profiles (a multiple pass pattern strategy assumed): If depositing proceeds within the MTL regime, the growth rate will primarily depend on the replenishment rate (and the individual pattern design). Therefore, the single line will evolve faster and consequently yield higher volumes than outer and inner lines do (especially in terms of height). Subsequently, the inner lines will yield the lowest volume. However, if fabrication is somehow achieved in the RRL regime, all lines will feature homogeneous and similar developed profiles in terms of height and width.

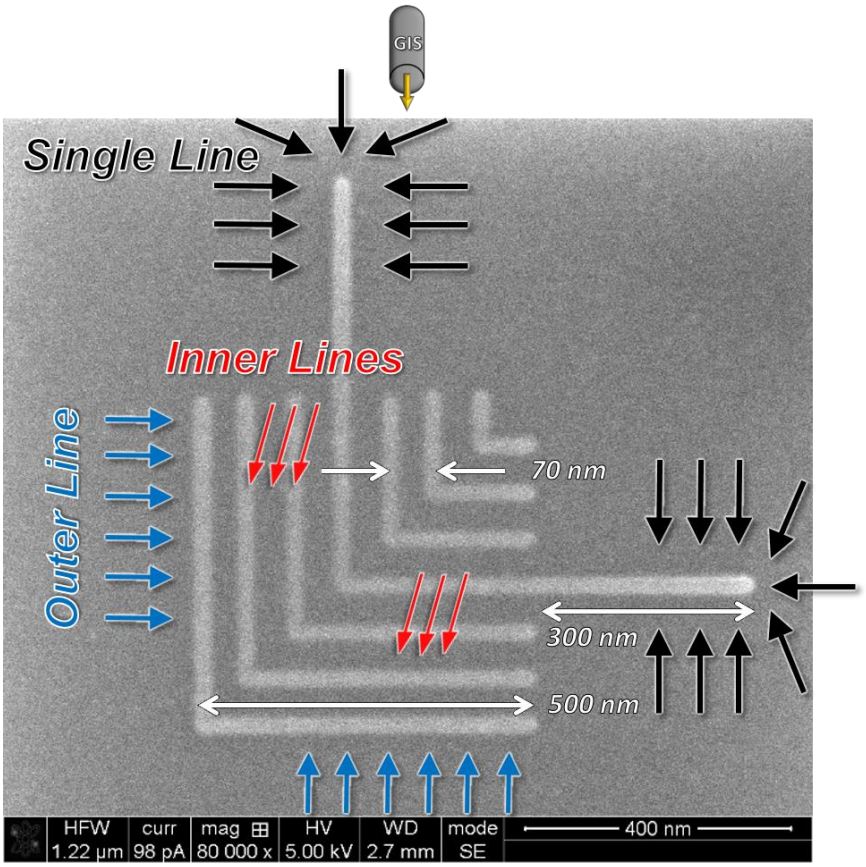

Figure 35: SEM image of the used a pattern design by means of seven, closely spaced "L" lines, together with annotations of the line lengths and respective line-to-line center distances. The colored arrows show the precursor gas diffusion in dependence of the particular line site. There are three important types of lines to focus on: The single line (black) with gas replenishment coming from two lateral directions and from top down directly, the outer line (blue) with gas replenishment coming from one lateral direction and from top down, and the inner lines (red) with gas replenishment coming from top down only. Note, for the two latter lines, there is an additional replenishment path across surrounding lines, which, however, is known to be more complicated due to different adsorption / diffusion behavior.

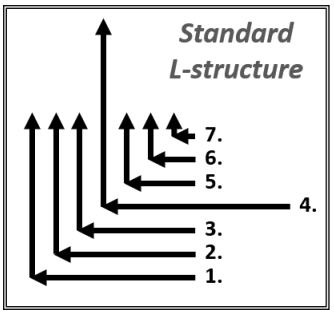

Figure 36: Sketch of the patterning direction and sequence. The electron beam begins its movement at the bottommost "L"-line (1.) and ends at the topmost (7.), which is also the shortest. The underlying reason was an on-purpose patterning towards the GIS to minimize nano-shadowing effects, as discussed in chapter 4.1.

In the following sections, multiple "L" patterns (hereinafter referred as to "L-structure(s)") were deposited by applying the Pt precursor (chapter 4.2.2), being a guideline for subsequent experiments when using the Au precursor. Figure 36 shows the detailed patterning sequence of the fabricated L-structure. The deposition starts with the bottommost L (1.) and ends with the topmost (7.). This approach was decided, as a patterning direction towards the GIS was considered minimizing the gas shadowing effect, which was spotted on the bi-ring fabrication (chapter 4.1). First analysis on the Pt precursor generally concentrated on the height / width control when varying depositing parameters (specifically, i.e. the S-TET, see also chapter 4.2.2.1)). When an appropriate parameter window was found, where the structures revealed the aimed dimensions, e.g. a line height of 10 - 20 nm and width of less than 25 nm (see 4.1), a parameter optimization was performed (chapter 4.2.2.2) to achieve the best performance possible. The optimization was realized by varying the DT and the number of passes (keeping the S-TET constant). Same procedure was done using the Au precursor (chapter 4.2.3) in the second part. One detail to be mentioned has been an observation by Van Oven et al.[65]. They found a technical issue with the microscopes power supply, which required a synchronization in the patterning approach. To check the influence in this setup as well, experiments were conducted in which the pattern sequencing synchronized to the 50 Hz electrical grid frequency (see 4.2.4). Although extremely small Au structures could adequately be realized when optimizing the parameter setting, a full RRL regime could not be established. Therefore, as last step, experiments were performed that focused on the fabrication of L-structures with additionally implemented replenishment time (chapter 4.2.5). This strategy succeeded and a RRL regime finally could be attained. Analogue to the fabrication of the bi-rings (see 4.1), all L-structures were deposited under similar framework configurations. These include 30 keV, 21 pA, 9 nm PoP (increasing the PoP from 4 nm (bi-rings) to 9 nm was supposed to enhance the depositing accuracy) and an S-TET ranging from 555 µs / nm to roughly 10 ms / nm. For simplicity, quantitative S-TET values will hereinafter be replaced by the DT and the number of passes. Since all L-structures were deposited using a PoP of 9 nm, the term S-TET will subsequently be replaced by the TET. All deposits were fabricated on a Si substrate wafer with size of 10×10 mm. All L-structures had the GIS needle positioned upside and directed towards the vertical single line (cf. Figure 35).

4.2.1 Precise Measurement of Exceedingly Small Structures

When fabricating extremely small structures, not only the fabrication itself is challenging, also the accurate determination of their genuine size highly is. For this reason, the height and width of the structure lines were measured in a two-step process. After fabrication in the DBM, the deposits were measured via AFM first, followed by a subsequent characterization via high-resolution SEM imaging. This approach was chosen to prevent any potential carbon contamination due to imperfect vacuum conditions in the DBM vacuum chamber, which possibly could corrupt any subsequent AFM measurements. The issue of carbon contamination appearing from residual gas when imaging samples via SEM had already been known by Plank et al.[40] (also referred to as "structural broadening"). Another important aspect emerges by comparing SEM and AFM height images of the identical Pt L-structure in Figure 37: The two images *allegedly* do not depict the same L-structure (deposited with DT 100 µs and 200 passes). In fact they do, which reveals a huge drawback in the AFM measurement principles at this scale: If not extremely well adjusted, the geometrical extent of the AFM cantilever tip together with the finite side wall angle distort lateral measurements, leading to images with structure widths that are compounded by a superposition of tip size and real line width. This problem increases with higher / thinner structures (referred to as "tip convolution", see AFM principles in 2.4). Thus, for data analysis, the values of line widths were deduced from SEM images (base width). The deviation of the base width / the width measuring error was assessed to be ≈ 5 nm. However, AFM investigations provide a very accurate determination of structural heights (deviation of height / measuring error ≈ 1 nm), which is not possible via SEM at this precision. Additionally, for certain L-structures it was even possible to get AFM images that enable an accurate width (FWHM) determination (which is explicitly mentioned in the further text).

(a) (b)

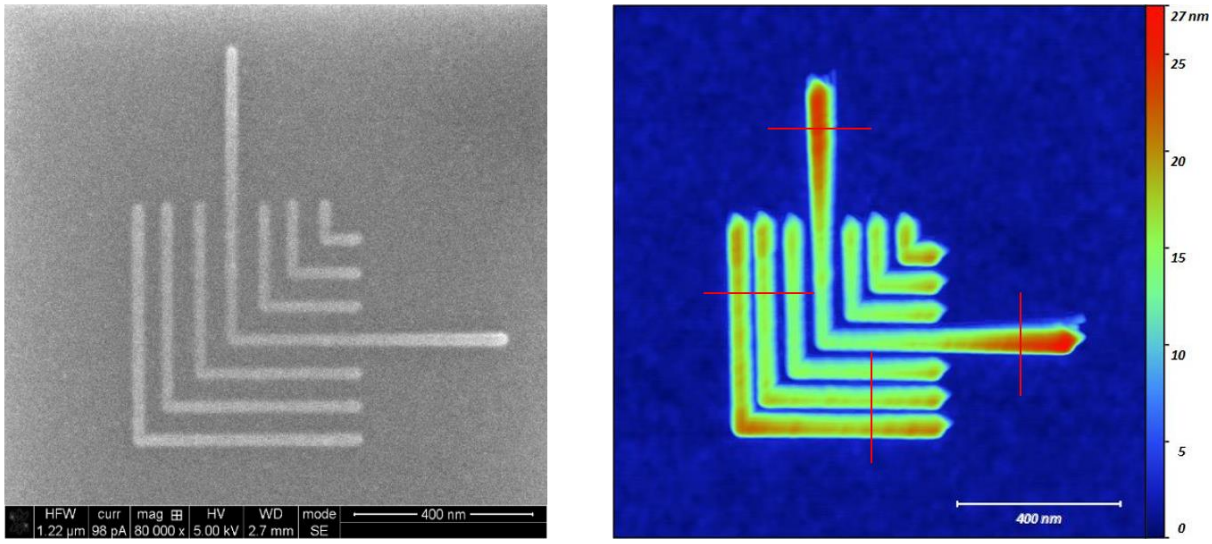

Figure 37: SEM (a) and AFM (b) image of an identical Pt L-structure. The AFM measurement mostly do not render the real lateral dimensions when measuring very thin structures due to tip convolution. Therefore, line widths were mainly deduced from SEM images. Image (b) also shows the measurement lines (red) on the positions the profiles (line heights) actually were determined. The L-structure was deposited with 200 passes and DT 100 µs.

Four horizontally and four vertically aligned branches were analyzed (i.e. number 1., 2., 3. and 4. in Figure 36), whereby each profile was measured in the second quarter area, viewed from the outside line starting point. Viewing the red measuring lines that are visible in Figure 37(b) supports to comprehend the manner of profile determination. The line cross section was averaged over an area of approximately 4 nm perpendicular to the cross-sectional line to minimize statistical fluctuations. The inner line data (both horizontal and vertical) always were averaged over line number 2. and 3. (cf. Figure 36).

The SEM images for measuring the line widths was conducted using the immersion mode (UHR mode) with 5 keV, 98 pA and a DT of 10 µs at a resolution of 1024 × 886 pixel. Once the samples had been transferred into the SEM vacuum chamber, an additional waiting time of > 1 h between loading and imaging was implemented. This was done for gaining an acceptable vacuum condition, and consequently, to minimize the unwanted structural broadening by carbon contamination. The distance between electron beam column and sample surface was set to 2.7 mm to enable true high-resolution imaging.

4.2.2 Pt Precursor

The Pt precursor ($MeCpPt^{IV}Me_3$) has been commonly used in this working group. Therefore, it was plausible not just exploring the resolutions limits using the Au precursor, but doing similar using the Pt one as well. Moreover, investigations into the growth behavior of the internally far better known Pt precursor advantageously gave indications on the Au depositing behavior. Therefore, Pt L-structures were deposited and examined at first. The Pt GIS position did not entirely coincide with the electron beam center due to technical restrictions. The GIS main axis position was found to be shifted 43 µm in X-direction and 530 µm in Y-direction (upper nozzle edge) to the electron beam center (cf. Figure 27). The stage tilt involved 52° and the scan rotation was set to 31.9°. The surface-to-nozzle (lower edge) distance was adjusted to 50 µm, which was distinctly less than compared to the usual distance when doing FEBID (“eucentric height”, see 2.2.3). The smaller nozzle-to-surface distance was expected to raise the precursor gas density and subsequently also the replenishment rates.

4.2.2.1 Pt: General Deposit Growth Dynamics

The first move towards ultra-high resolution fabrication was to narrow the ideal parameter set. For this purpose, several L-structures with varying passes (**TET**) at constant DT were deposited. The DT was set to 100 µs, and the number of passes ranged from 50 to 10.000. A reasonable analysis for passes higher than 1000 was not obtainable, as the structures lines started to overlap for TETs that were set too high. The charts in Figure 38 represent the line heights and widths of several L-structures, each fabricated with different TETs.

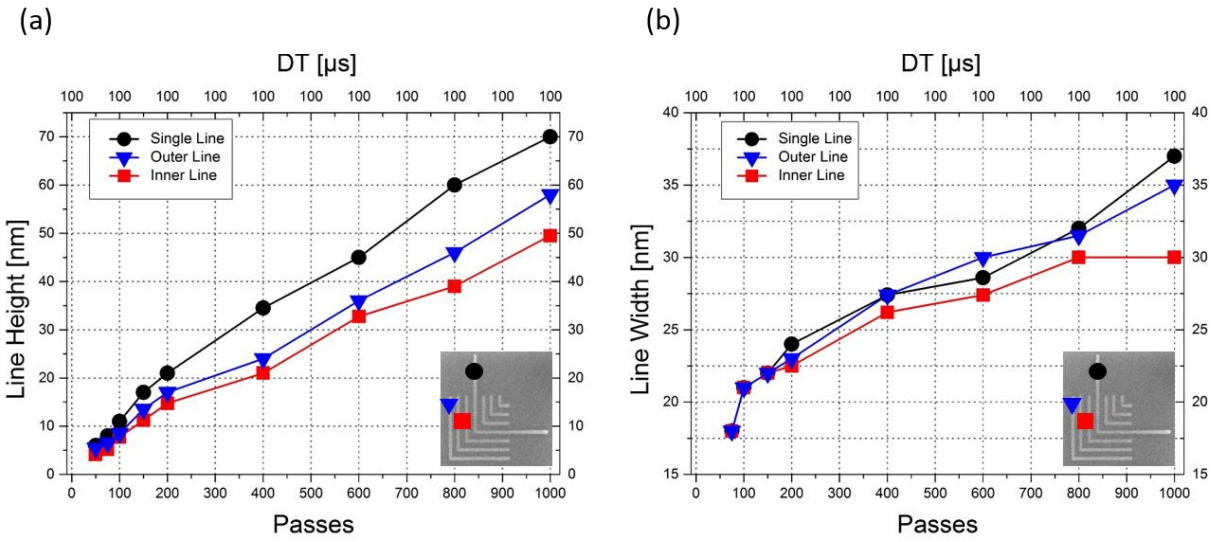

Figure 38: Dependence of line dimensions on TET (passes) for Pt structures. The line heights were measured via AFM and the line widths (base width) were deduced from SEM images. Chart (a) distinctively shows increasing height differences (line splitting) for higher TETs due to the lower gas replenishment rate for outer and, in particular, inner lines. (b) The line width increases with higher TET, whereby for 150 or less passes a distinction was not discernible between single-, inner- and outer line. For high TETs (roughly > 800 passes) the inner lines stop broadening and overlapping starts. Horizontal and vertical lines were averaged.

As expected, the lines were constantly extending their size (height and width) for increasing TET, giving heights of roughly 10 nm for 100 passes to 50 nm (inner line) - 70 nm (single line) for 1000 passes. The diverging height growth rate of single, outer and inner lines (see Figure 38(a)) is of special interest and can distinctively be observed on structures deposited with passes of 200 and more. The progressing difference for higher TETs undeniable indicates that at least the inner / outer lines were deposited in the MTL regime due to the limited replenishment paths via surface diffusion. The effect significantly weakens for passes fewer than 200 due to the low TET and the small amount of required precursor molecules. A similar behavior could be observed on the line widths (see Figure 38(b)), ranging from 18 nm for 75 passes to 30 nm (inner line) - 37 nm (single line) for 1000 passes. A width determination on the L-structure that was deposited with 50 passes could not be satisfyingly preformed via SEM due to the extremely small line dimensions together with the nature of thin lines, where electron contrast strongly decays. For structures fabricated with TETs equal or lower than 150 passes a width distinction between single, outer or inner lines could was not possible. This is, as intended, an indication for shifting into an RRL regime for low TET. The distinctive kink in the curve found around 100 passes could possibly be explained by a basically higher growth rate when depositing at lower TET (perhaps RRL regime). However, for passes higher than 150 the single, outer and inner lines start diverging in width, leaving the inner lines being the smallest and the single lines the broadest ones. The inner lines (red) broaden continuously until reaching a TET of about 800 passes, before overlapping kicks in and the L-structure starts to become one solid pad (with two protruding arms remaining).

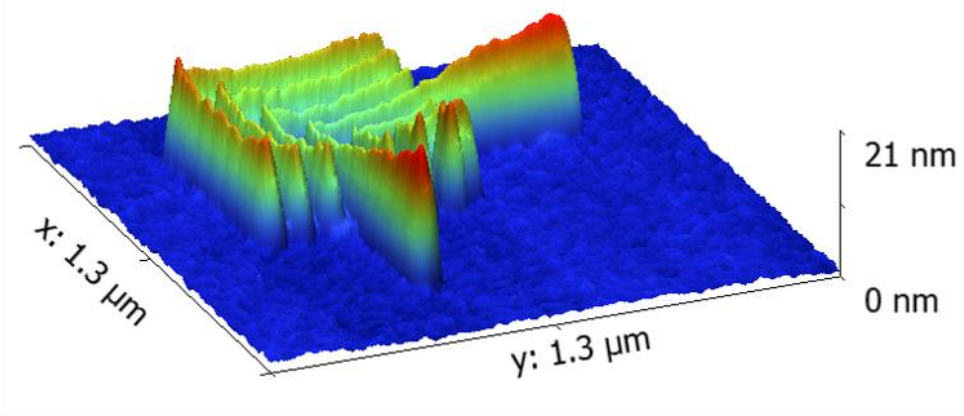

Figure 39: 3D AFM height image of a Pt based L-Structure, deposited with 1000 passes and DT 100 µs. Noticeable are the non-homogeneously distributed lines and the distinct structural bowl shape resulted from an imbalanced gas replenishment rate leading to spatial coverage gradients. The protruding branches (single lines) benefit from the higher amount of precursor molecules during deposition and therefore grow taller and broader than the other lines. Evidently, an RRL regime was not prevalent during deposition.

Figure 39 (1000 passes, DT 100 µs) shows a distinctive structural bowl shape that generically occurs for solid structures[48] when depositing in the MTL regime while having the DT set too low (at multiple pass patterns strategy). The image features the inner lines underdeveloped (thinner), compared to outer and single line, as the precursor molecules can't diffuse into the structure center timely within one electron beam cycle (pass). Therefore, ambient replenishing gas that is diffusing towards the inside area is largely absorbed by the bypassing electron beam before it can reach the inner structure.

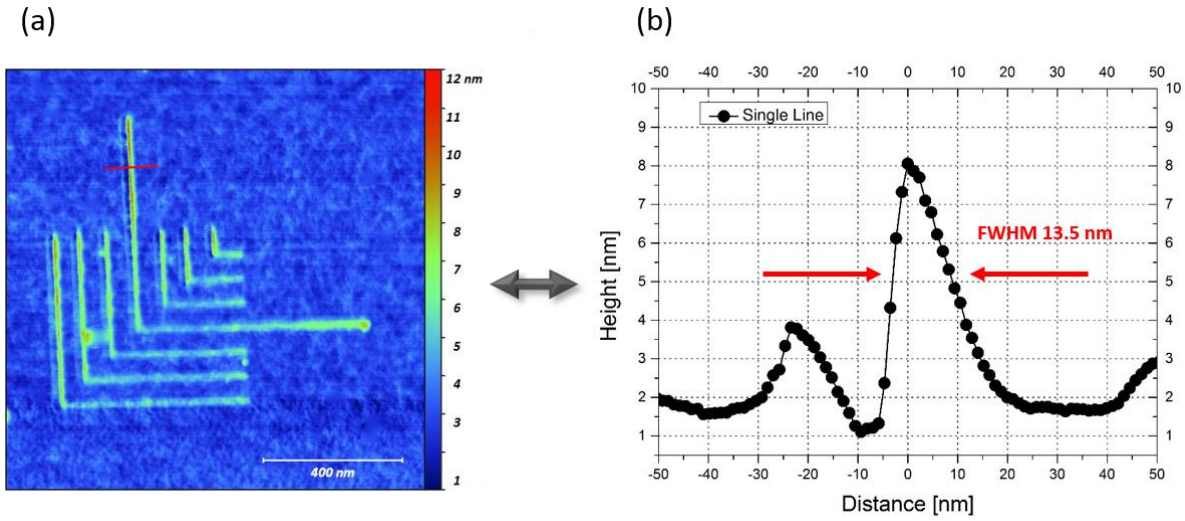

Figure 40: (a) 3D AFM height image of a Pt L-Structure (deposited with 50 passes and DT 100 µs) that allowed an appropriate width determination of the vertical single line (red line). (b) A FWHM of 13.5 nm at a height of ≈7 nm represents a new benchmark in nanostructuring via FEBID. Note: A width determination of the other lines on this structure was not possible due to the emergence of tip convolution (discernible on the faded horizontal lines in (a)).

As mentioned, the SEM analysis of the L-structure fabricated at 50 passes was not possible, but an adequate AFM width determination of the vertical single line providentially was, visible in Figure 40. Measuring its profile revealed a FWHM of 13.5 nm at a height of roughly 7 nm (Figure 40(b)), impressively representing a benchmark in the fabrication of Pt structures via FEBID for such heights. Although the structures grow acceptable homogeneous in height / width when assembled with a TET of equal or less than 100 passes (at DT 100 µs) (cf. Figure 38), the lines remained too thin for these parameters, compared to the intended height of 10 - 20 nm at width of 25 nm. To attain superior results, it was decided to put the focus on a parameter optimization using a constant TET of 10 ms while sweeping the passes and the pulse durations to find the ideal settings.

4.2.2.2 Pt: Achieving Homogeneity

By fabricating L-structures at different pulse durations (DTs) and passes, further insights on depositing dynamics can be received. For achieving homogeneous line profiles, seven Pt L-structures were fabricated de novo, each of them with identical TET but varying passes / DT. The TET was kept constant at 10 ms, the DT ranged from 10 to 10 000 µs and, consequently, the number of passes varied from 1 to 1000. To multiply to a constant TET, the DT had to be decreased when the number of passes was increased and vice versa. The measured line dimensions (height and width) with respect to the used parameters are plotted in Figure 41. The L-structure fabricated with 1 pass / DT 10 000 µs had line heights of 6.4 - 8.2 nm and line widths of 18.0 - 21.8 nm. The outer line (blue) exhibited distinctively pronounced dimensions, compared to single / inner lines (see AFM height image in Figure 42(b)). Since outer line was deposited at first (c.f. Figure 36), it considerably benefited from the high initial precursor molecule density (also called first-shot effect). The other L-shape lines (10 - 1000 passes) had their heights from 7 nm (smallest line at 10 passes) to 17.5 nm (highest line at 1000 passes) and widths from 19 nm (all lines at 10 passes) to 23.5 nm (broadest line at 1000 passes).

Despite a constant TET, both line height and line width tend to rise for higher pass counts, which has been attributed to a pass by pass time accumulation for gas replenishment, altogether increasing the available amount to precursor molecules on the deposition area. Generally speaking, while the time the electron beam is moving over one specific deposition area, the others areas are getting replenished. This effect intensifies with an increasing number of passes. The elaborated theory of the molecule coverage depending on the electron beam velocity is depicted in Figure 42(a): The actual local molecule coverage (green curve) is a convolution of the pulse duration related coverage (blue curve) and the refresh time related coverage (red curve), both depending on the DT. In an ideal case, both pulse duration and refresh time related coverage are on their peak (value 1), resulting in an ideal convolution (value 1). If the DT is increasing (theoretically based on an ideally adjusted DT), the electron beam remains for a longer time on each depositing sector causing a higher molecule depletion and subsequently a decrease in the pulse duration related coverage. On the other hand, if the number of passes is increasing (implying that the DT is decreasing), the electron beam patterning velocity increases, which creates a steadily intensifying hindrance of gas flux towards the structure center. This leads to bowl shaped deposits (see Figure 42(c)), which already had been observed in chapter 4.2.2.1 and can also be perceived on the curves in Figure 41(a) and (b) for passes > 10 / DT < 1000 µs.

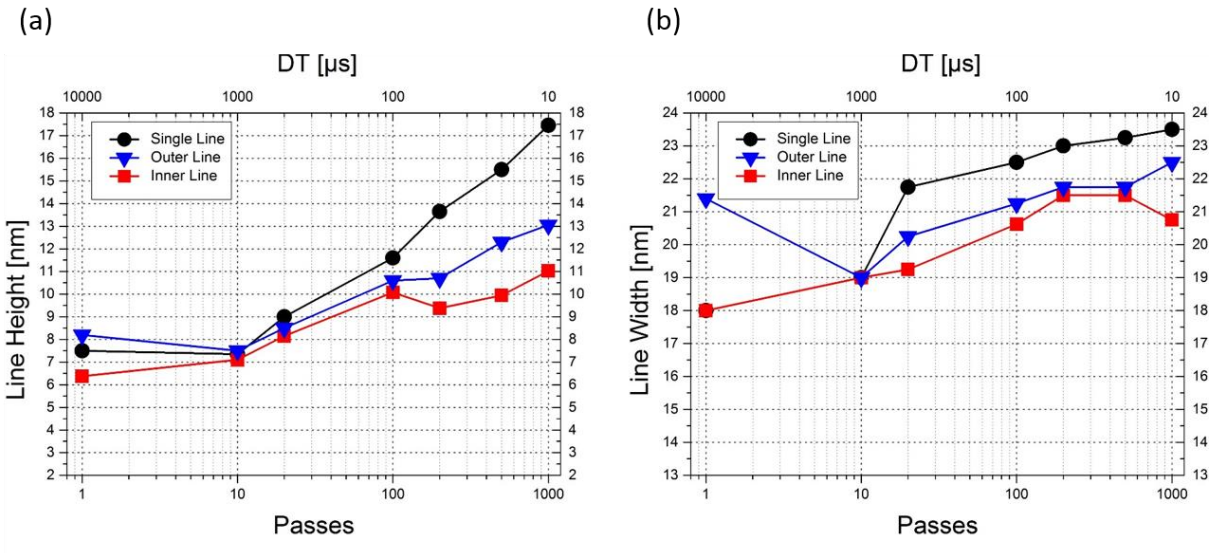

Figure 41: Dependence of line dimensions on the electron beam pulse duration (DT / passes) at constant TET for Pt L-structures. The line height was measured via AFM and the line width (base width) deduced from SEM images. Chart (a) shows significant line splitting for passes higher 100 (DT < 1000 µs), resulting in a bowl shaped deposit geometry. Chart (a) and (b) exhibit the outer line being distinctively pronounced for 1 pass (DT 10 000 µs), compared to inner and / or single lines. At 10 passes (DT 1000 µs) an accurate ratio was found: Here, all lines emerged homogeneously.

The line height strongly split up for passes higher than 1000 and the inner lines (red) nearly remain constant for values from 100 to 1000. However, for 10 passes / DT 1000 µs the structure features line heights and widths that are almost homogeneous (see Figure 42(d)). For this specific parameter setting, there was an ideally adjusted electron beam pattern velocity (being neither too slowly nor too fast). Here, an adequate ratio of proximal depletion and obstruction intensity of the inwardly replenishing molecules was found. The determination of the ideal beam velocity is nontrivial, but for the Pt precursor the most homogeneously grown lines could be found at 10 passes / DT 1000 µs when using a TET of 10 ms.

In summary, a line dependent splitting of height and width for varying passes at constant pulse durations unequivocally had been found (section 4.2.2.1 and Figure 38). In a second step, the total exposure time was kept constant and the pulse duration varied, while the number of passes had been adapted accordingly. Again, a line dependent height / width splitting was observed (this section, Figure 41). Both experimental approaches conclude that true ELR conditions had not been reached due to dwell-time induced depletion (Figure 42(b)) or replenishment issues (Figure 42(c)). A homogeneously distributed height and width of a structure (Figure 42(d) generally points on a carefully balanced regime situation, not on electron limited regime conditions. To overcome this limitation, the replenishment situation had to be improved, which can be realized by additional pause times in between individual passes for sufficiently short beam pulses. However, as the original interest was on the fabrication of high-resolution Au structures, this approach was postponed to a later point and it was decided to perform similar DT / passes experiments with the Au precursor to study the general behavior.

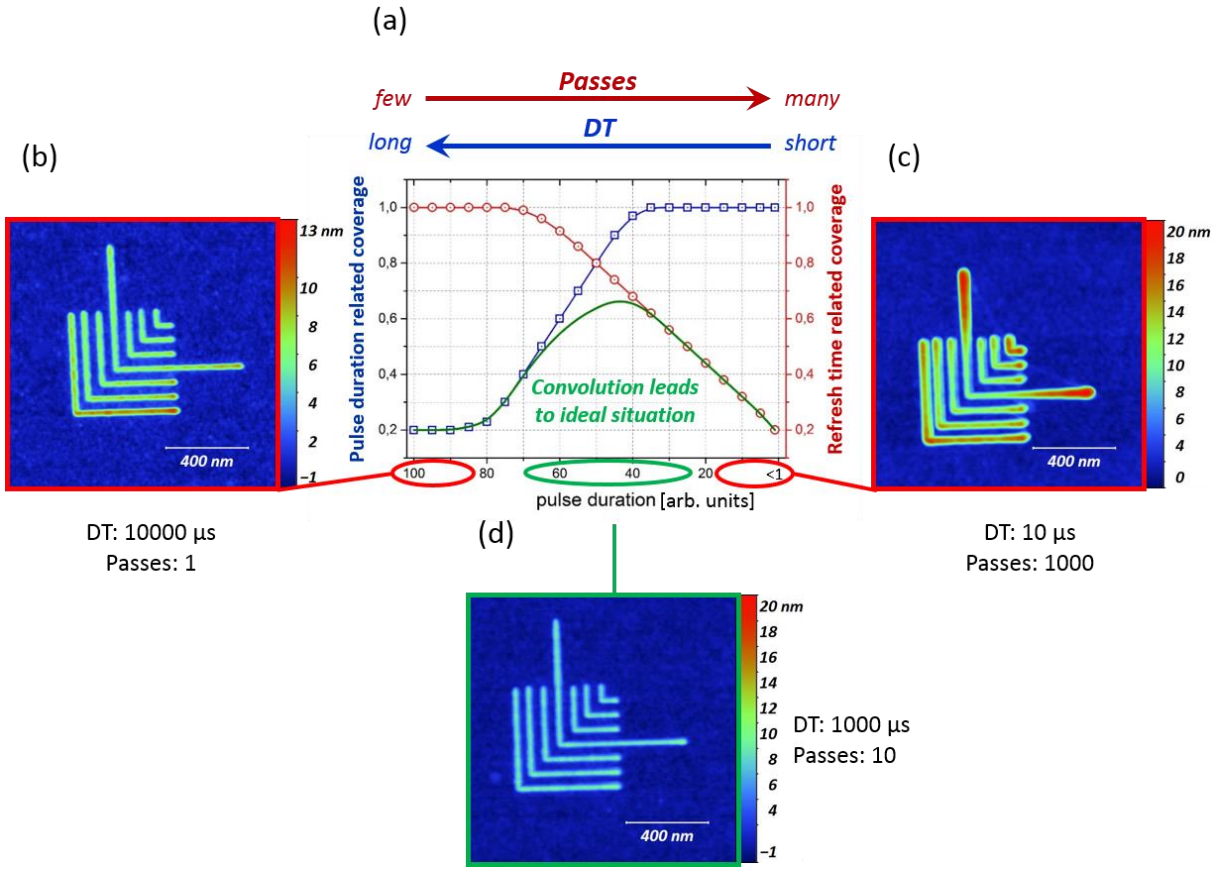

Figure 42: Theory of the precursor molecule coverage depending on the electron beam pulse duration (b). The three AFM images show several Pt L-structures deposited with similar TET but varying DT / number of passes. (a) The electron beam moves too slow (too high DT) and serious proximal depletion emerges. (c) The electron beam moves too fast (too low DT) and a bowl shaped structure emerges. (d) A correct ratio between DT and passes leads to homogeneously distributes structure lines. For more information on chart (b) see Figure 50.

4.2.3 Au Precursor

The reliable fabrication of homogeneous nanostructures when using the Pt precursor was enabled by having the required parameter range primarily localized. In the following chapter, similar approaches were done by using the Me_2-Au(acac) precursor. The Au GIS adjustment was opted equally to the arrangement applied in the manufacturing of bi-rings (chapter 4.1), shown in Figure 27, with the sole exception that the surface-to-nozzle (lower edge) distance had been decreased to 50 µm, just as it was the case for the previous Pt precursor experiments (chapter 4.2.2).

4.2.3.1 Au: General Deposit Growth Dynamics

The general deposit growth behavior at using the Au precursor was examined identically to the previous Pt L-shape experimental series, i.e. with a varying TET of 5 - 100 ms (over a variable pass count) at constant DT. The number of passes ranged from 50 to 1000 with the DT fixed at 100 µs. The

Au growth rate was found being qualitatively similar but quantitatively inferior to the Pt experiments (compare Figure 38 and Figure 43). The line height varied from 5 nm for 50 passes to 39 nm (inner lines) / 61 nm (single line) for 1000 passes (see Figure 43(a)), which makes the growing curve of Au (in dependency of the TET) to be less steep than that of Pt. A distinct height splitting continuously became manifested for passes > 100, again indicating a scarcity of precursor gas. The widths of Au (see Figure 43(b)) also appear similar to those of Pt, with a splitting of width occurring for passes > 100. An intense width enlargement was found on all lines for passes 100 - 400, whereby for passes > 400 the line width just sparsely grew. The flattening in the growing curve was also found on Pt, but in a less distinct manner. This was in fact a first strong indication that the working regime changed towards electron limited conditions. The determination of line widths for L-structures deposited with passes fewer than 100 was not possible via SEM, as the lines were not adequately discernible due to their small dimensions. However, the width at 50 passes could be ascertained for the vertical single line via AFM, giving a FWHM of 12.5 nm (see Figure 44). Again, it needs to be point out that AFM widths on that scale are slightly prone to convolution issues. This means that the here found width of 12.5 nm has to be considered as upper value, which in fact is assumed to be slightly smaller (around 10 nm). This lateral dimension accompanied by a height of 8 nm has set a new benchmark in FEBID, irrespective of the used type of precursor.

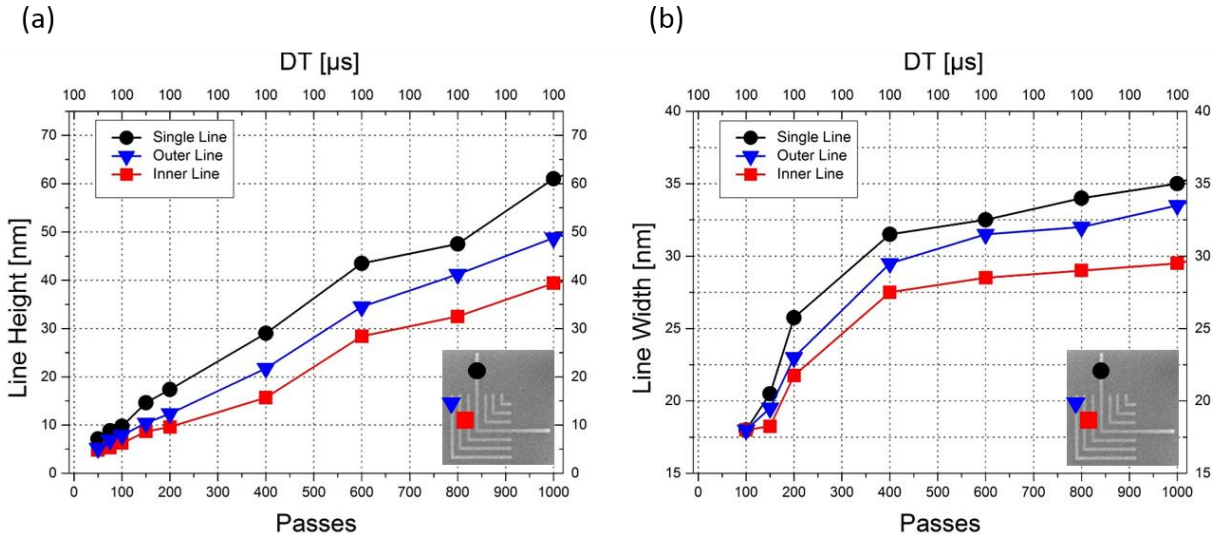

Figure 43: Dependence of line dimensions on the electron beam pulse duration (DT / passes) for Au structures, if keeping the TET constant. The line height was measured via AFM and the line width (base width) was deduced from SEM images. Chart (a) shows line splitting on all L-structures, increasing for higher passes due to the scarcity of precursor gas. (b) Lines strongly broaden for passes < 400 and flattens for passes > 400. Altogether, both charts appear similar to the charts in Figure 38.

So far, a clear improvement in the depositing accuracy had been achieved, shown in Figure 45. While even the fine-tuned bi-rings (chapter 4.1.3) had line profiles with FWHMs of 35 nm at heights of roughly 10 nm (unpurified), the Au L-structure (particularly the vertical single line at 50 passes and DT 100 µs) could be fabricated distinctively smaller. This enhancement not only could be traced back to the use of lower DTs and higher number of passes, but also to the augmenting of the PoP (from 5 to 9 nm) and the reduction of nozzle-to-surface distance (from 430 µm to 50 µm).

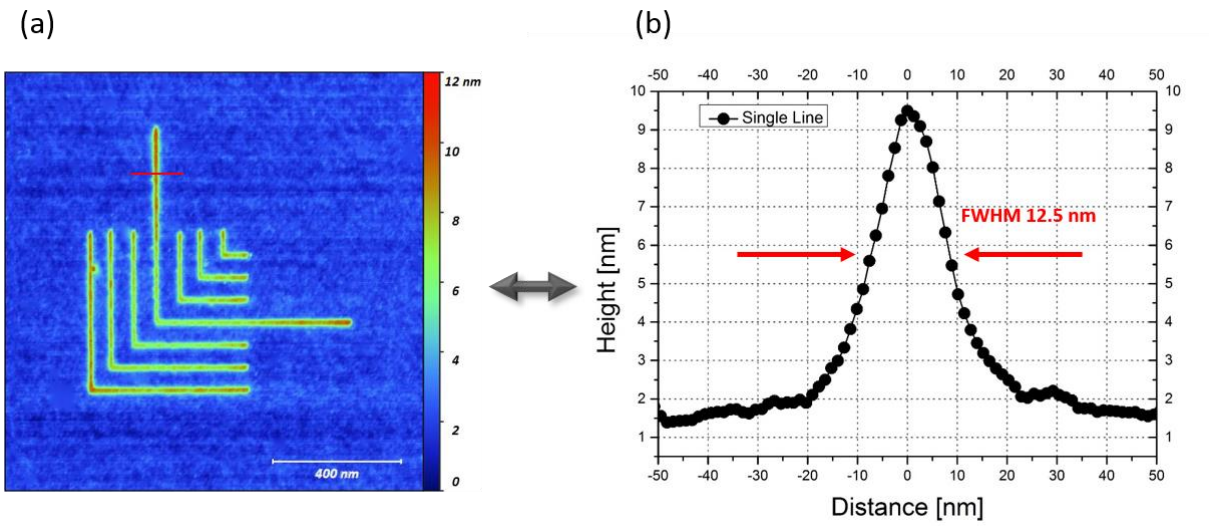

Figure 44: (a) AFM height image of an Au L-structure, deposited with 50 passes and DT 100 µs. The width determination was only achievable for the vertical single line due to tip convolution on the other deposit areas. (b) The FWHM was determined to be 12.5 nm at a height of approximately 8 nm, setting a new benchmark in FEBID. **Note logarithmic scale *of the* X-axis.**

However, even if a remarkable ratio of line height and width already had been successfully achieved (Figure 44), the line types show deviations to one another on nearly all L-shapes. Also a critical look on the 2D AFM image (Figure 44(a) still implies a bowl shaped height distribution as outer and single lines are slightly higher (see red color). Hence, as an adequate line homogeneity in the targeted height of 10 - 20 nm for widths of less than 25 nm had not been attained till that point, the implementation of a subsequent parameter optimization similar to the approach for Pt (fixed TET and varying passes / DTs) was considered necessary.

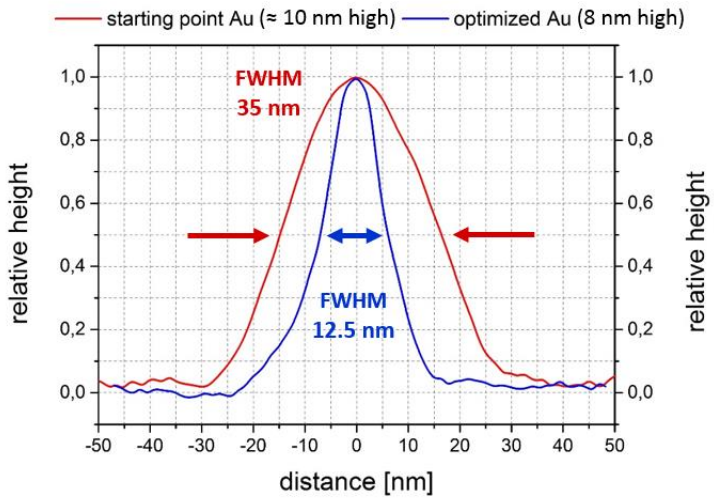

Figure 45: Comparison of the line profiles of an unpurified, fine-tuned bi-ring from chapter 4.1.34.1 (red line) and the vertical single line of the Au L-structure that was deposited with 50 passes and DT 100 µs (blue line). The parameter optimizations for the L-structures, which also included an augmented PoP (9 nm) and a lowered nozzle-to-surface distance, clearly show an improvement in the fabrication accuracy.

4.2.3.2 Au: Achieving Homogeneity

The fine-tuning at constant TET was conducted equally to the strategy used for the Pt precursor in 4.2.2.2. Seven L-structures were deposited with a TET of 10 ms and had passes varying from 1 - 10 000 with DTs that were re-adjusted, respectively, ranging from 10 - 10 000 µs. In this subsection, the aim was to attain a parameter set that enables all line types to grow equally and, as possible, a fabrication in the RRL regime. The outcome is shown in Figure 46(a) and Figure 46(b), showing the height and width evolution, respectively, in dependency on the passes with adapted DTs (to establish a constant TET). For 1 pass (highest DT) the same effect as for Pt was observable, resulting in an outer line that was emerged more dominantly (blue in Figure 46(b)). However, the dominance of the outer line for Au is less distinctive than for Pt. With heights of 3.5 nm (single and inner line) and 4 nm (outer line), and widths of 14 nm (single and inner line) and 15 nm (outer line), the Au lines arose smaller compared to the lines at 1 pass using the Pt precursor (cf. Figure 41). A progressively increasing line splitting of height was spotted for pass counts equal or higher than 20 (DT ≤ 500 µs). For 100 passes / DT 10 µs the lines reached heights of 6.2 nm (inner line), 8.4 nm (outer line) and 12.3 nm (inner line), which is roughly two-thirds of the Pt line heights at this parameter setting. This result substantiates that for deposition the Au precursor generally is being less efficient than the Pt precursor. The lower capability of the Au precursor to provide material deposition could most likely be traced back to **1)** a lower propensity for surface adsorbance (density of operational molecules), or / and **2)** a lower probability of interaction between adsorbed precursor molecules and impinging electrons (cross section), or / and **3)** a lower adherence of the yet cracked precursor molecules (volatile Au deposit). However, by analyzing the line width in dependence of the passes / DT (Figure 46(b)) effects occurred that were similar to those of the Pt experiments. This included the specific first-shot effect for one pass, noticeable by an overall dominating outer line (width of 15 nm, compared to 14 nm for single and inner line), and a significantly increasing width splitting for passes higher than 10 (DT < 1000 µs).

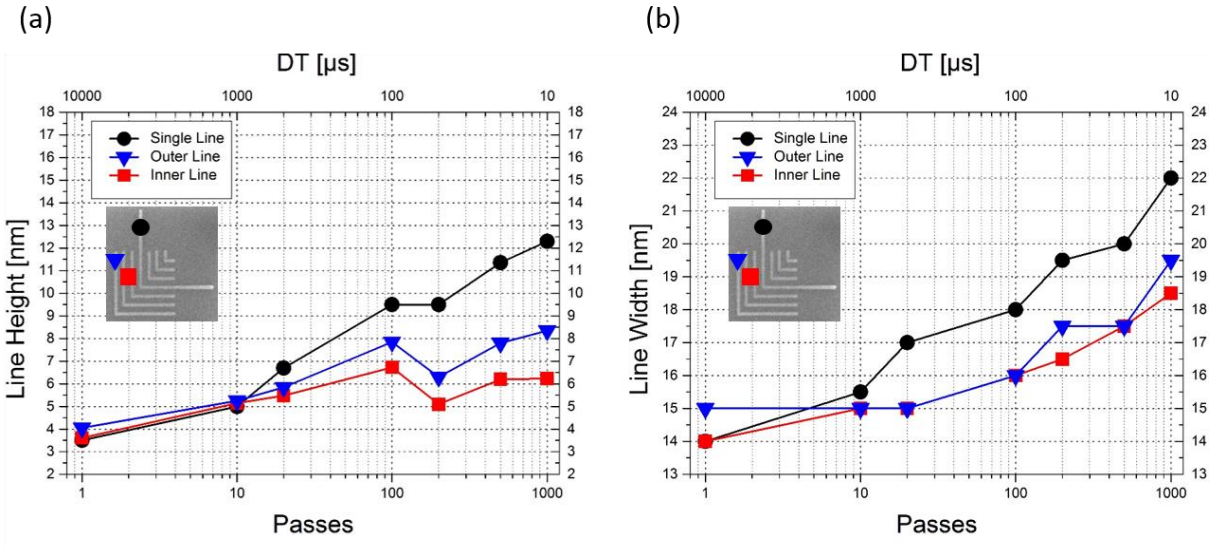

Figure 46: Dependence of line dimensions on the beam pulse duration (DT / passes) at constant TET for <u>Au</u> L-structures. The line height was measured via AFM and the line width (base width) deduced from SEM images. As for the Pt structures (Figure 41), a significant splitting in height (a) and width (b) occurred for passes > 10 (DT < 1000 µs). For 1 pass (DT 10 000 µs) both charts show the outer line developed larger than single and / or inner lines. For 10 passes / DT 1000 µs all lines show nearly similar in size, representing an ideal parameter set. Note logarithmic* scale *of the* X-axis*.

As described in chapter 4.2.2.2, this effect can again be traced back to the strongly decreasing replenishment times due to shorter pass durations by the lower DT. The Au lines generally were found thinner compared to the Pt lines, which is in accordance with the lower height reached on these experiments. Although the line widths were still slightly varying for passes < 20 (see Figure 46(b) the outer line (blue) seems to finally stagnate for very low passes. In particular, the 10 passes / DT 1000 µs doublet reveal a very narrow distribution in both heights and widths. Hence, it is worth to have a look on the entire L-structure as shown by a 3D AFM height image in Figure 47. As evident, the height distribution across the entire L-structure is very narrow with height variations in the sub-nm range. Although height / width evolution around this values still suggest non-perfect RRL conditions, these settings are close to that regime. Being more precise, these parameter setting rendered an ideal ratio of adsorbed precursor molecules (initially available and replenished) and depletion.

These contrarieties just were equilibrated, but an RRL regime could not be accomplished successfully. If an RRL regime had been achieved, all lines would have collectively exhibited heights of at least 12.3 nm (highest line in Figure 46(a)), as the quantity of impinging electrons would have been the only limiting factor. At this scale, both precursor types (Au and Pt) lack the necessary efficiency to enable an RRL working regime directly without further implements. Regardless of the existing deposition regime, if a fabrication of homogeneous structures is favorited for heights of 5 nm and widths smaller than 16 nm, the usage of 10 ms of TET (and 9 nm PoP at a lowered surface-to-nozzle distance), apportioned into 10 passes at DT 1000 µs, will be the proper parameter window on planar Si substrates. Compared to the intended bi-ring geometry (> 15 nm height), a TET of 10 ms was evaluated to be too low. To achieve future results of higher structures, it is suggested to raise the TET by simply increasing the number of passes while keeping the DT (10 µs), PoP (9 nm) and nozzle-to-surface (50 µm) constant. However, for reaching into the RRL regime, an enhancement of the amount of available precursor molecules was considered necessary, which was hereinafter implemented by adding a certain amount of time after each pass while depositing (in chapter 4.2.5).

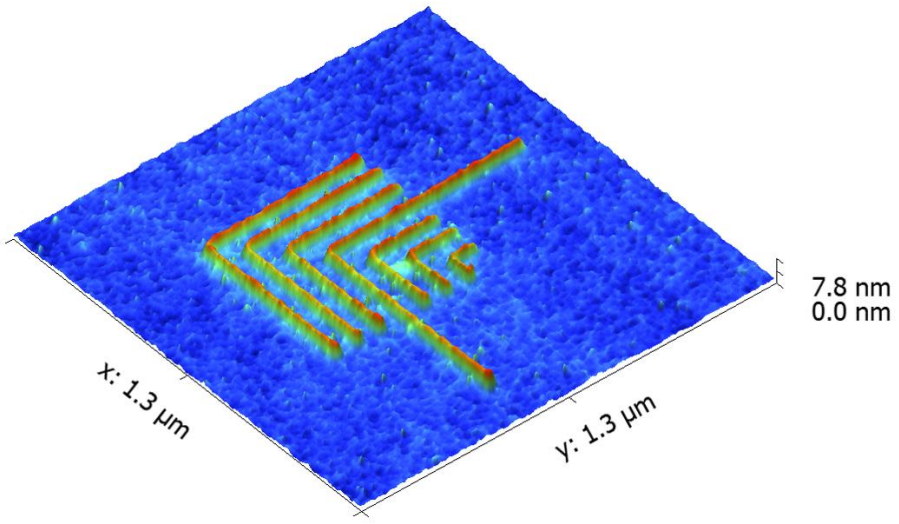

Figure 47: 3D AFM height image of an Au L-shape with homogeneously grown lines for 10 passes and DT 1000 µs. Although the lines appearing nearly ideal at this parameter setting, the deposit was not fabricated in the RRL regime.

4.2.4 50 Hz Power Line Synchronization

Before focusing on the attempt of adding replenishment time to increase the surface molecule coverage in between two consecutive patterning loops, a separate approach to reduce the line thicknesses was targeted. For this purpose, the patterning strategy was synchronized to the 50 Hz power line, which had also brought success in experiments conducted in 2011 by Van Oven et al.[65], who achieved reduced line widths by a power supply synchronization. In their experiments on resolution limits using the Pt ($MeCpPt^{IV}Me_3$) precursor, Van Oven et al. observed distinctive oscillations on their deposited structures, one with having a frequency of 50 Hz, exactly coinciding with the power supply frequency. It was suspected that the power line created slight magnetic field fluctuations inside the DBM / SEM according to the 50 Hz power supply, which could lead to small but evident inaccuracies in positioning and pulse durations (rather than raising mechanical vibrations, as an advanced damping mechanism was incorporated). The interacting caused specific disturbances in the patterning dynamics and, subsequently, lateral structure broadening. Since the interfering vibration phase was shifting with each patterning cycle, they forced the electron beam to park beside the structure after each pass whilst depositing (similar to this thesis, they deposited by using multiple passes). The electron beam was given a variable waiting time in such a way that each pass (including waiting time) had a cycle of 20 ms (power line cycle). Structures that were deposited by this strategy featured these distinctive irregularities less apparently. The synchronization in this thesis was conducted by redesigning the L-structure. The protruding section of the horizontal single line was elongated from 300 to 1100 nm, which augmented the exposure time of an L-structure within one pass exactly to 60 ms (multiple of 50 Hz), as visible in Figure 48.

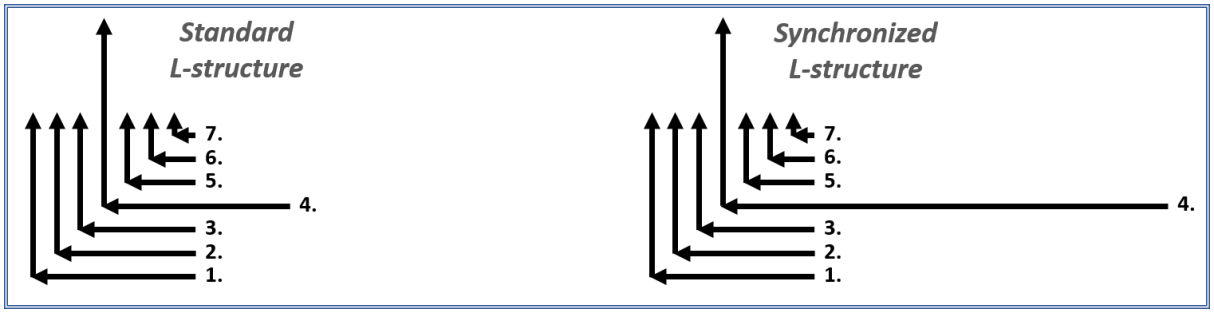

Figure 48: The patterning arrangement of standard and synchronized L-structure. The horizontally protruding center line was elongated in such a way that the overall deposition time of one patterning cycle (one pass) was inherently synchronized to the power line frequency.

This approach avoided the additional expenses of implementing a variable electron beam parking time for each pass and made the exposure time of the L-structure inherently identical to the power line period without losing the particular capabilities of the "L"-shaped geometry. To assess the difference between L-structures made in synchronization to the power line and those that were not, a redesigned and an ordinary L-structure set were deposited next to each other. A set comprised of two L-structures with equal TET, one fabricated with 1 pass / DT 10 000 µs, and the other deposited with 100 passes / DT 100 µs. The results are visible in Figure 49, showing height (**blue**) / width (**red**) of single (a), outer (b) and inner lines (c) of each of the four L-structures. As evident, no clear correlation could be found

between synchronizing the electron beam pass cycle and the line width, as nearly line types at all passes / DT yield similar widths (16.3 - 17.5 nm) for both synchronized and non-synchronized structures (except the single line at 100 passes / DT 100 µs, yielding 17 and 17.5 nm, respectively). At this point, it must be mentioned that the L-structures were appreciably more difficult to measure than those in the experiments before due to the small size and specific technical conditions. Therefore, the measurement errors were regarded being higher than usual (see 4.2.1). The accuracy was assessed to be about ± 3 nm in width (SEM) and ± 1 nm in height (AFM). Furthermore, there was also no correlation found between a synchronized beam and the resulting line heights. The heights were even reversed for synchronized and non-synchronized lines, leaving the ordinary L-structures about 1 nm higher than the redesigned ones, for all line types and both pass numbers (black data points in all charts in Figure 49). To summarize, there could no improvement in patterning resolution determined when attuning the pass period of the electron beam to the power line frequency.

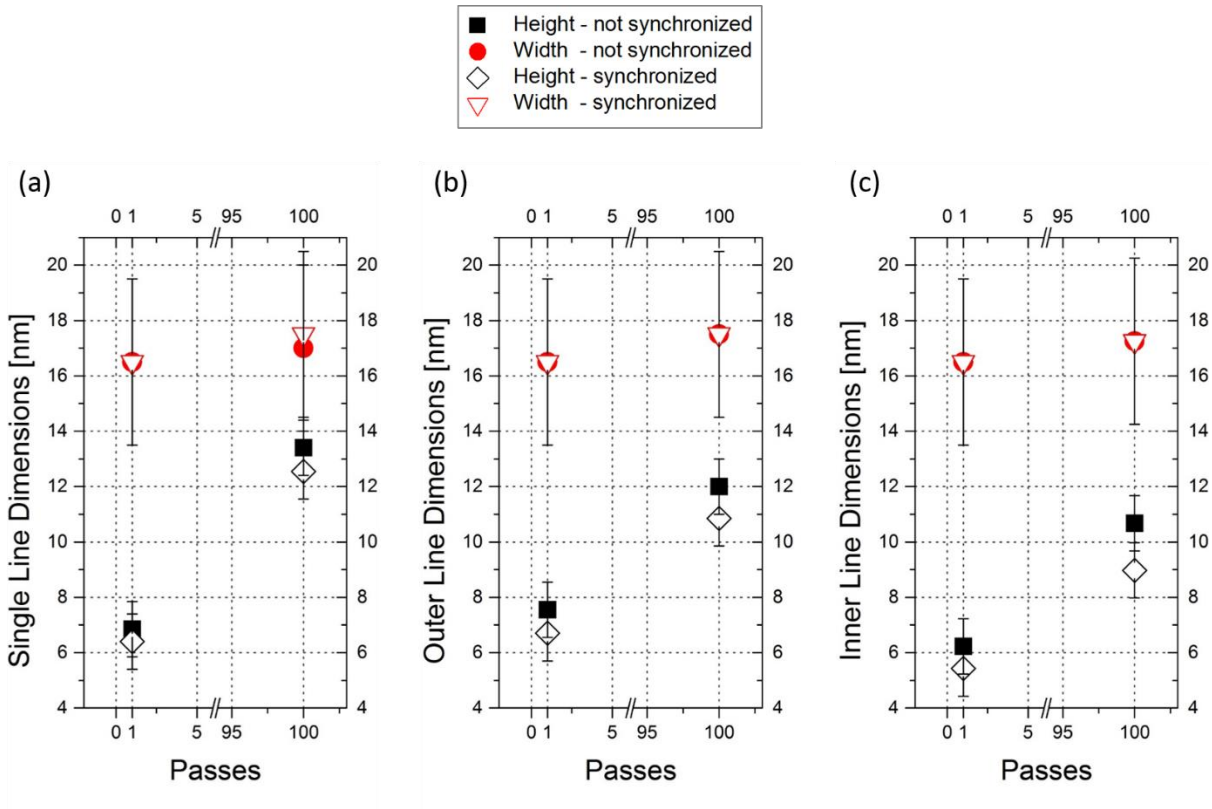

Figure 49: Line heights / widths of L-structures fabricated ordinarily (solid data points) and with pass cycle times synchronized to the 50 Hz power line (open data points). There is no correlation quantifiable between synchronizing the electron beam cycle with the electrical grid and improved depositing accuracy. All L-structures were deposited with a TET of 10 ms.

4.2.5 Increasing of Molecule Coverage

So far, in none of the approaches a full RRL regime could be established, wherefore an approach had been sought to tangibly increase the molecule coverage during deposition. Before focusing on the experiments, the dynamic coverage situations has to be comprehensibly rationalized, which is a convolution of pulse duration related coverage and refresh time related coverage, as visualized in

Figure 50: This starts by having a look at the idealized local coverage in dependency on the pulse duration shown by the blue squares in Figure 50(a) (left axis). As evident, the longer the pulse duration (from right to left) the higher the local depletion is due to increasing molecule consumption. The upper right plateau reflects RRL conditions where sufficient molecules are available. For increasing pulse durations, the coverage decays towards the lower left plateau. It is important to note that this plateau is not at zero coverage owing to the constant replenishment via direct gas flux adsorption. The replenishment time is linked to the replenishment situation, given by the red circles in Figure 50(a) (right axis). For long pulses (left hand side), the refresh time is high as it takes much longer before the beam comes back to the first patterning point. Hence, the refresh time related coverage is sufficiently high, which explains the elevated plateau at the left. As both the pulse and refresh time related coverage are linked to each other but show a different behavior, the final coverage situation is a convolution of both, visualized by the green curve in Figure 50(a). As evident, there is a maximum at the center, which reflects the best situation possible. Shifting the parameters to the left or right again leads in both cases to MLR conditions. This is what could be seen in Figure 41 (Pt) and Figure 46 (Au) by the best compromise at DTs of around 10 µs. The important part in Figure 50(a), however, is that the central peak is not necessarily at a coverage value of 1, which is the requirement for true RRL conditions. While the pulse duration related depletion behavior is invariable, the refresh time related replenishment can be influenced. In more detail, the introduction of an additional refresh time effectively shifts the red curve in Figure 50(a) to the right, as shown in Figure 50(b). By that, a region evolves which should lead to true RRL conditions as indicated by the green circle on top. Therefore, the subsequent task was to increase the additional refresh time (**RT**), until true RRL conditions establish. On this basis, complementary RT experiments were integrated by forcing the electron beam to park apart from the intended deposition area subsequently after each pass, adding a certain amount of time for the precursor molecules to replenish.

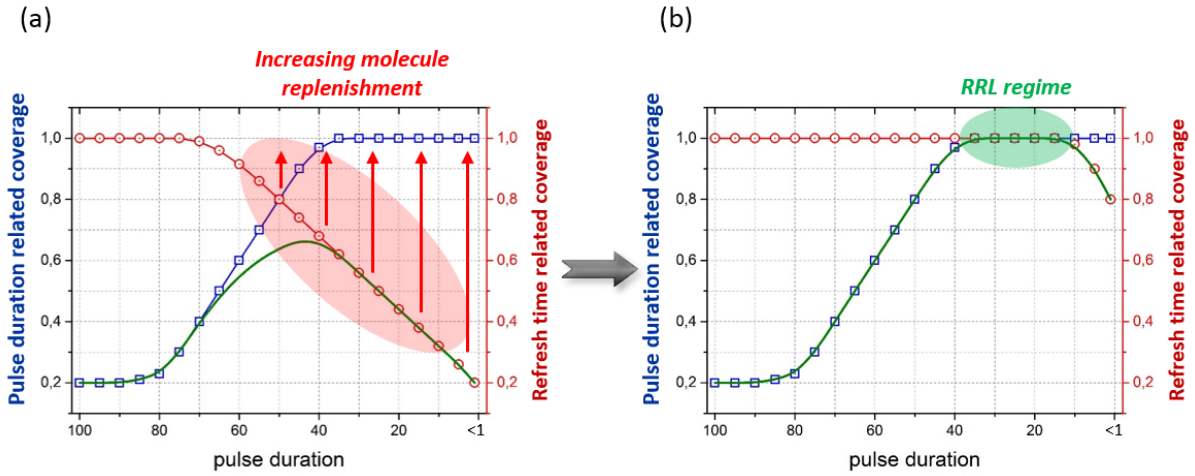

Figure 50: Total molecule coverage (green curve) is a convolution of pulse related coverage (blue curve) and refresh time related coverage (red curve). For achieving an RRL regime (green area in (b)), the molecule replenishment was increased (red arrows in (a)) by parking the electron beam apart from the intended deposition area subsequently after each pass, which adds complementary refresh time.

To determine the required RT necessary for attaining the RRL regime, two set of Au L-structures were deposited, both with a TET of 10 ms. The first set consisted of six L-shapes, fabricated with 100

passes / DT 100 µs and RTs of 0, 10, 100, 200, 500 and 1000 ms per pass, respectively (subchapter 4.2.5.1). The second one composed of four L-structures fabricated with 1000 passes / DT 10 µs and RTs of 0, 50, 100, 500 ms per pass, respectively (subchapter 4.2.5.2). For realizing this, an additional, mirror-inverted L-structure was positioned 4 µm beside the standard L-structure (see Figure 51). The mirrored L-structure was considered to be the parking area for the electron beam. The TET of the inverted L-structure was equivalent to the refresh time and had to be adjusted for each RT value separately.

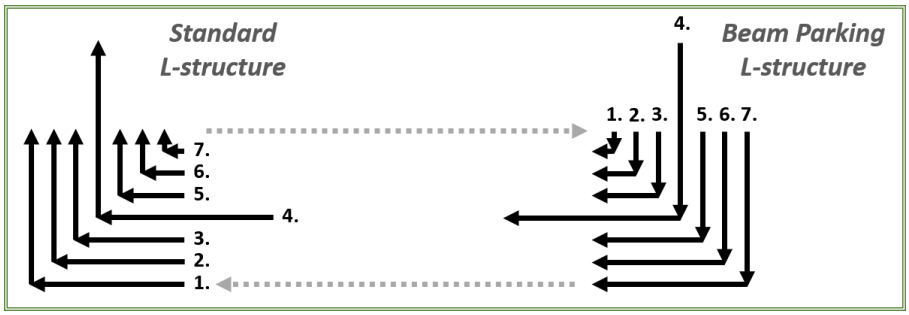

Figure 51: Scheme of the implementation of refresh times. A mirror-inverted L-structure was positioned beside, which functioned as an electron beam parking area. The TET of the mirrored L-structure was equivalent to the RT.

4.2.5.1 Refresh Time Adding for High Dwell Times

In a first attempt, L-structures were fabricated with 100 passes / DT 100 µs, as it was assumed that a pulse duration of equal or less than 100 µs of DT (at 9 nm PoP) will, if a certain amount of RT was added, fully suffice to establish of an RRL regime. Figure 52 depicts the line heights / widths for L-structures deposited with various RTs applied. Both curves (Figure 52 (a) and (b)) show a significant gain of both line height and line width when implementing RTs while depositing. The L-structure fabricated without RT revealed the lowest deposit volume with line heights from 6.2 nm (inner line) to 8.8 nm (single line) and line widths from 18 nm (inner line) to 21 nm (single line). These geometries were roughly similar to those found on the L-structure made with 100 passes / DT 100 µs in 4.2.3.2 (cf. Figure 46), and were also featuring line splitting. The line volume considerably increased for raised RTs and saturated for RT higher than 500 ms per pass, giving a maximum height of 11.3 nm (inner line) to 12.9 nm (outer line) and a maximum width of 35 nm (all line types). The line splitting was even prevalent for RT of 1000 ms per pass, which indicated that an RRL regime could not be fully established. This, in combination with saturating line volumes for high RTs, refers to a DT that was set too high, which inevitably leads to a decrease in the pulse duration related molecule coverage (cf. blue curve in Figure 50). However, the fabrication of precisely made nanostructures highly benefits from implementing RTs due to the increased height / width ratio, whose proper (and adjustable) value is considered being a key feature in the realization of adequately working deposits in the two-, or even one-digit nanometer scale.

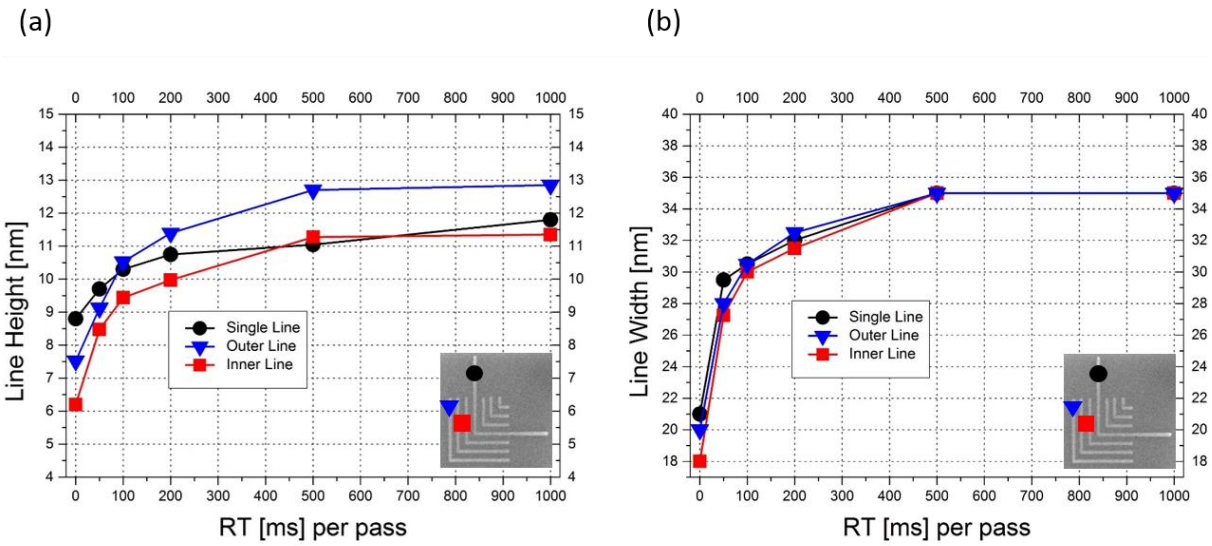

Figure 52: Dependence of line dimensions on the implemented refresh time for Au L-structures, all deposited with 100 passes / DT 100 µs. Both line heights (a) and line widths (b) show a strong dependency on the RT. While the undesirable line splitting is prevalent even for an applied RT of 1000 ms per pass, line height / width start to saturate for RTs higher than 500 ms per pass. The combination of volume saturation and line splitting indicates that the pulse duration (DT) was too high, and a lower DT is necessary to attain the RRL regime.

4.2.5.2 Refresh Time Adding for Low Dwell Times

Regardless of the added amount of RT, reaching into an RRL working regime could not be sufficiently attained by using a DT of 100 µs (100 passes) or higher, wherefore a last set of L-structures was deposited with a DT of 10 µs / 1000 passes. The increase of the beam's pattern velocity was expected to ensure the pulse duration related coverage to remain sufficiently high while depositing (cf. Figure 53), which should lead, in combination with an adequately set RT, finally to a full establishing of the RRL regime.

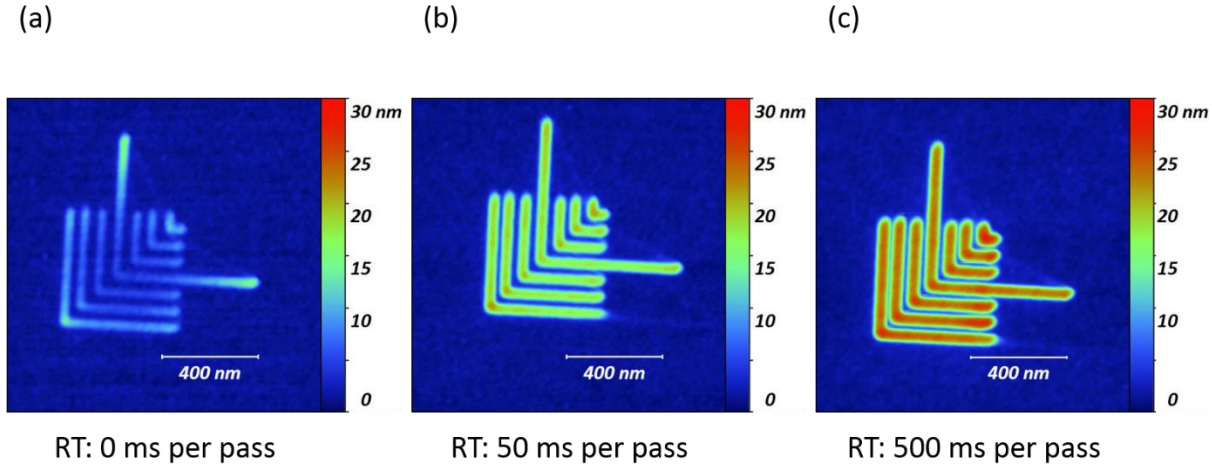

Figure 53: AFM height images of L-structures deposited with 1000 passes / DT 10 µs and RTs of 0 (a), 50 (b), and 500 (c) ms per pass, respectively. The implementation of RTs significantly intensifies the volume growth rate at identical electron doses (TET). The L-structure fabricated with an RT of 50 ms per pass (b) was deposited nearly and the L-structure fabricated with 500 ms per pass (c) was deposited fully in the RRL regime.

Four L-shapes were deposited with RTs that were partially similar to those applied previously (being 0, 50, 100 and 500 ms per pass, respectively), but they had their total refresh time (**TRT**), at equal RTs, higher by a factor 10 compared to the TRT for the L-structures deposited with DT 100 µs, as the number of passes was ten times higher (the TRT adds up with each pass). The large volume growth for increasingly added RTs are well noticeable in Figure 53. As displayed in Figure 54, the L-structure fabricated with a DT of 10 µs featured lines of 4 nm (inner line) to 11.8 nm (single line) and widths of 19 (inner line) to 23.5 nm (single line), which also roughly coincided with the L-structure that was fabricated with an identical parameter setting in 4.2.3.2. The line dimensions strongly increased when adding / increasing RTs and started to saturate for RTs of 100 ms per pass or higher. For RTs of 500 ms per pass (equivalent to a TRT of 500 seconds) all line types show identical heights / widths, which is a clear indication that an RRL regime had been achieved successfully.

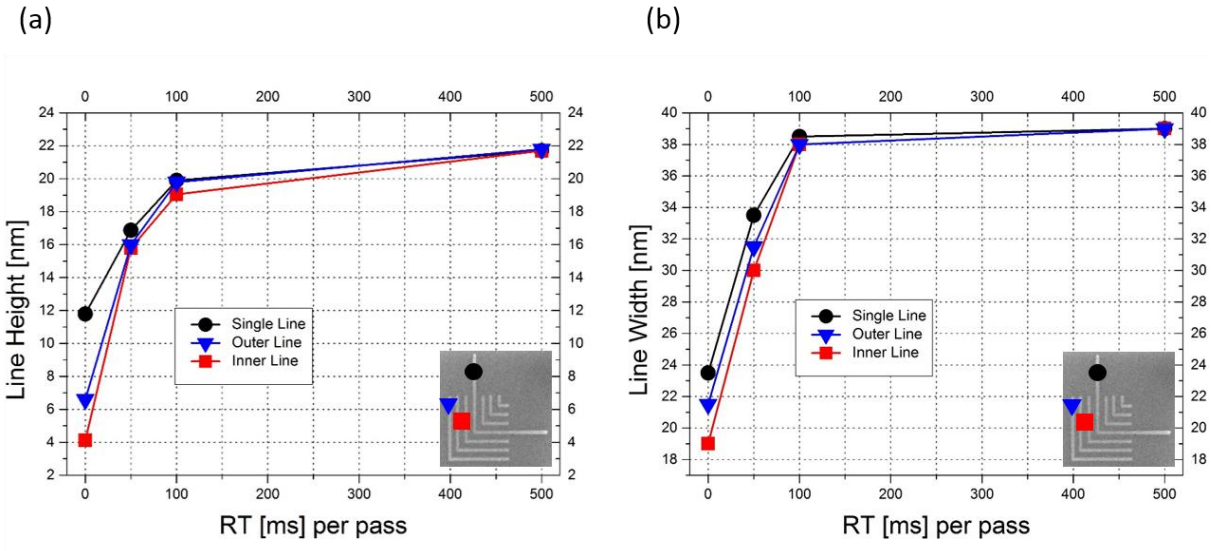

Figure 54: Dependence of the line dimensions on the added refresh time for Au L-structures, fabricated with 1000 passes / DT 10 µs. Line height (a) and line width (b) strongly grow for increasing RTs and start to saturate for RTs higher than 100 ms per pass. The combination of volume saturation and line type equalization substantiates the evidence of having an RRL regime successfully attained.

A widening of structure line profiles, in this case by nearly a factor 2 for both high and low DTs (c.f. Figure 52(b) and Figure 54(b)), is generally undesired but naturally accompanies deposit elevations. It has not been determined whether the broadening resulted from a stage drift (see chapter 2.2.6) due to the high overall depositing time when implementing additional RTs or had natural causes. Without beam parking applied, the total deposition time for an L-structure fabricated at TET 10 ms was roughly 5 seconds, whereas the implementation of an RT of 500 ms per pass caused the fabrication duration to rise to 55 seconds (DT 100 µs / 100 passes) or 505 seconds (DT 10 µs / 1000 passes). At such high fabrication times there might had been a stage drift involved, causing the structure to evolve wider than initially expected (which should be verified in further studies). However, there is a significant improvement in the height / width ratio when applying RTs, and, for the first time, real structure homogeneities successfully had been attained based on a continuously prevailing RRL regime while depositing.

5 Summery and Outlook

This thesis focused on the precise fabrication of structures on the two-digit nanoscale via focused electron induced deposition (**FEBID**) by using the organometallic precursors Me_2-Au(acac) and $MeCpPt^{IV}Me_3$. It basically was compounded by two main topics, i.e. **1)** the manufacturing and optimization of Au bi-ring arrays for obtaining plasmonic and well capable metamaterials (**MTM**), and **2)** the successful downscaling of the lateral resolution by studying the fundamental relations between process parameters and its implications on final dimensions. In more detail, it could be shown how the working regime can be systematically shifted towards ideal conditions by a careful choice of patterning strategies and a proper adjustment of patterning parameters.

Starting with the fabrication of the bi-ring array by applying a classical interlacing approach opened up a main issue, being the considerable depletion of precursor molecules during deposition. By omitting further sequencing refinements, spatial height and thickness distributions of individual bi-rings emerged. Adapted scan routines were implemented and successfully resulted in an array with structures being homogeneously developed, but individual bi-rings still revealed spatially varying on-ring volume growth rates. An empirical on-ring fine-tuning via dwell-time (**DT**) adaption removed the first-shot effect and lead to uniformly emerged individual bi-rings. Despite array and ring optimization worked effectively, a systematic height variation inside the cavity by means of a cross shaped distribution was found, which indicated a gas density imbalance within. The inhomogeneity of gas distribution could not be compensated by any alteration of sequencing or parameter setting.

In the second step, such optimized arrays were subsequently purified via a reliable H_2O approach developed by Geier et al[51]. Although successful from a chemical point of view, the ITO layer revealed massive buckling after purification, which providentially had little influence on the performance of the MTM. The purified and, for the purpose of comparison, three non-purified arrays were subjected to plasmonic measurements at the workgroup around Prof. Roskos at the Goethe University Frankfurt. Purified and non-purified arrays exhibited resonances in the predicted wavelength rage, with the purified doing more distinctively. By contrast with the initial simulation, the fabricated MTM had their optical response broader and less distinctly defined, which was attributed to the inhomogeneous array height, too broad ring line widths and a non-rectangular cross sectional profile due to the inaccessibility of the reaction rate limited (**RRL**) working regime. At this point, fabrication for direct plasmonic application stopped and a closer look on the growth fundamentals were taken, as hereinafter described. Nevertheless, this section successfully demonstrated that FEBID can be used for the on-demand, additive, direct-write fabrication of electromagnetic metamaterials.

To step away from trial-and-error approach, a more fundamental research method was chosen to unravel and finally improve the growth dynamics in ultra-high resolution FEBID. The second main topic addressed highly precise depositing and exploration of the ultimate resolution limits of FEBID for the given precursor types by using structures of simpler geometry (L-structures). In a first experiment set, the depositing behavior of the Pt precursor was determined by varying the total exposure time (**TET**) and analyzing the obtained structural volume. When the TET selection was found, in which the L-structures revealed almost the height / width the bi-rings were intended to have, a parameter fine fine-tuning was done, realized by changing number of passes and dwell-time (**DT**) while keeping the TET constant. It was able to determine the parameter set that provided the most homogeneously distributed lines, being an appropriate compromise between an electron beam patterning motion that

was adjusted too low (high DT), and a beam that was moving too fast (low DT). Identical experiments were done by using the Au precursor, which generally yielded similar results. Although it was not possible to reach into an RRL working regime, extremely small structures could be fabricated, revealing lines with FDWHs of less than 13 nm at heights of roughly 8 nm, which had set a new benchmark in the respective FEBID community. The optimization approach not only led to a parameter set that enables the manufacturing of entirely homogeneous structures for the given precursors at this scale, but also provides a universal blueprint to find suitable parameters for other deposit geometries, applied precursors, or predefined configurations. A complementary experiment was done to verify if there existed a noticeably influence on the fabricating performance when having the electron beam patterning cycle synchronized to the 50 Hz power supply frequency, with no significant connection found between a synchronization the electron beam pass cycle and an improved patterning resolution.

Since a full RRL regime could not be straightforwardly acquired by then, further experiments were executed to continually increase the molecule coverage while depositing. For that purpose, an additional electron beam parking time for molecule replenishment was specifically implemented, which resulted in considerably enlarged deposit volumes. For a certain quantity of molecule replenishment time the structural volume saturated and remained homogeneously distributed, which proved that a completely dominating RRL regime had been utterly achieved.

Overall, this master thesis featured the feasibility of functional plasmonic devices and contributed to essential acquirements to resolution limits in the area of FEBID. Figure 55 summarizes the latter aspect by directly comparing the starting situation (a) with the final achievement of homogeneous line arrays (b) revealing FWHMs in the sub-13 nm regime at heights around 9 nm (c), which is currently the worldwide benchmark in this research field. The combination of both the accessibility to the RRL working regime and the elaborated scheme to ultra-fidelity nanofabrication paves the way for prolific future research on fabricating highly efficient electromagnetic MTMs.

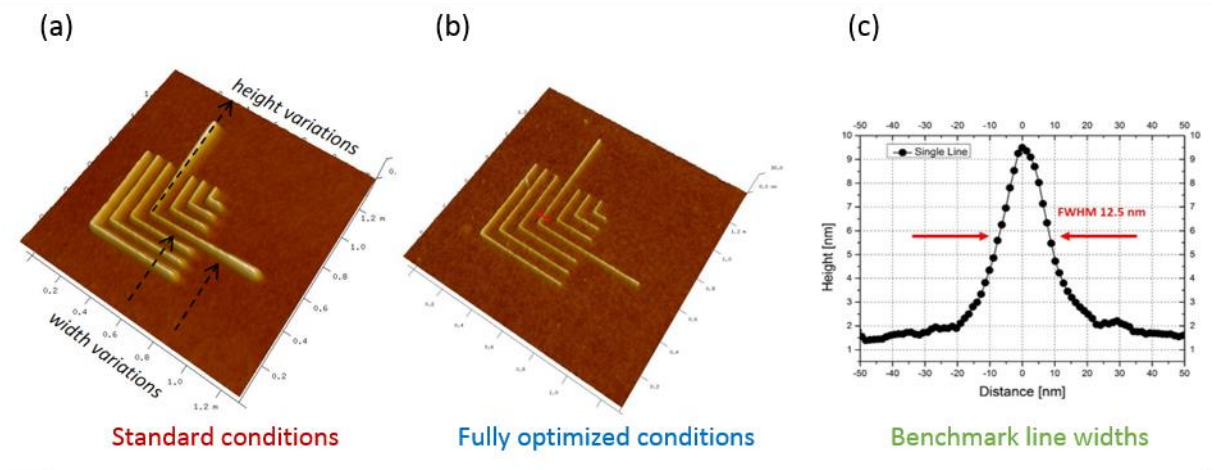

Figure 55: (a) Deposit before approaching parameter optimization. The lines were found to be too broad and inhomogeneously distributed. (b) Final deposit attained by implementing various parameter optimizations. (c) Finally achieved line width that represents a benchmark the respective research field.

References

1. Sirtori, C. Applied physics: Bridge for the terahertz gap. *Nature* **417,** 132–133 (2002).

2. Yao, Y. *et al.* Broad electrical tuning of graphene-loaded plasmonic antennas. *Nano Lett.* **13,** 1257–1264 (2013).

3. Otsuji, T. & Shur, M. Terahertz Plasmonics: Good Results and Great Expectations. *IEEE Microw. Mag.* **15,** 43–50 (2014).

4. Shalaev, V. M. Optical negative-index metamaterials. *Nat. Photonics* **1,** 41–48 (2007).

5. Chen, P. Y., Monticone, F., Argyropoulos, C. & Alù, A. Plasmonic optical nanoantennas. *Handb. Surf. Sci.* **4,** 109–136 (2014).

6. Boltasseva, A. & Atwater, H. A. Low-Loss Plasmonic Metamaterials. *Science (80-.).* **331,** 290–291 (2011).

7. Haselmann, U. Direct-Write Fabrication of Pure Metal Structures for Nano-Probing and Plasmonic Applications. (Graz University of Technology, 2016).

8. Botman, a, Mulders, J. J. L., Weemaes, R. & Mentink, S. Purification of platinum and gold structures after electron-beam-induced deposition. *Nanotechnology* **17,** 3779–3785 (2006).

9. Geier, B. Rapid and Highly Compact Purification at Room Temperature for Focused Electron Beam Induced Pt-C Deposits. (Graz University of Technology, 2014).

10. Dual Beam.

11. Johannes E. Fröch. Focussed Ion Beam assisted Deposition of Metals: Process-Parameters and Functionality Relationships. (Graz University of Technology, 2016).

12. *Courtesy of DI Robert Winkler, Institute for Electron Microscopy and Nanoanalysis, Graz University of Technology, Austria 2014*.

13. Goldstein, J. *et al.* Scanning Electron Microscopy and X-Ray Microanalysis: A Text for Biologists, Materials Scientists, and Geologists. *Scanning Electron Microscopy and X-Ray Microanalysis - A Text for Biologists, | Springer* 840 (2012). doi:10.1 0071/978-1-4613-0491-3

14. Leng, Y. *Materials Characterisation: Introduction to Microscopic and Spectroscopic Methods*. *Materials Characterization* (2008). doi:10.1002/9780470823002.ch2

15. Satoh, H., Kawata, S., Nakane, H. & Adachi, H. Studies on the ZrO/W(100) surface by means of low-energy electron diffraction and X-ray photoelectron spectroscopy. *Surf. Sci.* **400,** 375–382 (1998).

16. *FEI Company, Achtseweg Noord 5, Bldg, 5651 GG Eindhoven, The Netherlands.*

17. Drouin, D., Couture, A. R., Joly, D., Tastet, X. & Aimez, V. CASINO V2.42 - A Fast and Easy-to-use Modeling Tool for Scanning Electron Microscopy and Microanalysis Users. *Scanning* (2007).

18. *Couture AR, Drouin D, Gauvin R. CASINO V2.5.1. Monte Carlo simulation of electron trajectories in solids. 2017. Available at: http://www.gel.usherbrooke.ca/casino/download2.html.*

19. Reimer, L. *Scanning Electron Microscopy: Physics of Image Formation and Microanalysis*. (Springer Berlin Heidelberg, 1998). doi:10.1007/978-3-540-38967-5

20. *Emmanuel de Chambost (2007), Détecteur Everhart-Thornley, Wikimedia commons*.

21. Utke, I. *Nanofabrication using focused ion and electron beams: principles and applications*. (Oxford Univ. Press, 2012).

22. van Dorp, W. F. & Hagen, C. W. A critical literature review of focused electron beam induced deposition. *J. Appl. Phys.* **104,** 1–42 (2008).

23. Utke, I., Hoffmann, P. & Melngailis, J. Gas-assisted focused electron beam and ion beam processing and fabrication. *J. Vac. Sci. Technol. B Microelectron. Nanom. Struct.* **26,** 1197 (2008).

24. *Courtesy of Ass.Prof. Dr. Harald Plank, Institute for Electron Microscopy and Nanoanalysis, Graz University of Technology, Austria, 2017.*

25. Winkler, R. *et al.* The Nanoscale Implications of a Molecular Gas Beam during Electron Beam Induced Deposition. *ACS Appl. Mater. Interfaces* (2014). doi:10.1021/am405591d

26. Botman, a, Mulders, J. J. L. & Hagen, C. W. Creating pure nanostructures from electron-beam-induced deposition using purification techniques: a technology perspective. *Nanotechnology* **20,** 372001 (2009).

27. Huth, M. *et al.* Focused electron beam induced deposition: A perspective. *Beilstein J. Nanotechnol.* **3,** 597–619 (2012).

28. Liang, T., Frendberg, E., Lieberman, B. & Stivers, A. Advanced photolithographic mask repair using electron beams. *J. Vac. Sci. Technol. B Microelectron. Nanom. Struct.* **23,** 3101 (2005).

29. Lassiter, M. G., Liang, T. & Rack, P. D. Inhibiting spontaneous etching of nanoscale electron beam induced etching features: Solutions for nanoscale repair of extreme ultraviolet lithography masks. *J. Vac. Sci. Technol. B Microelectron. Nanom. Struct.* **26,** 963 (2008).

30. Utke, I. *et al.* Polarisation stabilisation of vertical cavity surface emitting lasers by minimally invasive focused electron beam triggered chemistry. *Nanoscale* **3,** 2718–2722 (2011).

31. Perentes, A. *et al.* Focused electron beam induced deposition of a periodic transparent nano-optic pattern. *Microelectron. Eng.* **73–74,** (2004).

32. Porrati, F., Sachser, R., Schwalb, C. H., Frangakis, a. S. & Huth, M. Tuning the electrical conductivity of Pt-containing granular metals by postgrowth electron irradiation. *J. Appl. Phys.* **109,** 63715 (2011).

33. Fernández-Pacheco, A. *et al.* Domain wall conduit behavior in cobalt nanowires grown by focused electron beam induced deposition. *Appl. Phys. Lett.* **94,** (2009).

34. Serrano-Ramón, L. *et al.* Ultrasmall functional ferromagnetic nanostructures grown by focused electron-beam-induced deposition. *ACS Nano* **5,** 7781–7787 (2011).

35. Gavagnin, M., Wanzenboeck, H. D., Belić, D. & Bertagnolli, E. Synthesis of individually tuned nanomagnets for Nanomagnet Logic by direct write focused electron beam induced deposition. *ACS Nano* **7,** 777–784 (2013).

36. Gabureac, M. S., Bernau, L., Boero, G. & Utke, I. Single superparamagnetic bead detection and direct tracing of bead position using novel nanocomposite nano-hall sensors. *IEEE Trans. Nanotechnol.* **12,** 668–673 (2013).

37. Engmann, S. *et al.* Absolute cross sections for dissociative electron attachment and dissociative ionization of cobalt tricarbonyl nitrosyl in the energy range from 0 eV to 140 eV. *J. Chem. Phys.* **138,** 44305 (2013).

38. LookChem.

39. Plank, H., Gspan, C., Dienstleder, M., Kothleitner, G. & Hofer, F. The influence of beam defocus on volume growth rates for electron beam induced platinum deposition. *Nanotechnology* **19,** 485302 (2008).

40. Plank, H., Haber, T., Gspan, C., Kothleitner, G. & Hofer, F. Chemical tuning of PtC nanostructures fabricated via focused electron beam induced deposition. *Nanotechnology* **24,** 175305 (2013).

41. Schmied, R., Fowlkes, J. D., Winkler, R., Rack, P. D. & Plank, H. Fundamental edge broadening effects during focused electron beam induced nanosynthesis. *Beilstein J. Nanotechnol.* **6,** 462–471 (2015).

42. Smith, D. a, Fowlkes, J. D. & Rack, P. D. Understanding the kinetics and nanoscale morphology of electron-beam-induced deposition via a three-dimensional Monte Carlo simulation: the effects of the precursor molecule and the deposited material. *Small* **4,** 1382–9 (2008).

43. Fowlkes, J. D. & Rack, P. D. Fundamental electron-precursor-solid interactions derived from time-dependent electron-beam-induced deposition simulations and experiments. *ACS Nano* **4,** 1619–1629 (2010).

44. Plank, H., Smith, D. a., Haber, T., Rack, P. D. & Hofer, F. Fundamental proximity effects in focused electron beam induced deposition. *ACS Nano* **6,** 286–294 (2012).

45. Winkler, R., Geier, B. & Plank, H. Spatial chemistry evolution during focused electron beam-induced deposition: origins and workarounds. *Appl. Phys. A Mater. Sci. Process.* **117,** (2014).

46. Szkudlarek, A., Gabureac, M. & Utke, I. Determination of the Surface Diffusion Coefficient and the Residence Time of Adsorbates via Local Focused Electron Beam Induced Chemical Vapour Deposition. *J. Nanosci. Nanotechnol.* **11,** 8074–8078 (2011).

47. Szkudlarek, A., Szmyt, W., Kapusta, C. & Utke, I. Lateral resolution in focused electron beam-induced deposition: scaling laws for pulsed and static exposure. *Appl. Phys. A Mater. Sci. Process.* **117,** 1715–1726 (2014).

48. Winkler, R. Implications of Precursor Dynamics on Nanostructures during Focused Electron Beam Induced Deposition. (Graz, University of Technology, 2013).

49. Arnold, G. *et al.* Fundamental resolution limits during electron-induced direct-write synthesis. *ACS Appl. Mater. Interfaces* **6,** 7380–7387 (2014).

50. Höflich, K., Yang, R. Bin, Berger, A., Leuchs, G. & Christiansen, S. The direct writing of plasmonic gold nanostructures by electron-beam-induced deposition. *Adv. Mater.* **23,** 2657–2661 (2011).

51. Geier, B. *et al.* Rapid and Highly Compact Purification for Focused Electron Beam Induced Deposits: A Low Temperature Approach Using Electron Stimulated H2O Reactions. *J. Phys. Chem. C* **118,** 14009–14016 (2014).

52. Donald, A. M. The use of environmental scanning electron microscopy for imaging wet and insulating materials. *Nat. Mater.* **2,** 511–516 (2003).

53. Johnson, R. *Environmental Scanning Electron Microscopy: An Introduction to ESEM*. (1996).

54. Bhushan, B. in *Handbook of Nanotechnology* 278 (2010). doi:10.1007/3-540-29838-X

55. *Plank, H. Rasterkraftmikroskopie - Atomic Force Microscopy (AFM). (Lecture Material, 2015).*

56. Pelton, M. & Bryant, G. W. *Introduction to metal-nanoparticle plasmonics*. (Wiley, 2013).

57. Monticone, F. & Alù, A. The quest for optical magnetism: from split-ring resonators to plasmonic nanoparticles and nanoclusters. *J. Mater. Chem. C* **2,** 9059–9072 (2014).

58. Utke, I., Friedli, V., Purrucker, M. & Michler, J. Resolution in focused electron- and ion-beam induced processing. *J. Vac. Sci. Technol. B Microelectron. Nanom. Struct.* **25,** 2219 (2007).

59. Friedli, V. & Utke, I. Optimized molecule supply from nozzle-based gas injection systems for focused electron- and ion-beam induced deposition and etching: simulation and experiment. *J. Phys. D. Appl. Phys.* **42,** 125305 (2009).

60. Toth, M., Lobo, C., Friedli, V., Szkudlarek, A. & Utke, I. Continuum models of focused electron beam induced processing. *Beilstein J. Nanotechnol.* **6,** 1518–1540 (2015).

61. Winkler, R. *et al.* Direct-Write 3D-Nanoprinting of Plasmonic Structures. *ACS Appl. Mater. Interfaces* acsami.6b13062 (2016). doi:10.1021/acsami.6b13062

62. Winkler, R. *et al.* Toward Ultraflat Surface Morphologies During Focused Electron Beam Induced Nanosynthesis: Disruption Origins and Compensation. *ACS Appl. Mater. Interfaces* **7,** 3289–3297 (2015).

63. Schmied, R. *et al.* A combined approach to predict spatial temperature evolution and its consequences during FIB processing of soft matter. *Phys. Chem. Chem. Phys.* **16,** (2014).

64. Orthacker, A. *et al.* Chemical degradation and morphological instabilities during focused ion beam prototyping of polymers. *Phys. Chem. Chem. Phys.* **16,** (2014).

65. van Oven, J. C., Berwald, F., Berggren, K. K., Kruit, P. & Hagen, C. W. Electron-beam-induced deposition of 3-nm-half-pitch patterns on bulk Si. *J. Vac. Sci. Technol. B Microelectron. Nanom. Struct.* **29,** 06F305 (2011).